ABSTRACT

Title of dissertation: RADIO ANALYTICS
FOR INDOOR MONITORING
AND HUMAN RECOGNITION

Qinyi Xu, Doctor of Philosophy, 2018

Dissertation directed by: Professor K. J. Ray Liu
Department of Electrical and Computer Engineering

In the era of Internet of Things (IoT), researchers have been developing new technologies and intelligent systems to answer the question of who, what, when, where, and how of things happening in the environment. Among the various techniques that measure what is happening in the surroundings, wireless sensing stands out because of its ubiquity and prevalence. On one hand, different indoor activities bring distinctive perturbations to wireless radio propagation. On the other hand, thanks to the nature of multipath, indoor environmental information is recorded and embedded in the wireless channel state information (CSI). Hence, by deploying wireless transceivers to sense the radio propagation environment and analyzing the CSI, one can extend human senses and enrich her/his insight into surrounding environments and activities.

By leveraging the natural multipath propagation of electromagnetic (EM) waves, radio analytics is proposed as a promising paradigm that deciphers radio propagation characteristics and reveals rich environmental information surround-

ing us. As one approach of radio analytics, time-reversal (TR) technique exploits the information of large degrees-of-freedom delivered by CSI and provides a high-resolution spatial-temporal resonance, by treating each multipath component in a wireless channel as a distributed virtual antenna. The TR spatial-temporal resonance is indeed a resonance of EM field in response to the propagation environment, and it changes whenever the propagation environment changes.

Inspired by the principle of TR and motivated by the development of IoT, in this dissertation, we propose several radio analytic systems that leverage multipath information to realize IoT applications of recognizing different events and identifying people in an indoor environment. In the first part, we design three indoor monitoring systems that analyze different event-determined features extracted from either a single CSI sample or a CSI time series. The first proposed indoor monitoring system distinguishes between different indoor events by matching the instantaneous CSI to a multipath profile calibrated in a training database whose similarity is quantified by the time-reversal resonance strength (TRRS). Later on, we derive the statistics of TRRS, and we propose a new TR based indoor monitoring system that differentiates between different indoor events based on the statistical behavior of TRRS. Unlike the previous two indoor monitoring systems which treats each CSI as an independent feature, we propose the third indoor monitoring system by exploiting the temporal information embedded in the CSI time series as an additional feature to comprehensively understand indoor events. Results of extensive experiments demonstrate the proposed systems as promising solutions to future indoor monitoring IoT applications.

In the second part of this dissertation, we propose the concept of human radio biometrics and design a through-the-wall human identification system that is implemented on commercial WiFi devices. As a human present in an indoor environment, the radio waves propagate around will interact with the human body through reflections and scatterings. We define human radio biometrics as the attenuation and alteration of wireless signals brought by human. We achieve an accurate through-the-wall human recognition by utilizing the fact that the radio biometrics are uniquely determined by the biological characteristics of each human. Through extensive experiments, we validate the existence of radio biometrics and evaluate the accuracy of the proposed human identification system. Unlike conventional approaches for biometric recognition, the proposed radio biometrics system can identify human through a wall and supports commercial WiFi infrastructure, thus illustrating its potential for smart IoT applications.

RADIO ANALYTICS FOR INDOOR MONITORING AND HUMAN RECOGNITION

by

Qinyi Xu

Dissertation submitted to the Faculty of the Graduate School of the
University of Maryland, College Park in partial fulfillment
of the requirements for the degree of
Doctor of Philosophy
2018

Advisory Committee:
Professor K. J. Ray Liu, Chair/Advisor
Professor Min Wu
Professor Gang Qu
Dr. Beibei Wang
Dr. Zoltan Safar
Professor Lawrence C. Washington

Dedication

To my family —

Hong Fang, Xiaosu Xu,

and Ruichi Yu.

Acknowledgments

First and foremost, I would like to express my sincerest appreciation and gratitude to my advisor Prof. K. J. Ray Liu for providing not only academic support for my research and study but also personal and emotional support for my life. Over the past five years, his consideration, encouragement and guidance have made me accomplish so much that I could have never foreseen when I first joined the group. His patience, motivation, enthusiasm, immense knowledge and pursuit of excellence on academic and research not only have ignited my passion and guided me in all the time of research, but also have a profound influence in my professional and personal development as a role model.

I would like to thank all of my dissertation committee members. I am grateful to Dr. Beibei Wang for her continuous support for my research and enlightening discussions on research, and thankful to Dr. Zoltan Safar for generously sharing with me his invaluable research and industry experience. I am also thankful to Prof. Min Wu who has provided me with many research ideas and suggestions. My sincere thanks also goes to Prof. Gang Qu and Prof. Lawrence Washington for their time and efforts serving on my dissertation committee and reviewing my thesis.

I would also like to acknowledge help and support from all members in our Signals and Information Group. I have learned so much from Dr. Yan Chen for his mentorship and collaboration on research. Thanks go to Dr. Hung-Quoc Lai, Dr. Yi Han, Dr. Zhung-Han Wu for their precious support on hardware implementation. I also wish to give my thanks to Chen Chen, Feng Zhang, Deepika, Regani, Chau-

Wai Wong, Chunxiao Jiang, Xuanyu Cao, Xiaoyu Chu, and Hang Ma for various thoughtful discussions, support and the wonderful time during the past few years.

I owe my deepest thanks to my family – my parents Hong Fang, Xiaosu Xu, and my husband Ruichi who have always stood by me. Without their unconditional love and strong support, I would not have been able to walk through my oversea graduate years to this important achievement. Words cannot express the gratitude I owe them. This dissertation is dedicated to them.

Table of Contents

Dedication ii

Acknowledgements iii

List of Tables ix

List of Figures x

List of Abbreviations xii

1 Introduction 1
- 1.1 Motivation . . . 1
- 1.2 Related Works on Indoor Wireless Sensing . . . 4
- 1.3 Dissertation Outline and Contributions . . . 6
  - 1.3.1 Multipath as Virtual Antenna: Time-Reversal Solution (Chapter 2) . . . 7
  - 1.3.2 Indoor Event Detection with Time-Reversal Space (Chapter 3) 7
  - 1.3.3 Indoor Monitoring: Statistical Learning over Time-Reversal Space (Chapter 4) . . . 8
  - 1.3.4 Indoor Monitoring: Training with Continuous Channel State Information (Chapter 5) . . . 8
  - 1.3.5 Radio Biometrics: Human Recognition Through a Wall (Chapter 6) . . . 9

2 Multipath as Virtual Antenna: Time-Reversal Solution 11
- 2.1 Multipath . . . 12
  - 2.1.1 Multipath Channel Profile . . . 14
- 2.2 Time-Reversal Resonance . . . 15
  - 2.2.1 Overview of Time-Reversal Technique . . . 16
  - 2.2.2 Time-Reversal Space . . . 17
  - 2.2.3 Time-Reversal Resonance . . . 19
    - 2.2.3.1 Calculating Time-Reversal Resonance Strength with Channel Impulse Response . . . 19
    - 2.2.3.2 Calculating Time-Reversal Resonance Strength with Channel Frequency Response . . . 20
- 2.3 Summary . . . 22

3 Indoor Event Detection with Time-Reversal Space 23
- 3.1 Proposed Algorithms . . . 25
  - 3.1.1 Phase 1: Offline Training . . . 25
  - 3.1.2 Phase 2: Online Testing . . . 27
- 3.2 Experimental Results . . . 29
  - 3.2.1 Experimental Setting . . . 30

3.2.2 Feasibility Validation . . . 31
3.2.3 Single Door Monitoring . . . 33
3.2.3.1 LOC A: NLOS case . . . 34
3.2.3.2 LOC B: LOS and NLOS case . . . 35
3.2.3.3 LOC C: LOS case . . . 37
3.2.4 TRIEDS in Controlled Environments . . . 38
3.2.4.1 Evaluations on LOC B . . . 39
3.2.4.2 Evaluations on LOC C . . . 42
3.2.5 TRIEDS in Normal Office Environments . . . 44
3.2.6 TRIEDS with Intentional Human Movements . . . 46
3.2.7 For through-the-wall Guard . . . 50
3.3 Discussion . . . 52
3.3.1 Impact of System Parameters . . . 52
3.3.2 Impact of Human Motion Interference . . . 52
3.4 Summary . . . 54

4 Indoor Monitoring: Statistical Learning over Time-Reversal Space 55
4.1 System Model . . . 56
4.1.1 Statistics of TRRS . . . 57
4.2 Proposed Algorithms . . . 61
4.2.1 TRIMS: Event Detector . . . 62
4.2.1.1 Offline Training Phase . . . 62
4.2.1.2 Online Monitoring Phase . . . 66
4.2.2 TRIMS: Motion Detector . . . 68
4.2.2.1 Phase I. Offline Training . . . 69
4.2.2.2 Phase II. Online Monitoring . . . 71
4.2.3 TRIMS: Time Diversity for Smoothing . . . 71
4.3 Experimental Results . . . 73
4.3.1 Experimental Setting . . . 73
4.3.2 TRIMS: Event Detection Performance . . . 74
4.3.2.1 Study on Location of TX-RX . . . 75
4.3.2.2 Operational Test in House #1 . . . 77
4.3.2.3 Long-Term Test in House #1 . . . 79
4.3.2.4 Operational Test in House #2 . . . 80
4.3.2.5 Long-Term Test in House #2 . . . 81
4.3.3 TRIMS: Motion Detection Performance . . . 84
4.4 Discussion . . . 86
4.4.1 Retraining TRIMS . . . 86
4.4.2 Monitoring with Multiple Transmitters . . . 87
4.4.3 Detecting Dynamic Events . . . 88
4.4.4 Identifying Motion . . . 88
4.4.5 Potential of TRIMS . . . 88
4.5 Summary . . . 89

5 Indoor Monitoring: Training with Continuous Channel State Information 91
5.1 System Model . . . 92
5.1.1 Multi-Antenna Diversity . . . 95
5.2 Proposed Algorithms . . . 96
5.2.1 Algorithms for Feature Extraction . . . 97
5.2.1.1 Refinement of CSI Time Series . . . 97
5.2.1.2 Denoising and Compact Representation . . . 100
5.2.2 Algorithms for Real-Time Monitoring . . . 102
5.2.2.1 Challenges in Real-Time Monitoring . . . 102
5.2.2.2 Monitoring with Partial Training Information . . . 104
5.2.2.3 Similarity Comparison with Event Inconsistency . . . 105
5.2.3 Algorithms for Unsupervised Retraining . . . 107
5.3 Experimental Results . . . 109
5.3.1 Experimental Setting . . . 110
5.3.2 Robustness to Event Inconsistency . . . 112
5.3.3 Robustness to Outside Activities . . . 113
5.3.4 Robustness to Inside Activities . . . 114
5.3.5 Long-Term Performance . . . 116
5.4 Discussion . . . 118
5.4.1 Impact of Sliding Window Length . . . 118
5.4.2 Impact of Unsupervised Retraining . . . 120
5.4.3 Potential for Smart Home . . . 121
5.5 Summary . . . 121

6 Radio Biometrics: Human Recognition Through a Wall 123
6.1 System Model . . . 127
6.2 Radio Biometric Refinement Algorithms . . . 130
6.2.1 Phase Alignment Algorithm . . . 133
6.2.2 Background Subtraction Algorithm . . . 134
6.2.3 Identification Methodology . . . 136
6.3 Experimental Results . . . 137
6.3.1 Experimental Setting . . . 137
6.3.2 Study on Background Subtraction . . . 139
6.3.2.1 Background Selection . . . 141
6.3.2.2 Background Subtraction Factor . . . 142
6.3.3 Study on TX-RX Locations . . . 143
6.3.3.1 Special Case Study . . . 145
6.3.4 Human Identification . . . 147
6.3.5 Human Verification . . . 148
6.3.5.1 Stationarity over Time . . . 148
6.3.5.2 Other Variations . . . 149
6.4 Discussion . . . 151
6.4.1 Impact of Obstructions . . . 152
6.4.2 Impact of Human Postures . . . 154
6.4.3 Comparison with RSSI-based Approach . . . 157

6.4.3.1 RSSI for Identification . . . 157
6.4.3.2 RSSI for Verification . . . 158
6.4.4 Limitations . . . 160
6.5 Summary . . . 162

7 Conclusions and Future Work 163
7.1 Conclusions . . . 163
7.2 Future Work . . . 166

Bibliography 169

List of Tables

3.1 Performance of the proposed TRIEDS in easy case. 32
3.2 State list for TRIEDS to detect. 39
3.3 False alarm and detection probability for multi-event detection on LOC B in controlled environment. 43
3.4 False alarm and detection probability for multi-event detection on LOC C in controlled environment. 47
3.5 False alarm and detection probability for multi-event detection on LOC B in normal environment. 47
3.6 False alarm and detection probability for multi-event detection on LOC C in normal environment. 48
3.7 State list for study on human movements. 48
3.8 Accuracy comparison of TRIEDS under human movements. 49

4.1 Events of interest in House #1. 75
4.2 Events of interest in House #2. 81
4.3 Detection rate for motion at different locations under 0 false alarm rate. 85

5.1 Long-term test results. 117
5.2 Long-term test result without unsupervised retraining for dynamic events. 120
5.3 Smart office analysis. 121

6.1 Physical characteristics of test subjects in human identification experiment. 138
6.2 Performance matrix of individual identification with and without background subtraction. 140
6.3 Comparison on performance matrices with fixed threshold $\mu = 0.9$. . . 145
6.4 Comparison on performance matrices with the minimum diagonal element larger than 99%. 145
6.5 Performance matrix for stationarity study. 149
6.6 List of the six variation classes. 150
6.7 Identification rate under variations. 151
6.8 Confusion matrix under RSSI-based approach. 159

List of Figures

1.1 Illustration of an indoor multipath environment. 2

2.1 Illustration of virtual antennas. 13
2.2 Mapping between the physical space and the TR space. 18

3.1 An example of indoor CSI. 26
3.2 Prototype of TRIEDS. 29
3.3 Experimental setting for TRIEDS: floorplans 31
3.4 Experimental setting for TRIEDS: devices. 32
3.5 Multipath profiles (amplitude part) of door D1 under LOC A. 35
3.6 Multipath profiles of door D1 for LOC B under NLOS and LOS scenarios. 36
3.7 Multipath profiles (amplitude part) of door D1 under LOC C. 38
3.8 Resonance strength map with RX on LOC B and TX on the 1^{st} green dot (axis 1). 40
3.9 ROC curve for distinguishing between S_1 and S_2 under LOC B. . . . 41
3.10 ROC curve for distinguishing between S_1 and S_9 under LOC B. . . . 42
3.11 Resonance strength map with RX on LOC C and TX on the 1^{st} green dot (axis 1). 44
3.12 ROC curve for distinguishing between S_1 and S_2 under LOC C. . . . 45
3.13 ROC curve for distinguishing between S_1 and S_9 under LOC C. . . . 46
3.14 Experiment setting for study on human movements. 49
3.15 Experiment setting for guard test. 50
3.16 Resonating strength of guard system. 51

4.1 Examples for evaluating the derived statistical model. 60
4.2 Diagram of the proposed event detector in TRIMS. 63
4.3 Diagram of the proposed motion detector in TRIMS. 69
4.4 Experimental setting for TRIMS: floorplans. 73
4.5 ROC performance for the proposed event detector. 74
4.6 System output of the proposed event detector for operational tests in House #1. 78
4.7 System output of the proposed event detector for operational tests in House #2. 82
4.8 System output of the proposed event detector for long-term tests in House #2. 83

5.1 System diagram. 97
5.2 Waveform Spectrogram: example of waveform series before and after low pass filtering. 98
5.3 Waveform Spectrogram: example of waveform series before and after PCA. 101
5.4 Illustration of event inconsistency. 103

5.5 Illustration of monitoring with partial information by sliding window. 104
5.6 Experimental setting: floorplans. 111
5.7 Experimental results: robustness to event inconsistency in setting 1. . 112
5.8 Experimental results: robustness to outside activities (Experiment 1). 113
5.9 Experimental results: robustness to outside activities (Experiment 2). 114
5.10 Experimental results: robustness to inside activities (Scenario 1). . . 115
5.11 Experimental results: robustness to inside activities (Scenario 2). . . 115
5.12 Experimental results: robustness to inside activities (Scenario 3). . . 116
5.13 Examples of feature series generated by Algorithm 2. 117
5.14 Experimental results: impact of sliding window length. 119

6.1 RF reflections and scattering. 128
6.2 TRRS map for each link. 131
6.3 Comparison on TRRS maps with and without background subtraction. 136
6.4 Experiment setting: floorplan and device. 138
6.5 Experiment setting for background subtraction study. 140
6.6 Evaluation on ROC curves for background selection. 142
6.7 Evaluation on ROC curves for background subtraction factor. 143
6.8 Evaluation on ROC curves for different TX-RX locations. 144
6.9 ROC curve of identifying 11 individuals. 147
6.10 Comparison on TRRS map for stationarity study. 149
6.11 TRRS map of variation. 150
6.12 Study on impacts of obstructions: test floorplan. 152
6.13 Study on impacts of obstructions: different obstructions. 152
6.14 Study on impacts of obstructions: ROC curves with different obstructions. 154
6.15 Study on human pose effects: test poses. 155
6.16 Study on human pose effects: ROC curves with different poses. 156
6.17 RSSI values variation of 11 individuals. 157
6.18 RSSI values comparison on stationarity. 158
6.19 RSSI values comparison on variations. 159

List of Abbreviations

AoA	Angle of arrival
CDF	Cumulative distribution function
CFO	Carrier frequency offset
CFR	Channel frequency response
CIR	Channel impulse response
CSI	Channel state information
DTW	Dynamic time warping
E-CDF	empirical cumulative distribution function
EM	Electromagnetic
FFT	Fast Fourier transform
GHz	Gigahertz
IoT	Internet of Things
ISM	Industrial, scientific, and medical radio band
K-S test	Kolmogorov-Smirnov test
kNN	k nearest neighbors
LOS	Line of sight
MIMO	Multiple input multiple output
MHz	Megahertz
NLOS	Non line of sight
OFDM	Orthogonal frequency-division multiplexing
PCA	Principal component analysis
RF	Radio frequency
ROC	Receiver operating characteristic
RSS	Received signal strength
RSSI	Received signal strength indicator
RX	Receiver
SFO	Sampling frequency offset

SNR	Signal-to-noise radio
STO	Symbol timing offset
ToF	Time of flight
TR	Time-Reversal
TRRS	Time reversal resonance strength
TX	Transmitter
UWB	Ultra-wide band

Chapter 1

Introduction

1.1 Motivation

In the era of Internet of Things (IoT), technologies and systems have been developed to understand and decipher the surrounding environment, by answering the question of who, what, when, where, and how of everything happening. Since the past decade, billions of smart objects, a.k.a. the "things", have been deployed around each individual. Including household appliances, phones and tablets, vehicles, and almost everything that we can think of, those smart objects can communicate and exchange data with each other through internet. As the things form a giant network, it will be possible to comprehensively track and measure people's daily life, and even monitor the entire world through IoT.

Thanks to the ubiquitous deployment of wireless radio devices and the development of emerging wireless sensing technologies, it has enabled a plenty of IoT applications that utilize wireless signals, or more specifically the wireless channel state information (CSI), to perceive the information hidden in the indoor environment. The feasibility of wireless passive sensing relies on multipath propagation. Multipath propagation is the phenomenon that a transmitted wireless signal reaches

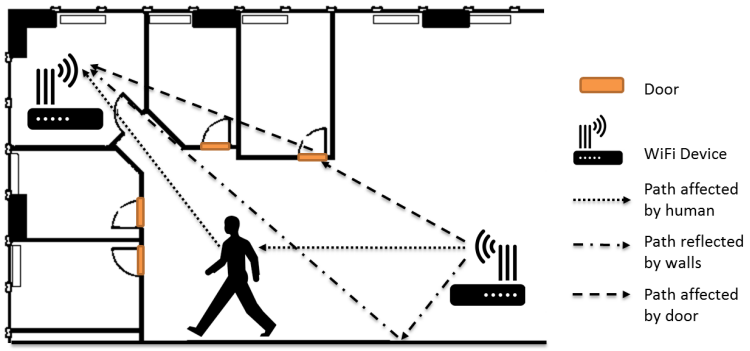

Figure 1.1: Illustration of an indoor multipath environment.

the receiver through different paths after being reflected and scattered by different objects in the indoor environment. A typical indoor multipath environment is demonstrated in Figure 1.1, where the channel between the transmitter (TX) and the receiver (RX) consists of paths affected by: 1) walls, 2) doors of each room and 3) a present human being. Hence, as long as one of those three factors changes, the channel changes accordingly and is revealed in the CSI. By deploying wireless transceivers indoors, both macro changes introduced by human activities and moving objects, and micro changes generated by gestures and vital signals, can be extracted from the CSI and recognized through wireless sensing. Hence, analyzing how multipath propagation reacts to human activities and indoor objects can enrich one's insight into surrounding environments and activities, consequently extending human senses.

Recently, time-reversal (TR) technique has been proposed as a promising approach for IoT applications by treating each path of the multipath channel in a rich scattering environment as a widely distributed virtual antenna [1, 2]. By leverag-

ing and controlling the virtual antenna, TR technique provides a high-resolution spatial-temporal resonance. Because it is indeed a resonance of the electromagnetic (EM) wave to the propagation environment, TR resonance, inherently, is capable of responding to, indicating and differentiating environmental changes promptly. Inspired by the principle of TR, *radio analytics* is proposed as the technique or the solution that can decipher radio waves to reveal activities and environmental information around us [2].

The past few decades have witnessed the surging demand of surveillance systems which aims to recognize individual identities and detect different indoor events. On one hand, most indoor surveillance systems, nowadays, basically rely on video recording and require cameras deployments in target areas. Techniques in computer vision and image processing are applied on the captured videos to extract information for real time detection and analysis [3–6]. However, conventional vision-based indoor monitor systems have many limitations, including privacy violation, susceptibility to malicious attack and indispensable requirements of LOS and illumination.

On the other hand, the capability of performing reliable human identification and recognition has become a crucial requirement in many applications, such as forensics, airport custom check, and bank securities. The well-known biometrics for human recognition include fingerprint, face, iris, and voice, which are inherent and distinctive to an individual. Even though the current biometrics systems are accurate and can be applied in all environments, all of them require special devices that capture human biometric traits in an extremely LOS environment, i.e., the subject should make contact with the devices.

Motivated and inspired by the aforementioned problems in current indoor monitoring and human identification applications, in this dissertation, we will illustrate how radio analytics can be used to achieve high-accuracy indoor monitoring and human recognition with WiFi. Because of the inherent characteristics of wireless signals, the proposed indoor monitoring systems and human identification system can work under non line-of-sight (NLOS) scenario with low complexity algorithms.

1.2 Related Works on Indoor Wireless Sensing

Sensing with the wireless signals to detect indoor events has gained a lot of attention [7]. By utilizing the fact that the received radio frequency (RF) signals can be altered by the propagation environment, device-free indoor sensing systems are capable of capturing activities in the environment through the changes in received RF signals. Existing research on wireless passive sensing can be categorized into different groups based on the features extracted from the wireless channel. To begin with, traditional wireless passive sensing systems are mainly based on the received signal strength (RSS) [8–11]. However, due to the fact that the RSS is coarse-grained and can be easily corrupted by multipath effect, RSS-based sensing systems often require a line-of-sight (LOS) transmission, resulting in a limited accuracy in indoor activity detection.

In order to improve the accuracy and expand the applicable scenario of traditional wireless passive sensing, a much more informative feature, the CSI, becomes prevalent. Since the CSI is typically of high dimensions, it contains more detailed

information and thus supports fine-grained classification applications. By analyzing the variations and statistics of CSI, systems have been built to detect indoor human motions [12–15] and small hand motions [16, 17]. Among most of those works only amplitude of the CSI was used to detect indoor activities, while ignoring the information in the phase, due to the randomness of phase distortion in the CSI. Later in [18–23], the first two largest eigenvalues of the CSI correlation matrix were treated as features and a support vector machine (SVM) classifier was trained to detect the presence of moving human. Although both the amplitude and phase information of the CSI was utilized in [18], it can only differentiate between the static and dynamic states in a LOS setting and the phase information was sanitized through linear fitting which has notable drawbacks. A home intrusion detection system has been proposed in [24] which treated the amplitude of the CSI as the feature, lacking study of the false alarm rate and long-term performance.

Moreover, doppler frequency introduced by moving objects has been extracted from CSI and one could utilize it to detect motion or motion directions [25–27]. However, in order to get accurate Doppler shift frequency, either a high sounding rate over 1 kHz or a strict LOS transmission is required. In [9, 28, 29], falling down detection systems have been implemented by analyzing the statistical behavior of CSI captured within a certain time window, which is useful in elderly monitoring and well-being applications.

Another category of wireless passive sensing techniques relies on the time-of-flight (ToF) information embedded in received signals to track changes of reflected objects for motion detection or vital sign monitoring. Due to the fact the the

spatial resolution of CSI is inversely proportional to the bandwidth, in order to extract the fine-grained ToF information, it often requires either extremely large sensing bandwidths [30–32], or specially designed frequency-modulated continuous-wave (FMCW) signals [33–37]. Hence, those techniques cannot be implemented on off-the-shelf WiFi devices and their ability of detecting multiple indoor events has not been studied yet.

1.3 Dissertation Outline and Contributions

Considering the limitations of current studies discussed in Section 1.2 and the proliferation of IoT applications in indoor monitoring and human identification, we are motivated to develop new radio analytic techniques that can not only fully utilize the information embedded in multipath channels, but also support simple implementation with commercial WiFi devices.

In this dissertation, we first introduce how to use TR technique to utilize and analyze indoor multipath profiles for indoor multi-event detection and real-time indoor monitoring. We propose three different indoor monitoring systems that exploit CSI with different radio analytic methods, in Chapter 3, Chapter 4, and Chapter 5. In the second part of this dissertation (Chapter 6), we will introduce the concept of radio biometrics and describe a system that realizes through-the-wall human recognition based on biometric information recorded in WiFi signals. The rest of this dissertation is organized as follows.

1.3.1 Multipath as Virtual Antenna: Time-Reversal Solution (Chapter 2)

In this chapter, we elaborate on the fundamental theory behind the proposed radio analytic systems, including multipath propagation and TR technique. Since each indoor event and/or person present in an indoor environment is associated with a unique multipath profile and can be mapped in to a distinct point in the TR space, the similarity between two indoor events and/or different individuals can be quantitatively measured through time-reversal resonance strength (TRRS). We define and present the TRRS calculation that will be used in this dissertation.

1.3.2 Indoor Event Detection with Time-Reversal Space (Chapter 3)

In this chapter, we propose a novel wireless indoor events detection system, TRIEDS. By leveraging TR technique to capture changes in the CSI of the indoor environment, TRIEDS enables low-complexity single-antenna devices that operate in the ISM band to perform through-the-wall indoor multiple events detection. In TRIEDS, each indoor event is detected by matching the instantaneous CSI to a multipath profile calibrated in a training database using TRRS as the similarity measurement. To validate the feasibility of TRIEDS and to evaluate the performance, we build a prototype that works on ISM band with carrier frequency being 5.4 GHz and a 125 MHZ bandwidth. Experiments are conducted to detect the states of the indoor wooden doors. Compared with previous works on indoor monitoring systems which require multiple antennas, dedicated sensors, ultra-wideband transmission or

LOS environment, and rely on only the amplitude information in the CSI, TRIEDS introduces a novel and practical solution to the indoor monitoring system which can support through-the-wall detection and only requires low-complexity single-antenna hardware operating in the ISM band.

1.3.3 Indoor Monitoring: Statistical Learning over Time-Reversal Space (Chapter 4)

In this chapter, we propose a new TR based indoor monitoring system, TRIMS, which utilizes both the amplitude and the phase information in the CSI obtained from off-the-shelf WiFi devices to monitor indoor environments in real time under both LOS and NLOS sensing scenarios. Unlike the system proposed in Chapter 3 that uses the TRRS directly as a similarity score for differentiating between events, TRIMS achieves indoor multiple events detection and human motion monitoring by analyzing the statistical behavior of TRRS. The statistics of TRRS is derived in this chapter and the performance of TRIMS is evaluated and verified through intruder detection experiments conducted in different single family houses with resident activities.

1.3.4 Indoor Monitoring: Training with Continuous Channel State Information (Chapter 5)

In this chapter, we propose an indoor monitoring system that monitors the occurrence of different indoor events in real time with commercial WiFi devices, by

exploiting the temporal information embedded in the CSI time series. Since the occurrence of an indoor event lasts for a certain period and shares a similar transition of indoor intermediate states among different instances, event-related information is embedded not only in each CSI sample but also in how CSI changes along time. Instead of treating each CSI as an independent feature (Chapter 3 and Chapter 4), in this chapter, the time series of CSI samples captured continuously is used for identifying and classifying different indoor events. Algorithms are designed to extract the most distinct and representative feature sequence and a modified classifier based on the k-nearest-neighbor (kNN) is proposed to overcome the perturbation and divergence in the real-time measured features. Moreover, we propose unsupervised auto-retraining algorithms to improve the system robustness in long-term experiments. We use the door opening and close in smart home scenario as a representative set of events to study the CSI time series classification, and the technique can be generalized to other types of events.

1.3.5 Radio Biometrics: Human Recognition Through a Wall (Chapter 6)

In this chapter, we present a TR human identification system which identifies individuals through the wall, based on the human radio biometrics extracted form WiFi signals. We introduce for the first time the concept of human radio biometrics, which account for the wireless signal attenuation and alteration brought by human. Through experiments, its existence has been verified and its capability in

human identification has been illustrated. The procedure to collect human radio biometrics is named as radio shot. Due to the fact that the dominant component in the CSI comes from the static environment rather than the human body, the human radio biometrics are embedded and buried in the multipath CSI. To boost the identification performance, we design novel algorithms for extracting individual human radio biometrics from the wireless channel information. With the help of TR technique and TRRS, human radio biometrics are differentiated between different people. Extensive experiments have been conducted using a prototype built on commercial WiFi devices and results demonstrate the potential of using commercial WiFi signals to capture human radio biometrics for individual identifications.

Chapter 2

Multipath as Virtual Antenna: Time-Reversal Solution

The nature provides a large number of degrees of freedom by means of radio multipath propagation. Through channel sounding, real-time CSI can be estimated which records information of all scatterers in the multipath propagation environment. TR technique treats each path of the multipath channel in a rich scattering environment as a widely distributed virtual antenna and provides a high-resolution spatial-temporal resonance, commonly known as the focusing effect [1]. As long as a change occurs on either the device or any scatterer in the environment, the corresponding multipath channel between the TX and the RX changes accordingly. Consequently, the TR spatial-temporal resonance changes, which conversely indicates changes in the propagation environment. In physics, the TR spatial-temporal resonance can be viewed as the result of the resonance of electromagnetic (EM) field in response to the environment [38].

Inspired by the fundamental physical principle of TR, *Radio analytics* has been proposed an emerging technology that infers the propagation environment and extends the human sense over the world [2]. As fully exploiting the rich multipath CSI, various types of analytics based on the wireless channel state information (i.e., radio analytics) has been developed to enable many cutting-edge IoT applications,

including the indoor monitoring systems and human recognition systems proposed in this dissertation.

In this chapter, we give a detailed introduction to the fundamental theory behind the proposed radio analytics: indoor monitoring systems and human recognition systems. The rest of this chapter is organized as follows. The idea of multipath propagation is introduced in Section 2.1, where we explain how to treat each multipath component as a virtual antenna. In Section 2.2, we provide an overview for TR technique, introduce the concept of TR space, and define the calculation of time-reversal resonance strength (TRRS). We summarize this chapter in Section 2.3.

2.1 Multipath

As the transmit signal encounters different scatterers in the environment and thus travels through different paths during its propagation, the channel between each TX and RX antenna is a multipath channel.

Because an attenuated copy of the original signal is generated and transmitted through a different path when the transmit signal gets reflected or scattered by a scatterer, each scatterer in the environment can be viewed as a virtual antenna that transmits directly to the RX, in addition to the TX. Moreover, the channel characteristics between the virtual antenna and the RX antenna are determined by both of the radio paths between the TX and the scatterer and between the scatterer and the RX. An illustration of scatterers as virtual antennas in a multipath propagation

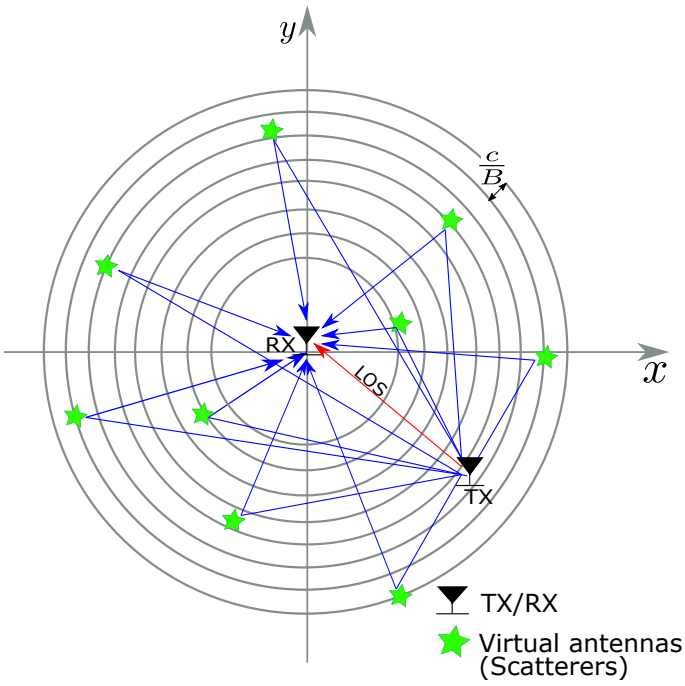

Figure 2.1: Illustration of virtual antennas.

environment is depicted in Figure 2.1, where the red arrow represents the LOS path and the blue arrows represent paths reflected and scattered by scatterers. Green stars in Figure 2.1 represent scatterers in the environment, which can be viewed as virtual antennas that transmit an attenuated signal to the RX. All paths together form a multipath channel between the TX and the RX [39].

The multipath can be effectively harvested by adjusting transmission power and bandwidth [40, 41]. On one hand, a higher transmission power can lead to a higher SNR. Consequently, the higher the transmission power is, the more observable multipath components are. On the other hand, the spatial resolutixon in resolving independent multipath components, i.e., the resolution to separate radio paths with different lengths in a multipath propagation, is limited by c/B as marked in Figure 2.1, with c being the speed of light and B being the bandwidth. Therefore, the

larger the bandwidth is, the better the spatial resolution is and thus the more multipaths can be revealed. The mathematical explanation of the relationship between bandwidth and multipath resolution is as follows.

2.1.1 Multipath Channel Profile

In an environment with K_{max} independent multipath components existing between the TX and the RX, the continuous-time multipath channel $h(t)$ is defined as collections of different radio propagation paths, i.e.,

$$h(t) = \sum_{k=1}^{K_{max}} \alpha_k \delta(t - \tau_k), \tag{2.1}$$

where K_{max} is the number of scatterers in the wireless transmission medium. α_k is the multipath coefficients of scatterer k, and τ_k is the time delay associated with α_k. The function $\delta(\cdot)$ is the delta function. Note that, the delay spread of the channel is $\tau = \max_k \tau_k$.

However, due to the limited bandwidth W, the estimated discrete-time channel $\mathbf{h}_T$ at the receiver side is a sampled version of $h(t)$, i.e.,

$$h_T[l] = \int_{\frac{l-1}{W}}^{\frac{l}{W}} P\Big(\frac{l}{W} - t\Big) h(t) dt, l = 0, 2, \cdots, L-1, \tag{2.2}$$

where $P(\cdot)$ is the window function with length $1/W$.

Given a delay spread τ, when $W \leq 1/\tau$, only a single tap is resolved as the integration of all multipaths. When $W > 1/\tau$, multipath signals received within $1/W$ seconds will be integrated into a single tap signal. Consequently, all multipaths can be resolved when $W > 1/\Delta\tau_{\min}$, where $\Delta\tau_{\min}$ represents the smallest difference in

ToF of consecutively received multipath signals. Because signals with ToF difference equal to or larger than $1/W$ can be separated under a bandwidth W, a larger bandwidth enables a higher sampling rate to sample analog signals received from different paths and resolve more multipath components. Therefore, the number of resolved channel taps, i.e. length of vector $\mathbf{h}_T$, is determined by $L = \text{round}(\tau W)$, as long as K_{max} is large enough to provide enough multipaths whose time delay difference $\Delta\tau_{\min}$ is close to 0.

Hence, the larger the bandwidth is, the better the spatial resolution is and thus the more multipaths can be revealed. The performance of wireless sensing depends greatly on how rich the CSI can be. In the LTE standard the bandwidth is 20MHz, and in WiFi (the IEEE 802.11n standard) systems the bandwidth is 40 MHz. Moreover, the entire ISM 5G band occupies a total of 125MHz bandwidth. As projected in 5G, high carrier frequencies with larger bandwidths will be adopted in the future wireless communication systems [42], which makes the multipath channel of a good spatial resolution feasible. With more and more bandwidth readily available for the next generation of wireless sensing, many more smart applications/services will come true, because richer information becomes available with a wider bandwidth.

2.2 Time-Reversal Resonance

In this section, we review the history of TR technique and introduce the concept of TR space. Multipath profile records changes occurring in the indoor environment, as well as the radio biometric information, i.e., how EM wave interacts

with human bodies. Each indoor event and/or person in the indoor environment can be represented by a multipath profile, corresponding to a point in the TR space. If there is a new event or person shows to affect the indoor propagation environment, current multipath profile changes and fails to generate a high spatial-temporal resonance with the one mapped in the TR space. With the notion of a TR space, the similarity between two indoor events and/or individuals can be evaluated quantitatively and perform indoor event detection and human recognition.

2.2.1 Overview of Time-Reversal Technique

TR signal processing technique is originally proposed in 1957 to compensate the delay distortion in picture transmission [43]. Then, its applications in acoustic communications has been studied, and it is validated through a series of theoretical and experimental works that the energy of the TR acoustic wave is only focused at the intended locations [44–52].

Later, applications of TR technique in wireless communications have received an increasing attention. In [38, 53–58], the study of TR signal transmission has been extended to applications related to the electromagnetic (EM) field, which demonstrates the TR resonance through experiments and justifies the assumption of channel stationarity and channel reciprocity given that the coherence time is long enough. Meanwhile, the performance of TR technique has been studied in UWB [59–63], and with MIMO technology [56, 64–67].

Recently, experiments as well as theoretic analysis have been conducted to

illustrate the potential of TR for future green communications [68, 69]. Later on, the concept of time-reversal division multiple access was proposed and a system-level performance analysis was provided in [70]. Moreover, TR waveforming [39,68,71–75] has been proposed as a novel technique to control virtual antennas distributed in the environment to take advantages of the spatial diversity and thus achieve a high degree of freedom.

On the other hand, TR technique can be utilized to detect and track the changes in a multipath propagation environment with a high accuracy. As capable of accurately detecting changes in the wireless environment, TR technique was presented as a promising technique for green Internet of things (IoT) [76] and has been applied to applications for indoor locationing that achieves a centimeter level accuracy [77–80], indoor speed estimation [81], through-the-wall event detection [82–84], human recognition [85] and breathing rate estimation [86].

2.2.2 Time-Reversal Space

The TR space is used to represent and separate different indoor propagation environments. The details are as follows.

During the wireless transmission, signals encounter different objects in the environment, and the corresponding propagation path and characteristics change accordingly before arriving at the receiver. Hence, each channel multipath profile is uniquely determined by the indoor environment. As demonstrated in Figure 2.2, each dot in the physical space represents an indoor location or a snapshot of an

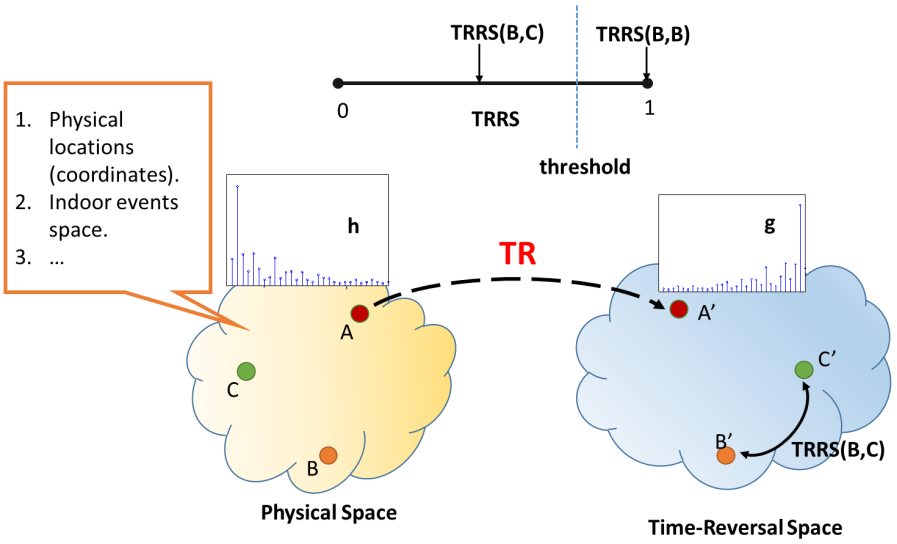

Figure 2.2: Mapping between the physical space and the TR space.

indoor environment, which uniquely determine a multipath profile $h(t)$. By taking a time-reverse and conjugate operation over the multipath profile, the corresponding TR signature $g(t)$ is generated. Consequently, each of the points in the physical space as marked by "A", "B", and "C" is mapped into the TR space as "A'", "B'", and "C'". When the TR signature is transmitted through a wireless channel, a unique peak will be generated at the receiver side, known as the spatial focusing effect, only if the current indoor environment matches the signature.

Therefore, in the TR space, the similarity between two indoor events and/or radio biometrics can be quantified by TRRSs. The higher the TRRS is, the more similar two indoor events and/or radio biometrics are. Similar events or radio biometric information constrained by a threshold on TRRS can be viewed as coming from the same class. By leveraging the high degrees-of-freedom in multipath information using TR techqniue, we can monitoring indoor environment and detecting

event occurrence in real time. Moreover, wireless human recognition is accomplished by deciphering the radio biometric information embedded in the CSI.

2.2.3 Time-Reversal Resonance

When the propagation environment changes, the involved multipath signal varies correspondingly and consequently the spatial-temporal resonance as well as TRRS also changes. In this part, we define the TRRS and provide the calculation details for time domain CSI and the frequency domain CSI.

2.2.3.1 Calculating Time-Reversal Resonance Strength with Channel Impulse Response

When sensing in the time domain, the CSI is in the form of the channel impulse response (CIR), $\mathbf{h}_T = \Big[h_T[0], h_T[2], \cdots, h_T[L-1]\Big]$, as defined in (2.2) and the subscript $(\cdot)_T$ denotes the time domain CSI. The definition of the TRRS is given as follows.

Definition: The TRRS $\mathcal{TR}(\mathbf{h}_{T,1}, \mathbf{h}_{T,2})$ between two CIR samples $\mathbf{h}_{T,1}$ and $\mathbf{h}_{T,2}$ is defined as

$$\mathcal{TR}(\mathbf{h}_{T,1}, \mathbf{h}_{T,2}) = \frac{\max\limits_{i} \Big|(\mathbf{h}_{T,1} * \mathbf{g}_{T,2})[i]\Big|^2}{\Big(\sum_{l=0}^{L-1} |h_{T,1}[l]|^2\Big)\Big(\sum_{l=0}^{L-1} |h_{T,2}[l]|^2\Big)}, \tag{2.3}$$

where "$*$" denotes the convolution and $\mathbf{g}_{T,2}$ is the TR signature of $\mathbf{h}_{T,2}$ as,

$$g_{T,2}[k] = h^*_{T,2}[L-k-1], \ k = 0, 1, \cdots, L-1, \tag{2.4}$$

where $(\cdot)^*$ denotes taking conjugation.

The resonating strength defined in (2.3) is similar to the definition of cross-correlation coefficient between $\mathbf{h}_{T,1}$ and $\mathbf{h}_{T,2}$ as the inner product of $\mathbf{h}_{T,1}$ and $\mathbf{h}^*_{T,2}$, which is equivalent to $(\mathbf{h}_{T,1} * \mathbf{g}_{T,2})[L-1]$. However, the numerator in (2.3) is the maximal absolute value in the convolved sequence. The operation of finding the maximum is important, in terms of combating any possible synchronization error between two CSI estimations, e.g., the first several taps of CSI may be missed or added in different measurements. Hence, due to its robustness to the synchronization errors in the CSI estimation, the TRRS is capable of capturing all the similarities between multipath CSI samples and increasing the accuracy.

2.2.3.2 Calculating Time-Reversal Resonance Strength with Channel Frequency Response

The CSI obtained from OFDM based WiFi devices is in the frequency domain, i.e., the CSI is in the form of the channel frequency response (CFR). Given the definition of $h(t)$ in (2.1), the CFR becomes

$$h(f) = \sum_{k=1}^{K_{max}} \alpha_k e^{-j2\pi f \tau_k}, \tag{2.5}$$

where f denotes the center frequency of each subcarrier. Given the number of accessible subcarriers to be L, the the CFR can be rewritten as

$$h_F[l] = \sum_{k=1}^{K_{max}} \alpha_k e^{-j2\pi\tau_k \frac{l+1}{NT_s}}, l = 0, 1, \cdots, L-1, \tag{2.6}$$

where the subscript $(\cdot)_F$ denotes the frequency domain CSI, l is the subcarrier index, L is the total number of subcarriers, $T_s = 1/W$ which is defined in (2.2), and N is the size of the DFT as well as the number of samples for each OFDM symbol.

Due to the existence of the carrier frequency offset (CFO), the sampling frequency offset (SFO) and the symbol timing offset (STO), the estimated CFR is corrupted with random phase distortion. Therefore, considering the phase distortion in the CFRs, the calculation of TRRS is defined as follows.

Definition: The TRRS $\mathcal{TR}(\mathbf{h}_{F,1}, \mathbf{h}_{F,2})$ in frequency domain between two CFRs $\mathbf{h}_{F,1}$ and $\mathbf{h}_{F,2}$ is defined as

$$\mathcal{TR}(\mathbf{h}_{F,1}, \mathbf{h}_{F,2}) = \frac{\max\limits_{\phi} \left| \sum\limits_{k} h_{F,1}[k] g_{F,2}[k] e^{jk\phi} \right|^2}{\left(\sum_{l=0}^{L-1} |h_{F,1}[l]|^2 \right) \left(\sum_{l=0}^{L-1} |h_{F,2}[l]|^2 \right)}, \tag{2.7}$$

where $\mathbf{g}_{F,2}$ denotes the TR signature in the frequency domain for CFR $\mathbf{h}_{F,2}$, defined as

$$g_{F,2}[k] = h^*_{F,2}[k], \ k = 0, 1, \cdots, L-1. \tag{2.8}$$

In (2.7), the numerator is similar to the one in (2.3) and the operation of taking maximal value is to addressing the misalignment of random linear phase offset between two CFRs. In the real application, the calculation of numeration is approximated by fast Fourier transform (FFT) with a length of 512 or 1024.

However, given two CFRs that have been individually compensated for the phase distortion, the (2.7) can be rewritten as

$$\begin{aligned} \mathcal{TR}(\mathbf{h}_{F,1}, \mathbf{h}_{F,2}) &= \frac{\left| \sum_k h_{F,1}[k] g_{F,2}[k] \right|^2}{\left(\sum_{l=0}^{L-1} |h_{F,1}[l]|^2 \right) \left(\sum_{l=0}^{L-1} |g_{F,2}[l]|^2 \right)} \\ &= \frac{\left| \sum_k h_{F,1}[k] h^*_{F,2}[k] \right|^2}{\left(\sum_{l=0}^{L-1} |h_{F,1}[l]|^2 \right) \left(\sum_{l=0}^{L-1} |h_{F,2}[l]|^2 \right)} \end{aligned} \tag{2.9}$$

where L is the length of the CFR vector, k is the subcarrier index.

In Chapter 3, we use the definition of TRRS as the one in (2.3) because

the prototype we built probes the multipath channel in time domain. However, in Chapter 4 and Chapter 6 where proposed systems are implemented using commodity WiFi devices, (2.9) and (2.7) are adopted respectively.

2.3 Summary

In this chapter, we introduce the fundamental theory behind radio analytics, including multipath propagation and TR technique. By treating each multipath component as a virtual antenna and leveraging the high degrees-of-freedom in multipath information, radio analytic systems are proposed in this work to interpret an indoor environment and detect indoor events in real time, and even identify the human being present in the environment without the help of cameras. The details of the proposed systems are discussed in the following chapters.

Chapter 3

Indoor Event Detection with Time-Reversal Space

The past few decades have witnessed the increase in the demand of surveillance systems which aims to capture and to identify unauthorized individuals and events. With the development of technologies, traditional outdoor surveillance systems become more compact and of low cost. In order to guarantee the security in offices and residences, indoor monitoring systems are now ubiquitous and their demand is rising both in quality and quantity. For example, they can be designed to guard empty houses and to alarm when break-in happens.

Currently, most indoor monitor systems basically rely on video recording and require cameras deployments in target areas. Techniques in computer vision and image processing are applied on the captured videos to extract information for real time detection and analysis [3–6, 87, 88]. However, conventional vision-based indoor monitor systems have many limitations. They cannot be installed in places requiring high level of privacy like restrooms or fitting rooms. Owing to the prevalence of malicious softwares on the Internet, vision-based indoor surveillance systems may lead to more dangers than protections, contradicting their intention. Moreover, vision-based approaches have a fundamental requirement of a LOS environment with enough illumination is indispensable.

In this chapter, we propose a TR based wireless indoor events detection system, TRIEDS, capable of through-the-wall indoor events detections with only one pair of single-antenna devices. We utilize the TR technique to capture the variations in the multipath CSI due to different indoor events, and propose TRIEDS for indoor event detection. More specifically, thanks to the nature of TR that captures the variations in the CSI, maps different multipath profiles of indoor events into separate points in the TR space, and compresses the complex-valued features into a real-valued scalar called the spatial-temporal resonance strength, the proposed TRIEDS supports simplest detection and classification algorithms with a good performance. Compared with previous works on wireless indoor monitoring systems which require multiple antennas, dedicated sensors, ultra-wideband transmission or LOS environment, and rely on only the amplitude information in the CSI, TRIEDS introduces a novel and practical solution which can well support through-the-wall detection and only requires low-complexity single-antenna hardware operating in the ISM band.

The rest of this chapter is organized as follows. The details of how TRIEDS works are studied and analyzed in Section 3.1, involving an offline training phase and an online testing phase. Moreover, extensive experiments of TRIEDS in detecting indoor events in real office environments are conducted and the experimental results are investigated in Section 3.2. Based on the results in Section 3.2, we further discuss how the system parameters, human motions will affect the accuracy of TRIEDS. Finally, conclusions are drawn in Section 3.4.

3.1 Proposed Algorithms

In this part, we present a detailed introduction to the proposed TR based indoor events detection system, TRIEDS. The proposed TRIEDS exploits the intrinsic property of TR technique that the spatial-temporal resonance fuses and compresses the information of the multipath propagation environment. To implement the indoor events detection based on the TR spatial-temporal resonances, TRIEDS consists of two phases: the offline training and the online testing. During the first phase, a training database is built by collecting the signature $\mathbf{g}$ of each indoor events through the TR channel probing phase. After training, in the second phase, TRIEDS estimates the instantaneous multipath CSI $\mathbf{h}$ for current state and makes the prediction according to the signatures in the offline training database by means of the strength of the generated spatial-temporal resonance. The detailed operations are discussed in the followings.

3.1.1 Phase 1: Offline Training

As discussed above, TRIEDS leverages the unique indoor multipath profile and TR technique to distinguish and detect indoor events. During the offline training phase, we are going to build a database where the multipath profiles of any targets are collected and stored the corresponding TR signatures in the TR space. Unfortunately, due to noise and channel fading, the CSI from a specific state may slightly change over the time. To combat this kind of variations, for each state, we collect several instantaneous CSI samples to build the training set.

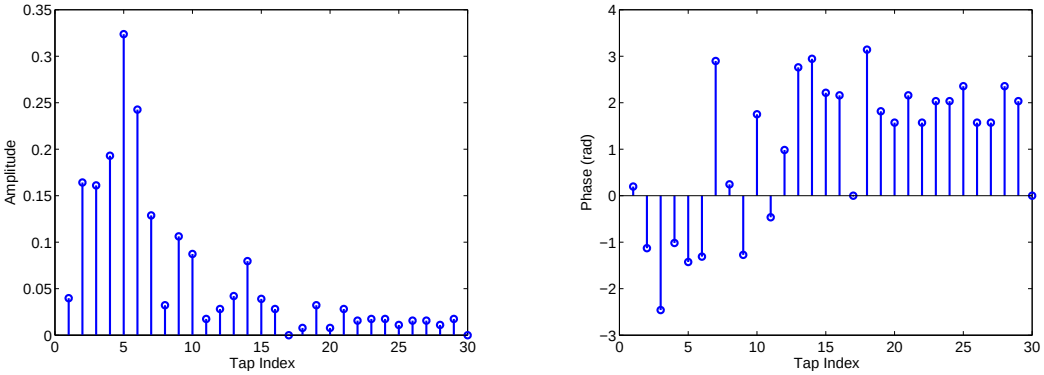

(a) The amplitude. (b) The phase.

Figure 3.1: An example of indoor CSI.

Specifically, for each indoor state $S_i \in \mathcal{D}$ with $\mathcal{D}$ being the state set, the corresponding training CSI, a.k.a. CIR, is estimated and form a matrix $\mathbf{H}_{T,i}$ as,

$$\mathbf{H}_{T,i} = [\mathbf{h}_{T,i,t_0},\ \mathbf{h}_{T,i,t_1},\ \cdots,\ \mathbf{h}_{T,i,t_{N-1}}], \tag{3.1}$$

where N is the size of the CSI samples for a training state. $\mathbf{h}_{T,i,t_j}$ represents the estimated CSI vector of state S_i at time t_j and $\mathbf{H}_{T,i}$ is named as the CSI matrix for state S_i. An example of estimated indoor CSI obtained by the prototype in Figure 3.2 shown in Figure 3.1, where the total length of the CSI is 30. From Figure 3.1(a), we can find out that there exist at least 10 to 15 significant multipath components.

The corresponding TR signature matrix $\mathbf{G}_i$ can be obtained by time-reversing the conjugated version of $\mathbf{H}_{T,i}$ as:

$$\mathbf{G}_i = [\mathbf{g}_{T,i,t_0},\ \mathbf{g}_{T,i,t_1},\ \cdots,\ \mathbf{g}_{T,i,t_{N-1}}], \tag{3.2}$$

where the TR signature is defined in (2.4). Here, the superscript $*$ on a vector variable represents the conjugate operator. L denotes the length of a CSI vectors

and k denotes the index of taps. Then the training database $\mathcal{G}$ is the collection of $\mathbf{G}_i$'s.

3.1.2 Phase 2: Online Testing

After constructing the training database $\mathcal{G}$, TRIEDS is ready for real-time indoor events detection. The indoor events detection is indeed a classification problem. Our objective is to detect the state of indoor targets through evaluating the similarity between the testing TR signatures and the TR signatures in the training database $\mathcal{G}$. The raw CSI information is complex-valued and of high dimensions, which complicates the detection problem and increases the computational complexity if we directly treat the CSI as the feature. To tackle this problem, by leveraging the TR technique, we are able to naturally compress the dimensions of the CSI vectors through mapping them into the strength of the spatial-temporal resonances.

When comparing two estimated multipath profiles, they are first mapped into the TR space where each of them is represented as one TR signature. Then the TRRS as defined in (2.3) is a metric that quantifies the similarity between these two multipath profiles in the mapped TR space. The higher the TRRS is, the more similar two multipath profiles are in the TR space.

During the online monitoring phase, the receiver keeps matching the current estimated CSI to the TR signatures in $\mathcal{G}$ to find the one that yields the strongest TR spatial-temporal resonance. The TRRS between the unknown testing CSI $\tilde{\mathbf{H}}_T$

and state S_i is defined as

$$\mathcal{TR}_{S_i}(\tilde{\mathbf{H}}_T) = \max_{\tilde{\mathbf{h}}_T \in \tilde{\mathbf{H}}_T} \max_{\mathbf{h}_{T,i} \in \mathbf{H}_{T,i}} \mathcal{TR}(\tilde{\mathbf{h}}_T, \mathbf{h}_{T,i}), \tag{3.3}$$

where $\tilde{\mathbf{H}}_T$ is a group of CSI samples assumed to be drawn from the same state as

$$\tilde{\mathbf{H}}_T = [\tilde{\mathbf{h}}_{T,t_0},\ \tilde{\mathbf{h}}_{T,t_1},\ \cdots,\ \tilde{\mathbf{h}}_{T,t_{M-1}}], \tag{3.4}$$

and M is the number of CSI samples in one testing group, similar to the N in the training phase defined in (3.1).

Once we obtain the TRRS for each event, the most possible state for the testing CSI matrix $\tilde{\mathbf{H}}_T$ can be found by searching for the maximum among $\mathcal{TR}_{S_i}(\tilde{\mathbf{H}}_T),\ \forall\, i$, as

$$S^* = \arg\max_{S_i \in \mathcal{D}} \mathcal{TR}_{S_i}(\tilde{\mathbf{H}}_T), \tag{3.5}$$

The superscript $*$ on S denotes the optimal.

Besides finding the most possible state S^* by comparing the TR spatial-temporal resonances, TRIEDS adopts a threshold-trigger mechanism, in order to avoid false alarms introduced by events outside of the state class $\mathcal{D}$. TRIEDS reports a change of states to S^* only if the TRRS $\mathcal{TR}_{S^*}(\tilde{\mathbf{H}}_T)$ reaches a predefined threshold γ.

$$\hat{S} = \begin{cases} S^*, & \text{if } \mathcal{TR}_{S^*}(\tilde{\mathbf{H}}_T) \geq \gamma, \\ 0, & otherwise, \end{cases} \tag{3.6}$$

where $\hat{S} = 0$ means the state of current environment is not changed, i.e., TRIEDS is not triggered for any trained states in $\mathcal{D}$. According to the aforementioned detection rule, a false alarm for state S_i happens whenever a CSI is detected as $\hat{S} = S_i$ but it is not from state S_i.

Figure 3.2: Prototype of TRIEDS.

Although the algorithm for TRIEDS is simple, the accuracy of indoor events detection is high and its performance is validated through multiple experiments in the next section.

3.2 Experimental Results

To empirically evaluate the performance of TRIEDS, we conduct several experiments for door states detection in a commercial office environment with different transmitter-receiver locations, using the prototype in Figure 3.2. The prototype operates at 5.4 GHz band with a bandwidth of 125 MHz

To begin with, a simple LOS experiment for validating the feasibility of TRIEDS is conducted in a controlled environment, with 7 transmitter locations, one receiver location and two events. Then, the validation is further extended to both LOS and NLOS cases in a controlled office environment with 3 receiver locations, 15 locations for transmitter and 8 targeted doors made of wood. Meanwhile, experiments

are conducted in an uncontrolled indoor environment during normal working hours with people around. Furthermore, the performance of the proposed TRIEDS is also compared with that of the RSS-based indoor monitoring approach, which can be easily extracted from the channel information and classified the using kNN method. To further evaluate the accuracy of the proposed TRIEDS in real environments, the performance of TRIEDS with intentional human movements is studied. Last but not least, results of TRIEDS being as a guard system to secure a closed room are discussed.

3.2.1 Experimental Setting

The prototype of the proposed TRIEDS requires one pair of single-antenna transmitter and receiver that work on the ISM band with the carrier frequency being 5.4 GHz and a 125 MHz bandwidth. Moreover, during the experiment, the system runs with a channel probing interval around 20 millisecond (ms). A snapshot of the hardware device for TRIEDS is shown in Figure 3.2 with the antenna installed on the top of the radio box.

The experiments are carried out in the offices at the 10^{th} floor in a commercial building of 16 floors in total. The experimental offices are surrounded by multiple offices and elevators. The detailed setup is shown in the floorplans in Figure 3.3. During the experiments, we are detecting the open/closed states of multiple wooden doors labeled as D1 to D8. The TX-RX locations include both LOS and NLOS transmissions.

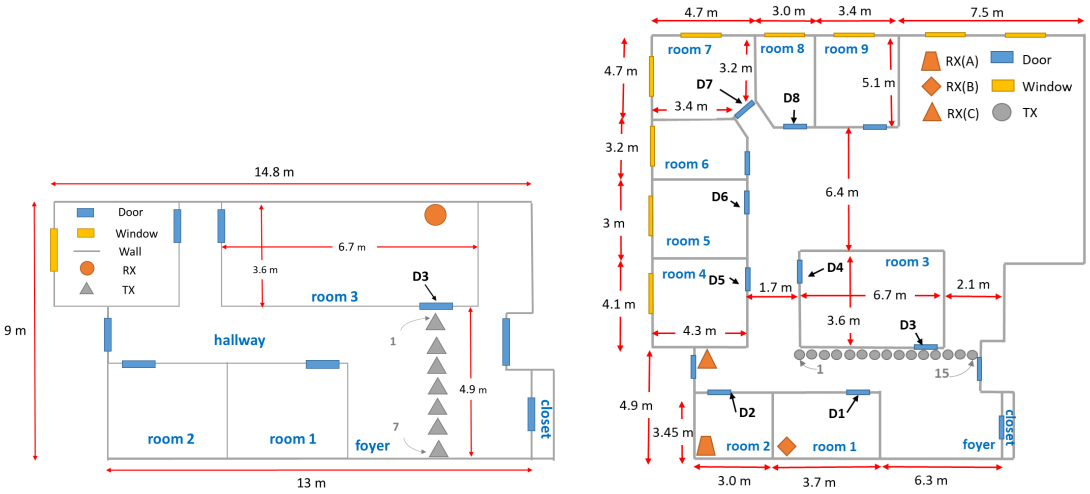

(a) Setting 1. (b) Setting 2.

Figure 3.3: Experimental setting for TRIEDS: floorplans

In TRIEDS experiments, the receiver and the transmitter are placed on the top of stands at the intended locations, with the height from the ground being 4.3 ft and 3.6 ft respectively, as shown in Figure 3.4(a) and Figure 3.4(b).

In all the experiments, we choose the number of the training CSI and the testing CSI to be $N = 10$ and $M = 10$ as defined in (3.1) and (3.4).

3.2.2 Feasibility Validation

To begin with, the feasibility for the proposed TRIEDS to detect indoor events is verified in a LOS case where the receiver is placed inside room 3 as shown in Figure 3.3(a), and the transmitter is moving along the 7 locations marked by "△" in a vertical line with the dot nearest to the targeted door being labeled as index "1". Our task is to detect whether the wooden door D3 is closed or open.

The multipath CSI samples for D3 open and closed are obtained through

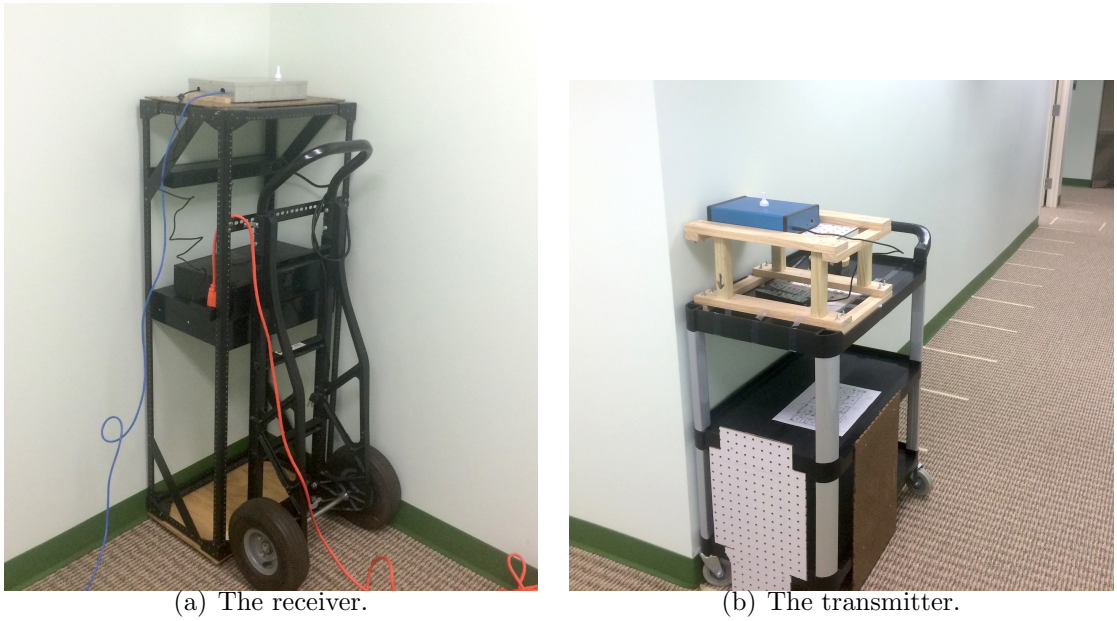

(a) The receiver. (b) The transmitter.

Figure 3.4: Experimental setting for TRIEDS: devices.

Location Index	1	2	3	4	5	6	7
False Alarm Rate (%)	0	0	0	0	0	0	0
Detection Rate (%)	100	100	100	100	100	100	100

Table 3.1: Performance of the proposed TRIEDS in easy case.

TR channel probing phase and the corresponding TR signatures are stored in the database. In the testing phase, we keep listening to the multipath channel and matching the collected testing CSI to the database for. With any threshold γ smaller than 0.97, we can achieve the perfect detection for all the 7 transmitter locations as in Table 3.1.

In this case, the proposed TRIEDS indeed performs a detection for the events on the LOS path between the transmitter and the receiver. Through this simple

experiment, we have demonstrated the feasibility of TRIEDS to use the TR spatial-temporal resonance to capture the changes in the indoor multipath environment. Next, the performance of TRIEDS is further evaluated under more complicated changes of the multipath environment and with both LOS and NLOS TX-RX transmissions.

3.2.3 Single Door Monitoring

In this part, the experiments are conducted to understand how locations of the receiver, the transmitter and the targeted objects affect the performance of TRIEDS. The receiver is placed at location "RX(A)", "RX(B)" and "RX(C)", whereas the transmitter is moving along 15 locations separated by 0.5 meters in a horizontal line as marked by grey dots in Figure 3.3(b). The objective of TRIEDS is to monitor the states of wooden door D1. During the experiment, for each location and each indoor event, we measure 3000 samples of the CSI which takes about 5 minutes by using our built prototype, leading to a total experimental time to be 10 minutes for each TX-RX location.

Here, the location "RX(A)" (LOC A) represent a throuth-the-wall detection scenario in the absence of a LOS path between the transmitter and the receiver, and between the receiver and where the indoor event happens. Under the case when the receiver is at the location "RX(B)" (LOC B), there is always a LOS path between the receiver and where the indoor event happens, since they are in the same room. However, the LOS path between the transmitter and the receiver disappears

regarding most of the possible transmitter locations, and it exists only if the transmitter, the receiver and the door D1 form a line. However, the transmitter and the receiver always perform LOS transmission when the receiver is at the location "RX(C)" (LOC C). Meanwhile, the door D1 to be detected falls outside of the LOS link between the transmitter and the receiver.

3.2.3.1 LOC A: NLOS case

As we discussed above, when the receiver is on LOC A in room 2, there is no LOS path between the receiver and the transmitter, and the receiver and door D1 are isolated by walls. One example of the multipath CSI for the open and the closed state of door D1 is shown in Figure 3.5. In Figure 3.5 where only the amplitudes of the CSI are plotted, it is clear to observe a change in how the energy is distributed on each tap. In the proposed TRIEDS, not only the amplitude information but also the phase for each tap is taken into consideration by means of the TR spatial-temporal resonance.

From the experiment, with a threshold γ no larger than 0.9, we can achieve a perfect detection rate and zero false alarm rate for all 15 transmitter locations. Hence, we can conclude that TRIEDS is capable of detecting an event in a NLOS environment with through-the-wall detection and the distance between the receiver and the transmitter has little effect on the performance.

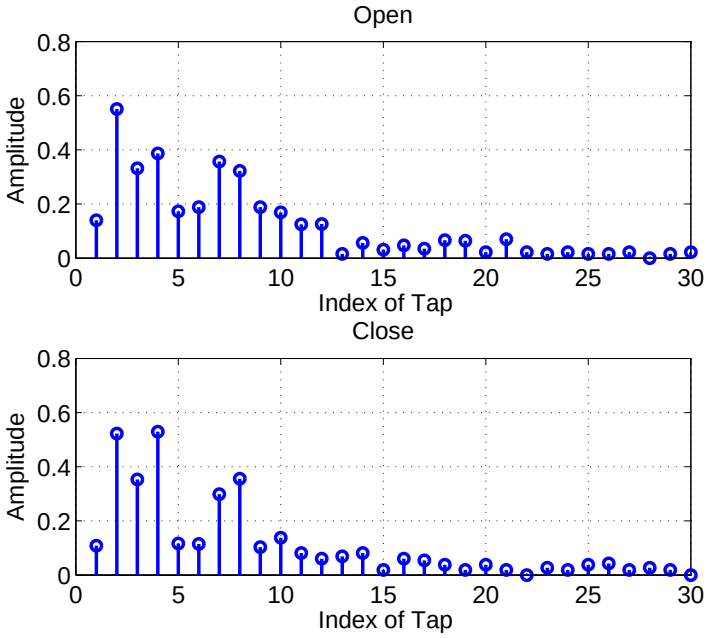

Figure 3.5: Multipath profiles (amplitude part) of door D1 under LOC A.

3.2.3.2 LOC B: LOS and NLOS case

When the receiver is on LOC B in room 1, as the transmitter moving from the location "1" to the location "4" (the 4^{th} dot right to the one marked as "1"), the transmission scenario between the transmitter and the receiver is NLOS due to the absence of a direct LOS link. Then, the trasmission scenario become LOS, when the transmitter is on the location "5" to the location "6". When the transmitter moves farther away (i.e., from the dot "7"), there is no LOS path again between the transmitter and the receiver and the transmission scenario becomes NLOS. In Figure 3.6(a) and Figure 3.6(b), examples of the CSI for each event are plotted to demonstrate the changes in the amplitudes of the multipath profile corresponding to the indoor event.

Considering the accuracy for TRIEDS, with a threshold $\gamma \leq 0.9$, the detection

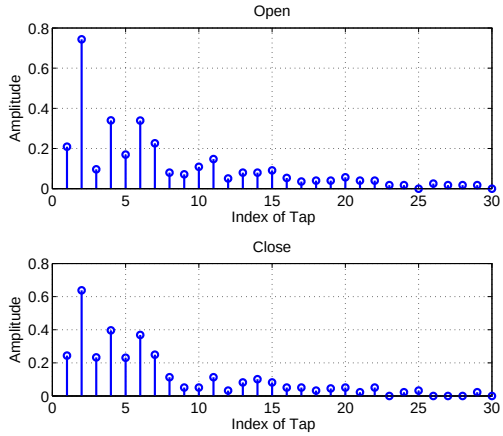

(a) A multipath profile (amplitude part) when TX on location "1" (NLOS).

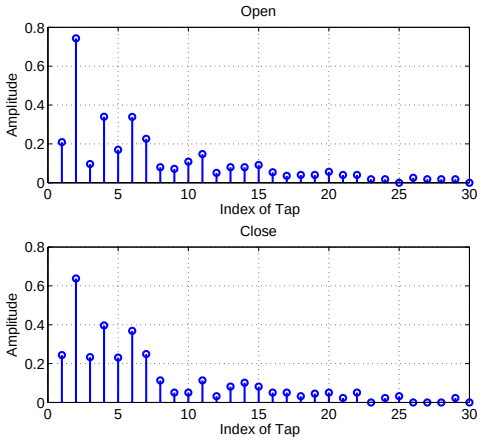

(b) A multipath profile (amplitude part) when TX on location "5" (LOS).

Figure 3.6: Multipath profiles of door D1 for LOC B under NLOS and LOS scenarios.

rate for all 15 transmitter locations is higher than 99.9%. Except when the transmitter is at the location "6", the detection probability drops to 95.9%. Nevertheless, the corresponding false alarm rates are all below 0.1%. Since the experiment is carried out in a commercial office building, there exist outside activities that we cannot control but indeed change the multipath CSI to fall out the collected indoor events. So the reason for the detection probability at the 6^{th} location being 95.9% might be the existence of uncontrollable outside activities. For example, the elevator running which may greatly change the outside multipath propagation because it is close to the environmental office and is made of metal. Moreover, generally, TRIEDS is robust to the various distances between the transmitter, the receiver and where the indoor event happens.

3.2.3.3 LOC C: LOS case

When the receiver is on LOC C outside room 2, no matter where the transmitter is, they are transmitting under LOS scenario, which leads to a dominant multipath component exists in the multipath CSI.

The LOS transmission brings difficulties to indoor events detection when event locates outside of the LOS path between the transmitter and the receiver. The reason for that can be decomposed into two parts. In the first place, in this experiment, the object door D1 is located parallel with the transmission link between the transmitter and the receiver, and has little influence to the dominant LOS component in the multipath profile. Secondly, since more energy is focused on the LOS path dominant in the CSI, the other multipath components that contain the event information are more noise-like and less informative. Hence, as most of the information for the event is buried in the CSI components with only a few energy, it is hard to detect an event happening outside the direct link between the transmitter and the receiver in a LOS-dominant wireless system. This can be shown by an example of the multipath CSI with respect to the open and closed states of door D1 in Figure 3.7, where the dominant path remains the same and contains most of the energy in the CSI.

In the experiment, TRIEDS yields a 100% detection rate and a 0 false alarm rate for all the 15 transmitter locations with the threshold $\gamma \leq 0.93$. The experimental result supports our claim that the proposed TRIEDS can capture even minor changes in the multipath profile by using TR technique.

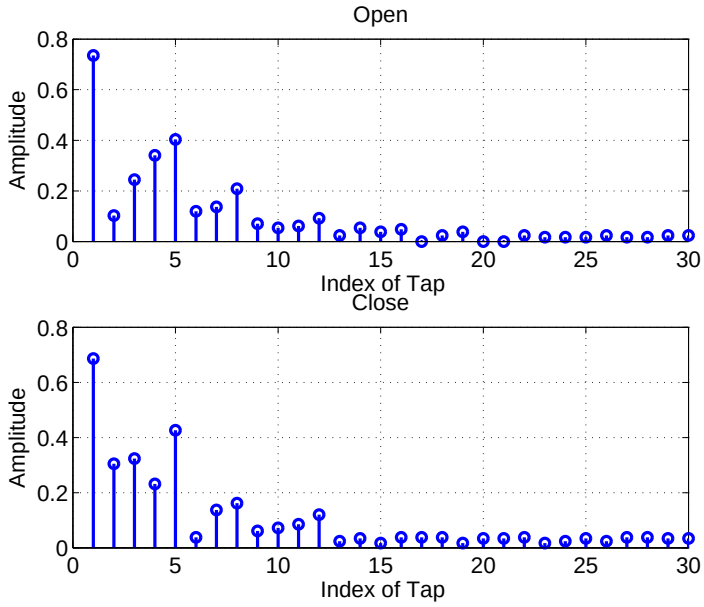

Figure 3.7: Multipath profiles (amplitude part) of door D1 under LOC C.

3.2.4 TRIEDS in Controlled Environments

In the previous sections, we have validated the capability of the proposed system of detecting two indoor events with both LOS and NLOS transmission in controlled indoor environments. In this part, we are going to study the performance of TRIEDS in detecting multiple indoor events. Moreover, the performance comparison between the RSSI-based indoor detecting approach and the proposed TRIEDS is further investigated.

In the experiment, the receiver is placed on either LOC B in room 1 or LOC C outside room 2, whereas the transmitter moves and stops on every two grey dots that are separated by 1 meter, named from "axis 1" to "axis 4" respectively. In total, we have 2 receiver locations and 4 transmitter locations, i.e., 8 TX-RX locations. The objective of TRIEDS is to detect which wooden doors among D1 to D8 is closed

State Index	Description
S_1	All the doors are open.
S_{i+1}	Door Di closed and the others open, $\forall i = 1, 2, \cdots, 8$.

Table 3.2: State list for TRIEDS to detect.

versus all other doors are open, as labeled in Figure 3.3(b). During the experiment, for each TX-RX location and each event, we measure 3000 CSI samples which takes approximately 5 minutes, leading to a total monitoring time of 45 minutes. In Table 3.2 is the state table describing all the indoor events in the experiment.

As we claimed and verified in the single-event detection experiment that the proposed TRIEDS can achieve highly accurate detection performance by utilizing the spatial-temporal resonance to capture changes in the multipath profiles. In this section, we evaluate the capability of TRIEDS of detecting multiple events in a controlled indoor environment. The performance analysis for normal office environment during working hours will be discussed later.

3.2.4.1 Evaluations on LOC B

To begin with, the performance of TRIEDS when the receiver is on LOC B is studied. In Figure 3.8, we show how the TRRS varies between different events.

Due to the fact that door D5 and D6 are closed to each other whereas they are far away to the receiver and the transmitter, the introduced changes in the multipath profiles of both of them are similar. Consequently, the resonance strength between

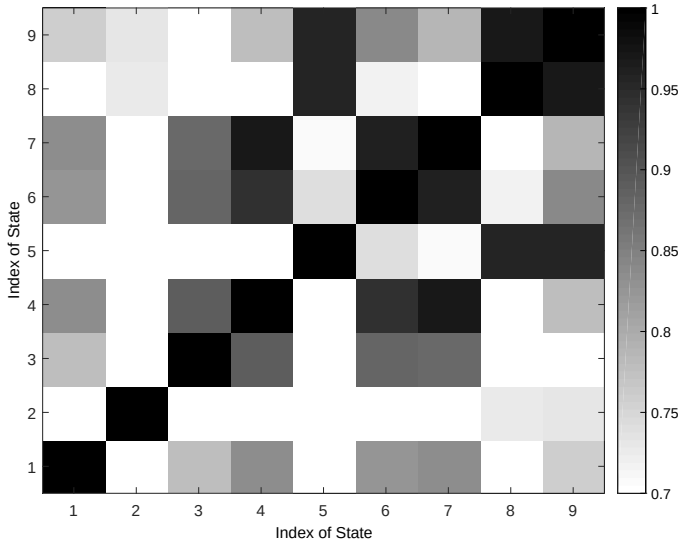

Figure 3.8: Resonance strength map with RX on LOC B and TX on the 1^{st} green dot (axis 1).

states S_6 and S_7 is relatively higher than other off-diagonal elements, but it is still smaller than the diagonal ones in Figure 3.8 that represent the in-class resonance strength. Similar phenomenon happens between states S_8 and S_9.

In Figure 3.9 and Figure 3.10, examples of the receiver operating characteristic (ROC) curves for detecting states of indoor doors are plotted for both the proposed TRIEDS system and the conventional RSSI approach. Here, the legend "aixs i", $i = 1, 2, 3, 4$, denotes the location of transmitter to be on the $(2 * i - 1)^{th}$ grey dot in Figure 3.3(a).

As shown by Figure 3.9 and Figure 3.10, the proposed TRIEDS outperforms the RSSI-based approach in distinguishing between one door is closed (i.e., $S_i,\ i \geq 1$) versus all doors are open (i.e., S_0), by achieving perfect detection and zero false alarm rate. Note that S_9 is the state of door D8 which is blocked from the TX-RX link by

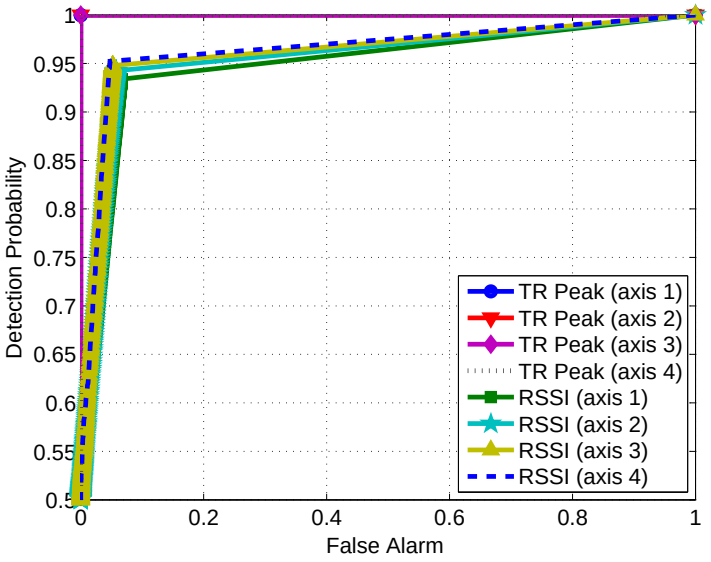

Figure 3.9: ROC curve for distinguishing between S_1 and S_2 under LOC B.

a closed office, as an example, Figure 3.9 demonstrates the superiority of TRIEDS in performing a through-the-wall detection. Meanwhile, the performance of the RSSI-based approach degrades as the distance between where the indoor event happens and the TX-RX gets smaller. By leveraging the TR technique, TRIEDS is capable of capturing the changes in a multipath environment in a form of multi-dimensional and complex-valued vector with high degree of freedoms, and of distinguishing between different changes in the TR spatial-temporal resonance domain. However, the RSSI based approach tries to monitor the changes in the environment through a real-valued scalar, which due to its dimension loses most of the distinctive information.

Furthermore, the accuracy of detection of TRIEDS improves as the distance between the transmitter and the receiver increases. So does the RSSI-based method. The reason is that when the transmitter and the receiver get far away, more energy will be distributed to the multipath components with longer distance and thus the

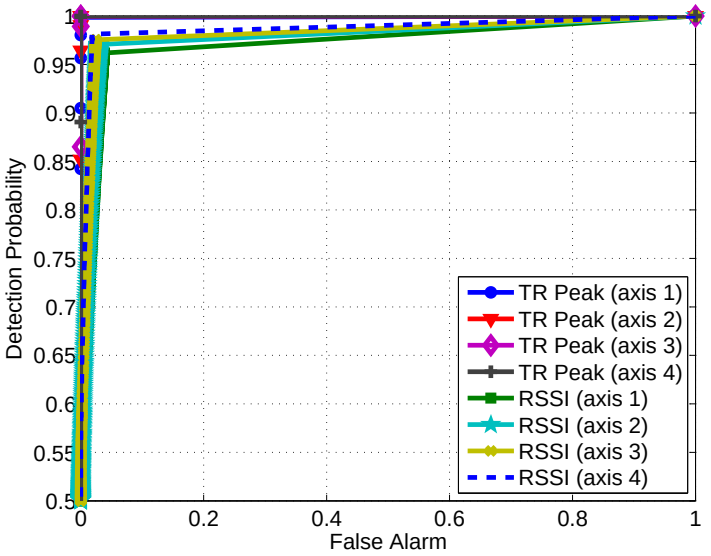

Figure 3.10: ROC curve for distinguishing between S_1 and S_9 under LOC B.

sensing system will have a larger converage. The overall performance obtained by averaged on all possible events shows that TRIEDS outperforms the RSSI approach in Table 3.3.

3.2.4.2 Evaluations on LOC C

Experiments are further conducted to evaluate the performance of indoor multiple events detection in a LOS transmission scenario by putting the receiver on LOC C. In Figure 3.11, we show the strengths of the TR spatial-temporal resonances between different indoor events. When the receiver and the transmitter transmit in a LOS setting, the CSI is LOS-dominant such that the energy of the multipath profile is concentrated only on a few taps. It makes the coverage of TRIEDS shrink and degrades the performance of TRIEDS, especially when the indoor events happen far from the TX-RX link as shown in Figure 3.11.

LOC B	axis 1	axis 2	axis 3	axis 4
Detection Rate TRIEDS (%)	99.12	99.5	99.67	99.81
False Alarm TRIEDS (%)	0.88	0.5	0.33	0.19
Detection Rate RSSI (%)	89.41	91.16	92.07	93.07
False Alarm RSSI (%)	10.59	8.84	7.93	6.93

Table 3.3: False alarm and detection probability for multi-event detection on LOC B in controlled environment.

Examples of ROC curves to illustrate the detection performance of both TRIED-S and the RSSI-based approach are plotted in Figure 3.12 and Figure 3.13. The performance of the proposed TRIEDS working in a LOS environment is similar to that in a NLOS environment. Generally, TRIEDS achieves a better accuracy for events detection with a lower false alarm rate, compared with the RSSI-based approach. In both scenarios, TRIEDS achieves almost perfect detection performance in differentiating between $S_i, i \geq 1$ and S_0. Moreover, the RSSI method has a better accuracy in the LOS case than that in the NLOS case.

The corresponding overall performance comparison for TRIEDS and the RSSI-based method is shown in Table 3.4. It is obvious that the farther the receiver and the transmitter are separated, the better accuracy TRIEDS achieves. Moreover, compared with Table 3.3, the accuracy of RSSI-based method improves a lot in LOS environment, whereas the one of TRIEDS degrades slightly. Moreover, comparing

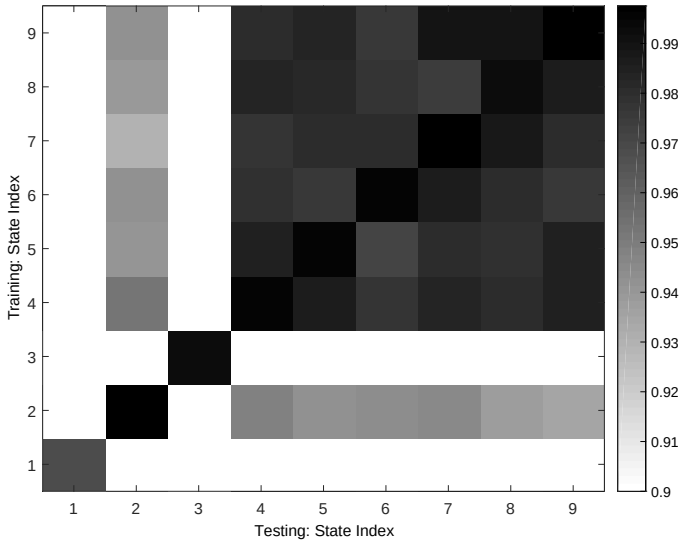

Figure 3.11: Resonance strength map with RX on LOC C and TX on the 1^{st} green dot (axis 1).

the results in Table 3.3 and Table 3.4, the detection performance for TRIEDS degrades a little when the receiver and the transmitter change the transmission scheme from NLOS to LOS. Because of the dominant LOS path in LOS transmission, the ability to perceive multipath components which is far away from the direct link degrades, leading to a worse detection accuracy.

3.2.5 TRIEDS in Normal Office Environments

In this part, we repeat the experiments in the previous section during working hours in weekdays, where approximately 10 individuals are working in the experiment area, and all offices surrounding and locating beneath or above the experimental area are occupied with uncontrollable individuals.

The proposed TRIEDS achieves similar accuracy compared with that of the

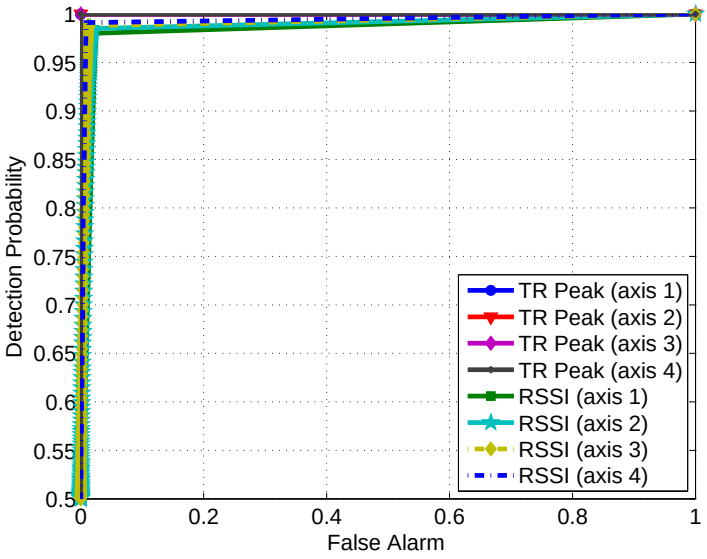

Figure 3.12: ROC curve for distinguishing between S_1 and S_2 under LOC C.

controlled experiment. The overall false alarm and the detection rate for TRIEDS and the RSSI-based approach are shown in the Table 3.5 and Table 3.6.

The results in Table 3.5 and Table 3.6 are consistent with the results in Table 3.3 and Table 3.4. The performance for TRIEDS is superior to that of the RSSI-based approach, by realizing a better detection rate and a lower false alarm rate. Even in the dynamic environment, the proposed TRIEDS can maintain a detection rate higher than 96.92% and a false alarm smaller than 3.08% under the NLOS case, whereas a detection rate higher than 97.89% and a false alarm smaller than 2.11% under the LOS case. Moreover, as the distance between the receiver and the transmitter increases, the accuracy of both methods improves. In the comparison of Table 3.3, 3.4, 3.5 and 3.6, we claim that the proposed TRIEDS has a better tolerance to the environment dynamics.

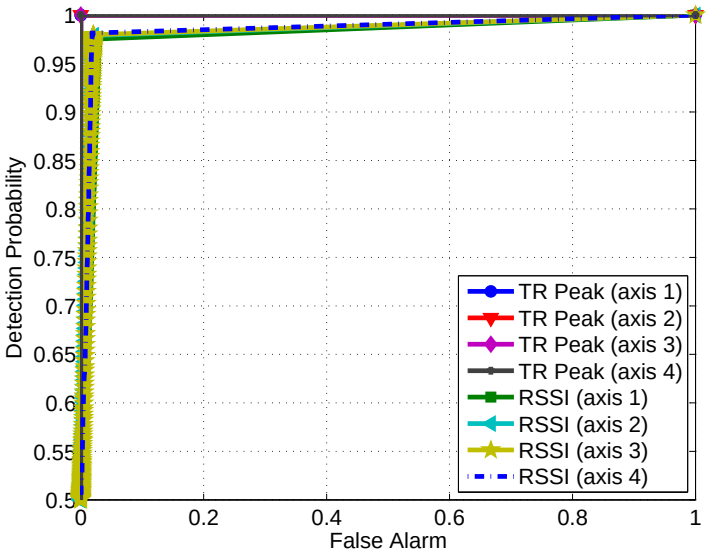

Figure 3.13: ROC curve for distinguishing between S_1 and S_9 under LOC C.

3.2.6 TRIEDS with Intentional Human Movements

To investigate on the effects that the human movements have on the performance of TRIEDS, we conduct experiments with none, one and two individuals keep moving back and forth in the shaded area as Figure 3.14 shows. Meanwhile, the transmitter and the receiver are placed to detect the states of two adjacent doors labeled as "D1" and "D2". The list of door states is in Table 3.7. For each set of experiments, TRIEDS detects the states of the two doors for 5 minutes during the normal working hours.

Interference caused by the human movements changes the multipath propagation environment and brings in the variations in the TR spatial-temporal resonances during the monitoring process of TRIEDS. Fortunately, due to the mobility of human, the introduced interference keeps change and the duration for each interference

LOC C	axis 1	axis 2	axis 3	axis 4
Detection Rate TRIEDS (%)	99.09	99.28	99.31	99.35
False Alarm TRIEDS (%)	0.91	0.72	0.69	0.65
Detection Rate RSSI (%)	97.24	97.66	97.8	97.88
False Alarm RSSI (%)	2.76	2.34	2.2	2.12

Table 3.4: False alarm and detection probability for multi-event detection on LOC C in controlled environment.

LOC B	axis 1	axis 2	axis 3	axis 4
Detection Rate TRIEDS (%)	96.92	98.95	99.23	99.4
False Alarm TRIEDS (%)	3.08	1.05	0.77	0.6
Detection Rate RSSI (%)	92.5	94.16	94.77	95.36
False Alarm RSSI (%)	7.5	5.84	5.23	4.64

Table 3.5: False alarm and detection probability for multi-event detection on LOC B in normal environment.

is short. To combat the resulted bursted variations in the TRRSs, we adopt the majority vote method combined with a sliding window to smooth the detection results over time. Supposing we have the previous $K-1$ outputs $S_k^*,\ k = t-K+1,\ \cdots, t-1$ and the current result S_t^*, then the decision for time stamp t is made by majority vote over all $S_k^*,\ k = t-K+1,\ \cdots, t$, so on and so forth for all t. K denotes the

LOC C	axis 1	axis 2	axis 3	axis 4
Detection Rate TRIEDS (%)	97.89	98.94	99.18	99.36
False Alarm TRIEDS (%)	2.11	1.06	0.82	0.64
Detection Rate RSSI (%)	96.73	97.19	97.35	97.43
False Alarm RSSI (%)	3.27	2.81	2.65	2.57

Table 3.6: False alarm and detection probability for multi-event detection on LOC C in normal environment.

State	00	01	10	11
D1	Open	Open	Closed	Close
D2	Open	Closed	Open	Closed

Table 3.7: State list for study on human movements.

size of the sliding window for smoothing.

In Table 3.8, we compare the average accuracy over all states for TRIEDS with or without the smoothing algorithm in the absence of human movements (HM), and in the presence of the intentional persistent human movements performed by one individual and two individuals. Here, the length of the sliding window is $K = 20$. First of all, the accuracy of TRIEDS reduces as the number of individuals increases, performing persistent movements near the location of the indoor events to be detected, the transmitter and the receiver. Moreover, the adopted smoothing

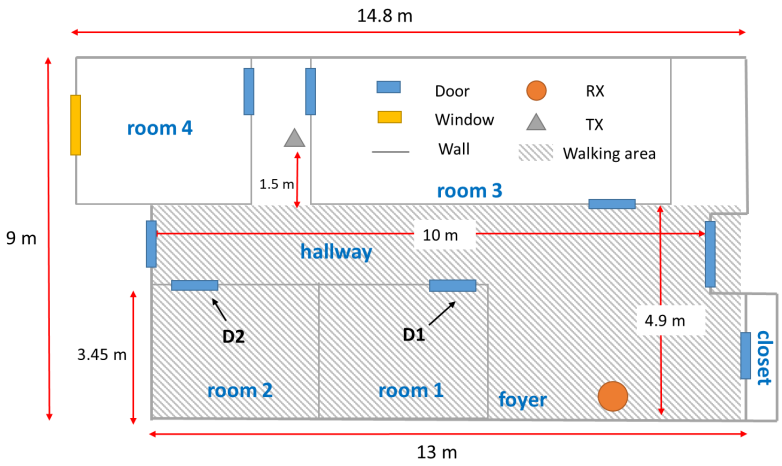

Figure 3.14: Experiment setting for study on human movements.

Experiment	No HM	One HM	Two HM
No Smoothing	97.75%	87.25%	79.58 %
With Smoothing	98.07%	94.37%	88.33 %

Table 3.8: Accuracy comparison of TRIEDS under human movements.

algorithm improves the robustness of TRIEDS to human movements and enhances the accuracy by 7% to 9% compared with that of the case without smoothing. Meanwhile, during the experiments, we also find that the most vulnerable state is state "00" where all doors are open, such that with human movements TRIEDS is more likely to yield a false alarm than other states. The reason is that as human moves close to the door location, the human body, viewed as an obstacle at the door location, is similar to a closed wooden door, and hence the changes in the multipath CSI are also similar, especially for D1.

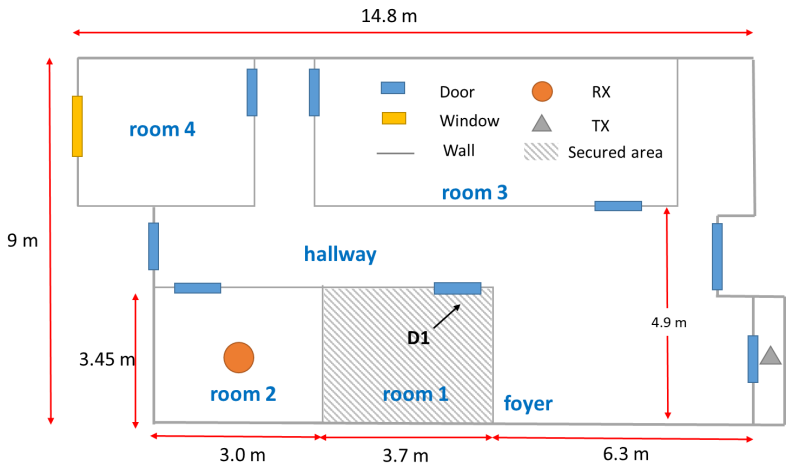

Figure 3.15: Experiment setting for guard test.

3.2.7 For through-the-wall Guard

Unlike the previous experiments where we are trying to detect the door states, in this part, TRIBOD is functioning as a through-the-wall guard system. The objective for TRIEDS is to secure a target room through walls and to alarm not only when the door state changes but also when unexpected human movements happen inside the secured room. The system setup is shown in Figure 3.15, where the secured room is shaded.

In this experiment, the transmitter and the receiver of TRIEDS, marked as purple and green dots, are placed in two rooms respectively as shown in Figure 3.15. TRIEDS is aimed to monitor and secure the room in the middle, and to report as soon as the door of the secured room is open or someone is walking inside the secured room. TRIEDS only collects the training data for normal state, i.e., door is closed and no one is walking inside the room. The training database consists of 10 samples of the CSI. Once TRIEDS starts monitoring, it will keep sensing the indoor

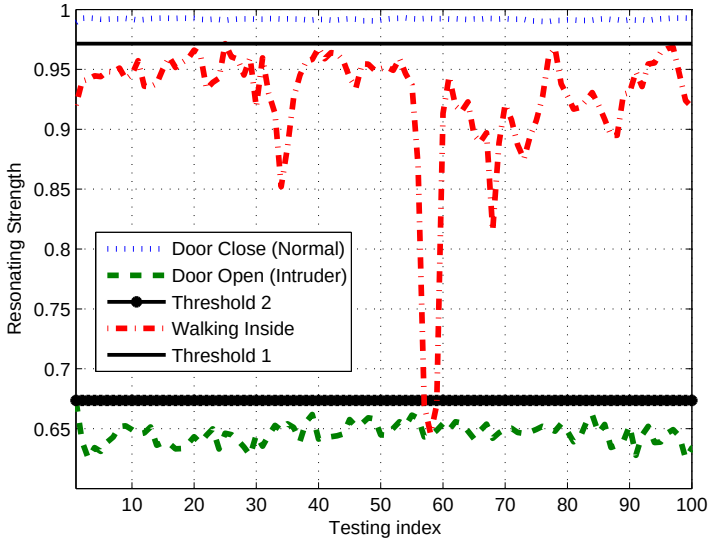

Figure 3.16: Resonating strength of guard system.

multipath channel profile, and compare it with the training database by computing the time reversal resonance strength according to (2.3) and (3.3).

An example is shown in Figure 3.16, where we can see a clear cut between the normal state and the intruder state, and between the normal state and the state where someone is walking inside the room. The *threshold 1* is the threshold for detecting when the indoor states deviates from the normal state, leading to a 100% detection rate and 0 false alarm. Whereas the *threshold 2* is for differentiating between the intruder state(i.e., door is open) and the state when someone is walking inside the secured room with the door is closed, based on which TRIEDS only has 3% error by classifying the human activity state as the intruder state. Even with a single-class training dataset, TRIEDS is capable of distinguishing between different events and functioning as an alarm system to secure the rooms through the walls.

3.3 Discussion

3.3.1 Impact of System Parameters

1. *Sampling Frequency:* In this work, the sampling frequency of TRIEDS is 50 Hz, i.e., TRIEDS senses the multipath environment every 20 ms. Since usually the changes of door states happen in 1 to 2 seconds (s), current sampling frequency is enough for capturing binary changes for doors. In order to detect and monitor the entire transition of the changes or other changes happen in a sudden, a higher sampling frequency is indispensable.

2. *Size of Training and Testing Group:* In the current experiments, we choose both the training group size M in (3.1) and the testing group size N in (3.4) as 10, to address the variations of noise in the CSI estimation. We have studied the performance of TRIEDS with different sizes of training and testing group. It is found out that with a size greater than 10, the performance does not improve much but a larger delay for acquiring more CSI samples is introduced. Hence, in this work, without sacrificing the time sensitivity of TRIEDS, the size of 10 (i.e., a sensing duration of 0.2s) is adopted.

3.3.2 Impact of Human Motion Interference

TRIEDS utilizes the TR technique to map multipath profiles of indoor events into separate points in the TR space, due to the fact that different indoor events and human movements alter the wireless multipath profiles differently.

In Section IV-G, the experimental results of applying TRIEDS in a through-the-wall guard task are discussed. As shown in the Figure 3.16, in most cases, given the door close event with no human motions, the TRRS of the same event with human motions drops. However, the degradation in the TRRS introduced by human motions is small, whereas the gap between the TRRS of the door close event and that of the door open event is significantly large. The reason is that due to the small size of human body compared to indoor objects like doors, human body only alters a small portion of multipath components when moving not close to the transmitter or the receiver, resulting in sparse changes in the amplitude or the phase of a couple of taps in the CSI. Consequently, the point of door close event with human motions locates at the "proximity" of the point of the static door close event, i.e., the two points are quite similar measured by the TRRS. They can be viewed as a single cluster given a proper threshold on the TRRS. However, when the human motions are close to the transmitter or the receiver, there is a chance that the altered multipath profile differs a lot from the one of the static indoor event, leading to a great attenuation in the TRRS, and thus a different cluster in the TR space as well as a miss detection in TRIEDS. Moreover, as discussed in Section IV-F, the detection accuracy drops compared to the case without intentional motions with intentional human movements. It is because that due to the existence of moving human bodies, the CSI or the multipath profiles in the environment deviate accordingly and keep changing. However, with the help of smoothing over the time domain, the dynamic changes in multipath profiles introduced by human motions can be trimmed out.

3.4 Summary

In this chapter, we proposed a novel wireless indoor events detection system, TRIEDS, by leveraging the TR technique to capture changes in the indoor multipath environment. TRIEDS enables low-complexity devices with the single antenna, operating in the ISM band to detect indoor events even through the walls. TRIEDS utilized the TR spatial-temporal resonances to capture the changes in the EM propagation environment and naturally compresses the high-dimensional features by mapping multipath profiles into the TR space, enabling the implementation of simple and fast detection algorithms. Moreover, we built a real prototype to validate the feasibility and to evaluate the performance of the proposed system. According to the experimental results for detecting the states of wooden doors in both controlled and dynamic environments, TRIEDS can achieve a detection rate over 96.92% while maintaining a false alarm rate smaller than 3.08% under both LOS and NLOS transmissions. The proposed TRIEDS introduces a novel idea to apply the TR technique to capture the variations in the multipath propagation environments for future surveillance systems.

Chapter 4

Indoor Monitoring: Statistical Learning over Time-Reversal Space

Thanks to its capability of capturing the difference between different CSI, TR technique has been applied to wireless event detection in an indoor environment [82]. Even though the proposed system achieved an accuracy over 96.9% in detecting multiple events by utilizing information in the complex valued CSI, the system required a transmission under 125MHz bandwidth which can not be implemented with commodity WiFi. Moreover, it has no experimental results which evaluates the accuracy in motion detection. Meanwhile, it lacks a long-term study on performance in practical use with critical interference introduced by resident activities.

Given the limitation of the aforementioned study and other wireless sensing technique discussed in Section 1.1, we are motivated to develop a new indoor monitoring system that not only can fully utilize the information embedded in multipath channels, but also support simple implementation with commercial WiFi devices while maintaining a high detection accuracy. To achieve this goal, we propose TRIMS (abbreviation for the TR based Indoor Monitoring System), which utilizes both the amplitude and the phase information in the CSI obtained from off-the-shelf WiFi devices and succeeds in monitoring indoor environments in real time under both LOS and NLOS sensing scenarios. In particular, TRIMS is implemented on

off-the-shelf WiFi devices which operate around 5.8 GHz with 40 MHz bandwidth, and capable of both multi-event detection and motion detection.

Moreover, unlike the aforementioned works that use the TRRS directly as a similarity score for recognition and localization, TRIMS relies on the statistical behavior of TRRS to differentiate different events. The statistics of TRRS is derived in this chapter and used as features in TRIMS for event detection and motion monitoring.

The rest of this chapter is organized as follows. We introduce the theoretical foundation of the proposed system and derive the statistics of TRRS in Section 4.1. Section 4.2 presents an overview of the proposed TRIMS as well as the details of both the event detector and the motion detector in TRIMS. The performance of TRIMS is studied and evaluated in Section 4.3, where the long-term behavior of TRIMS is also investigated. We briefly discuss the future works as well as the limitations in Section 4.4. This chapter is concluded in Section 4.5.

4.1 System Model

In this section, the theoretical foundation of the proposed smart radio system, TRIMS, is discussed. We derive the statistics of intra-class TRRS, which later is used as the feature for the event detector in TRIMS.

4.1.1 Statistics of TRRS

Based on the assumption of channel stationarity, if CFRs $\mathbf{h}_{F,0}$ and $\mathbf{h}_{F,1}$ are captured from the same indoor multipath propagation environment, we can model $\mathbf{h}_{F,1}$ as

$$\mathbf{h}_{F,1} = \mathbf{h}_{F,0} + \mathbf{n} \tag{4.1}$$

where $\mathbf{n}$ is the Gaussian noise vector, $\mathbf{n} \sim \mathcal{CN}(\mathbf{0}, \frac{\sigma^2}{L}\mathbb{I})$, and $E\Big[\|\mathbf{n}\|^2\Big] = \sigma^2$ with $\|\cdot\|_2$ representing the L2-norm of a vector.

Without loss of generality, we assume unit channel gain for $\mathbf{h}_{F,0}, i.e., \|\mathbf{h}_{F,0}\|^2 = 1$. Then, the TRRS between $\mathbf{h}_{F,0}$ and $\mathbf{h}_{F,1}$, as defined in (2.9), can be calculated as

$$\mathcal{TR}(\mathbf{h}_{F,0}, \mathbf{h}_{F,1}) = \frac{\Big|\sum_k h^*_{F,0}[k](h_{F,0}[k] + n[k])\Big|^2}{\|\mathbf{h}_{F,0}\|^2\|\mathbf{h}_{F,0} + \mathbf{n}\|^2} = \frac{\Big|1 + \mathbf{h}^{\mathrm{H}}_{F,0}\mathbf{n}\Big|^2}{\|\mathbf{h}_{F,0} + \mathbf{n}\|^2} \tag{4.2}$$

where $(\cdot)^{\mathrm{H}}$ denotes the Hermitian operator, i.e., transpose and conjugate.

Based on (4.2), we introduce a new metric γ and its definition is given by the following.

$$\gamma = 1 - \mathcal{TR}(\mathbf{h}_{F,0}, \mathbf{h}_{F,1}) = 1 - \frac{\Big|1 + \mathbf{h}^{\mathrm{H}}_{F,0}\mathbf{n}\Big|^2}{\|\mathbf{h}_{F,0} + \mathbf{n}\|^2} = \frac{\|\mathbf{n}\|^2 - \Big|\mathbf{h}^{\mathrm{H}}_{F,0}\mathbf{n}\Big|^2}{\|\mathbf{h}_{F,0} + \mathbf{n}\|^2} \tag{4.3}$$

According to the Cauchy-Schwartz inequality, we can have $|\mathbf{h}^{\mathrm{H}}_{F,0}\mathbf{n}|^2 \leq \|\mathbf{n}\|^2\|\mathbf{h}_{F,0}\|^2$, with equality holds if and only if $\mathbf{n}$ is a multiplier of $\mathbf{h}_{F,0}$, which is rare to happen since $\mathbf{n}$ is a Gaussian random vector and $\mathbf{h}_{F,0}$ is deterministic. Hence, we can assume $\|\mathbf{n}\|^2 > |\mathbf{h}^{\mathrm{H}}_{F,0}\mathbf{n}|^2$ given $\|\mathbf{h}_{F,0}\|^2 = 1$, leading to $\gamma > 0$.

By taking the logarithm on both sides of (4.3), we have

$$\ln(\gamma) = \ln\Big(\|\mathbf{n}\|^2 - |\mathbf{h}^{\mathrm{H}}_{F,0}\mathbf{n}|^2\Big) - \ln\Big(\|\mathbf{h}_{F,0} + \mathbf{n}\|^2\Big). \tag{4.4}$$

Let us denote $X = \frac{2L}{\sigma^2}\|\mathbf{n}\|^2$, $Y = \frac{2L}{\sigma^2}|\mathbf{h}_{F,0}^{\mathrm{H}}\mathbf{n}|^2$ and $Z = \frac{2L}{\sigma^2}\|\mathbf{h}_{F,0} + \mathbf{n}\|^2$. It is easy to prove that $X \sim \chi^2(2L)$, $Y \sim \chi^2(2)$ and $Z \sim \chi'^2_{2L}(\frac{2L}{\sigma^2})$. Here, $\chi^2(k)$ denotes a chi-squared distribution with k degrees of freedom, and $\chi'^2_k(\mu)$ represents a non-central chi-squared distribution with k degrees of freedom and non-centrality parameter μ. By utilizing the statistics of X, Y, and Z, we can have the following properties as

$$\begin{aligned} E\Big[\|\mathbf{n}\|^2\Big] = \sigma^2,\ Var\Big[\|\mathbf{n}\|^2\Big] = \tfrac{\sigma^4}{L}, \\ E\Big[|\mathbf{h}_{F,0}^{\mathrm{H}}\mathbf{n}|^2\Big] = \tfrac{\sigma^2}{L},\ Var\Big[|\mathbf{h}_{F,0}^{\mathrm{H}}\mathbf{n}|^2\Big] = \tfrac{\sigma^4}{L^2} \\ E\Big[\|\mathbf{h}_{F,0} + \mathbf{n}\|^2\Big] = 1 + \sigma^2,\ Var\Big[\|\mathbf{h}_{F,0} + \mathbf{n}\|^2\Big] = \tfrac{\sigma^4 + 2\sigma^2}{L} \end{aligned} \tag{4.5}$$

where $E[\cdot]$ denotes the expectation and $Var[\cdot]$ represents the variance.

According (4.5), it is reasonable to establish the following approximation as $|\mathbf{h}_{F,0}^{\mathrm{H}}\mathbf{n}|^2 \simeq \frac{\sigma^2}{L}$, whose mean square error of approximation is equal to $Var\Big[|\mathbf{h}_{F,0}^{\mathrm{H}}\mathbf{n}|^2\Big] = \frac{\sigma^4}{L^2}$. Considering that in a typical OFDM system σ^4 usually has a magnitude smaller than 10^{-4} after normalization while L^2 is about 10^4, we have $Var\Big[|\mathbf{h}_{F,0}^{\mathrm{H}}\mathbf{n}|^2\Big] = \frac{\sigma^4}{L^2} \to 0$. Then, substituting $|\mathbf{h}_{F,0}^{\mathrm{H}}\mathbf{n}|^2$ with $\frac{\sigma^2}{L}$, (4.4) becomes the following.

$$\begin{aligned} \ln(\gamma) &\simeq \ln\Big(\frac{\sigma^2}{2L}X - \frac{\sigma^2}{L}\Big) - \ln\Big(\frac{\sigma^2}{2L}Z\Big) \\ &= \ln(\sigma^2) + \ln\Big(\frac{1}{2L}X - \frac{1}{L}\Big) - \ln\Big(\frac{\sigma^2}{2L}Z\Big) \end{aligned} \tag{4.6}$$

Moreover, considering that it is typical to have $L > 100$ and $\sigma^2 < 10^{-2}$ in a real OFDM system, $\frac{1}{2L}X - \frac{1}{L} \to 1$ with a mean square error being $1/L^2 + 1/L$ which approximates to 0. Similarly, it is easy to derive that $\frac{\sigma^2}{2L}Z \to 1$. By utilizing the linear approximation of logarithm, i.e., $\ln(x+1) \simeq x$ when $x \to 0$, along with

$\frac{1}{2L}X - \frac{1}{L} \to 1$ and $\frac{\sigma^2}{2L}Z \to 1$, (4.6) can be approximated as follows.

$$\begin{aligned} \ln(\gamma) &\simeq \ln(\sigma^2) + \Big(\frac{1}{2L}X - \frac{1}{L} - 1\Big) - \Big(\frac{\sigma^2}{2L}Z - 1\Big) \\ &= \ln(\sigma^2) - \frac{1}{L} + \frac{1}{2L}\Big(X - \sigma^2 Z\Big) \end{aligned} \tag{4.7}$$

Referring to the definition of X and Z, the last term in (4.7) can be rewritten as

$$X - \sigma^2 Z = \frac{2L}{\sigma^2}\|\mathbf{n}\|^2 + 2L\|\mathbf{h}_{F,0} + \mathbf{n}\|^2 = \sum_{i=1}^{2L} W_i$$

where W_i is defined as follows.

$$W_i = \begin{cases} w_i^2 - (\sqrt{2L}\Re\{h_{F,0}[k]\} + \sigma w_i)^2, & \text{if } i = 2k \\ w_i^2 - (\sqrt{2L}\Im\{h_{F,0}[k]\} + \sigma w_i)^2, & \text{if } i = 2k-1 \end{cases} \tag{4.8}$$

Here, w_i is independent and identically distributed (i.i.d.) with $w_i \sim \mathcal{N}(0,1), \forall i$. $\Re\{\cdot\}$ denotes the function to take the real part of a complex value while $\Im\{\cdot\}$ for the imaginary part. Given the statistics of w_i, the mean and variance of W_i are derived and listed in (4.9) and (4.10), respectively,

$$E\Big[W_i\Big] = \begin{cases} 1 - 2L\Re\{h_{F,0}[k]\}^2 - \sigma^2, & \text{if } i = 2k \\ 1 - 2L\Im\{h_{F,0}[k]\}^2 - \sigma^2, & \text{if } i = 2k-1 \end{cases} \tag{4.9}$$

and

$$Var\Big[W_i\Big] = \begin{cases} 2\Big(1 + \sigma^4 + (2L\Re\{h_{F,0}[k]\}^2 - 1)\sigma^2\Big), \\ \qquad \text{if } i = 2k \\ 2\Big(1 + \sigma^4 + (2L\Im\{h_{F,0}[k]\}^2 - 1)\sigma^2\Big), \\ \qquad \text{if } i = 2k-1 \end{cases} \tag{4.10}$$

Due to the fact that $L > 100$ in typical OFDM system, $\sum_i^{2L} W_i$ will exhibit an asymptotic behavior, according to the *Central Limit Theorem*. Hence we define

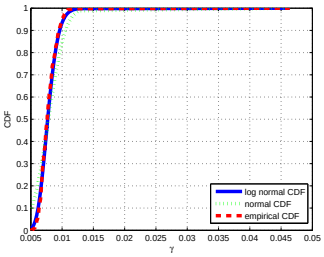

(a) Distribution fitting for 500 real CSI measurements.

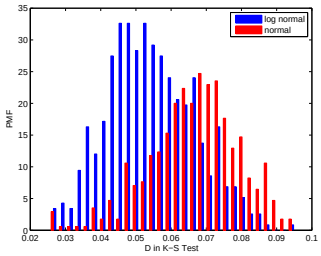

(b) The histogram of scores of K-S test from 500 real CSI measurements.

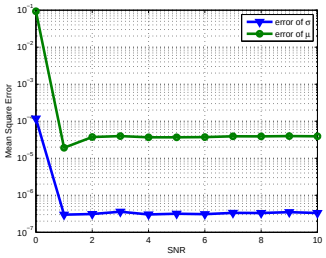

(c) The mean square error of log-normal parameter estimation for simulated CFRs.

Figure 4.1: Examples for evaluating the derived statistical model.

a new normal-distributed variable S_{2L} as follows.

$$S_{2L} = \frac{\sum_i^{2L} W_i + 2L\sigma^2}{\sqrt{4L(1+\sigma^4)}} \sim \mathcal{N}(0,1) \tag{4.11}$$

After substituting (4.11) into (4.8), we finally get the statistical distribution of γ as follows.

$$\begin{aligned} \ln(\gamma) &\simeq \ln(\sigma^2) - \frac{1}{L} + \frac{1}{2L}\sum_{i=1}^{2L} W_i \\ &= \ln(\sigma^2) - \frac{1}{L} - \sigma^2 + \frac{\sqrt{4L(1+\sigma^4)}}{2L} S_{2L} \\ &\sim \mathcal{N}\left(\ln(\sigma^2) - \frac{1}{L} - \sigma^2, \frac{1+\sigma^4}{L}\right) \end{aligned} \tag{4.12}$$

Hence, the metric γ, i.e., $1-\mathcal{TR}(\mathbf{h}_{F,0}, \mathbf{h}_{F,1})$, follows the log-normal distribution with the location parameter $\mu_{\text{logn}} = \ln(\sigma^2) - \frac{1}{L} - \sigma^2$ and the scale parameter $\sigma_{\text{logn}} = \sqrt{\frac{1+\sigma^4}{L}}$.

The derived statistical model is verified by fitting over real measured CSI samples and CSI samples generated from the model in (4.1), as shown in Figure 4.1. Firstly, we adopt the Kolmogorov-Smirnov test (K-S test) to quantitatively evaluate

the accuracy of the derived log-normal distribution model on the real CSI measurements. The score of K-S test is denoted as D which measures the difference between the empirical cumulative distribution function (E-CDF) and the log-normal cumulative distribution function (CDF). As depicted by the example in Figure 4.1(a) and Figure 4.1(b), the log-normal distribution fits better over CSI samples captured from real channels, compared with the normal distribution. Moreover, the derived log-normal distribution model is further investigated on simulated CSI samples through studying the mean square errors of parameter estimations against the SNR, a.k.a., σ^{-1} in dB. As plotted in Figure 4.1(c), in terms of parameter estimation for the log-normal distribution, the derived model is accurate with almost zero mean square error, especially when SNR is high.

4.2 Proposed Algorithms

Can WiFi perceive an indoor environment? To answer this question, in this chapter, we propose an intelligent indoor monitoring system, TRIMS, which enables real-time indoor monitoring with commercial WiFi devices by leveraging TR technique. This novel indoor monitoring system consists of the following components.

1. Event Detector: With the purpose of perceiving a monitored environment and recognizing specific events, an event detector is included in TRIMS. The proposed event detector in TRIMS relies on TR technique to evaluate the difference and similarity between various indoor events. It consists of an offline training phase where the CSI and corresponding statistics of training events

are learnt and an online monitoring phase where the event detector of TRIMS will report the occurrence of trained events in real time. The details are discussed in Section 4.2.1.

2. Motion Detector: TRIMS not only has the functionality of detecting the occurrence of trained events, it is also capable of detecting dynamics in the environment, i.e., motion inside the protected area. The proposed motion detector leverages fluctuations in TRRS values within a time window to indicate environmental dynamics and the sensitivity is auto-adapted for each environment through the training phase. In Section 4.2.2, we will introduce details of the proposed motion detector in TRIMS.

4.2.1 TRIMS: Event Detector

By leveraging the fundamental theories and techniques proposed in Section 4.1, we design a real-time event detection module in TRIMS, utilizing the statistics of TRRS between the CSI as the metric for categorizing indoor environments and recognizing different indoor events. In this section, the details of statistics based event detector are introduced, and the diagram illustrating how the event detector works is shown in Figure 4.2. The details are discussed in the following.

4.2.1.1 Offline Training Phase

In the offline training phase, the proposed system aims to build a database that stores, for each of the training events, the log-normal statistics of TRRSs between

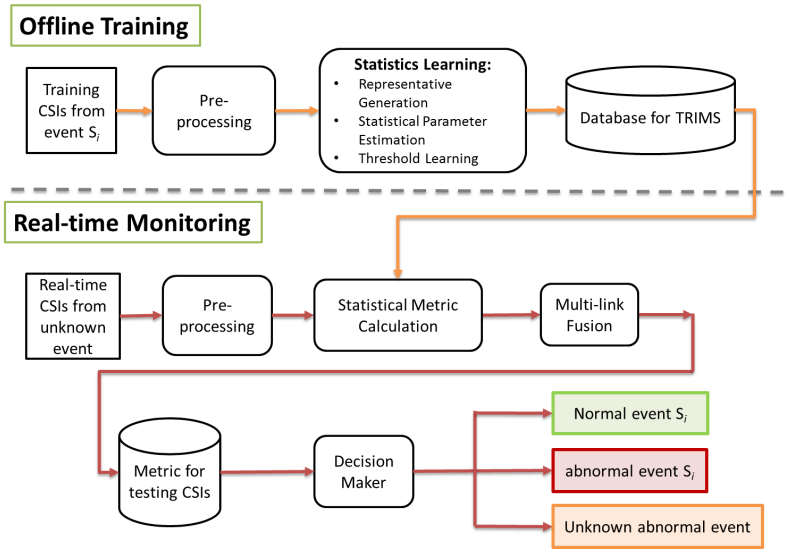

Figure 4.2: Diagram of the proposed event detector in TRIMS.

the intra-class CSI and a representative CSI sample.

Specifically, for each indoor event $S_i \in \mathcal{S}$ with $\mathcal{S}$ being the set of indoor events to be monitored, the corresponding CFRs are obtained through channel sounding and estimated at the receiver side as,

$$\mathbf{H}_{F,i} = \left[\mathbf{h}_{F,i}^{(1)},\ \mathbf{h}_{F,i}^{(2)},\ \cdots,\ \mathbf{h}_{F,i}^{(M)}\right],\quad i = 1,\ 2,\ \cdots,\ N \tag{4.13}$$

where N is the size of $\mathcal{S}$, i.e., the number of events of interest, M is the number of links between the transmitter and the receiver. Each link represents the channel between a single TX-RX antenna pair. The dimension of $\mathbf{H}_{F,i}$ is $L \times M$ with L being the number of active subcarriers in a wireless OFDM system. The statistics of intra-class TRRS is estimated through the following steps.

- **Preprocessing:** A phase sanitization algorithm is applied to compensate all CFRs for phase offsets, which are introduced by CFO, SFO and STO.

- **CSI Representative Generation:** For each link m, a CSI representative is

found for every indoor event S_i in the training set. The CSI representative is selected as the one that is most similar to all other CFRs on link m from S_i. In particular, to quantitatively evaluate the similarity, the pair-wise TRRSs on link m between all the CFRs collected for indoor event S_i are calculated first. Then the CSI representative is selected on link m for event S_i as the one that is most similar to the majority of other CSI samples in the same class. $\mathbf{H}_{rep,i}$ is the collection of CSI representatives on all links for event S_i, which is defined as follows.

$$\mathbf{H}_{rep,i} = \Big[\mathbf{h}_{rep,i}^{(1)},\ \mathbf{h}_{rep,i}^{(2)},\ \cdots,\ \mathbf{h}_{rep,i}^{(M)}\Big], \forall i \tag{4.14}$$

- **Lognormal Parameter Estimation:** Once the CSI representative is selected, the log-normal distribution parameters can be estimated from intra-class TRRSs. For link m and event S_i, the TRRSs between the CSI representative $\mathbf{h}_{rep,i}^{(m)}$ and all other realizations $\mathbf{h}_{F,i}^{(m)}(n),\ \forall\ n$ are calculated using (2.9) and denoted as

$$\mathcal{TR}_i^{(m)}(n) = \mathcal{TR}\Big(\mathbf{h}_{rep,i}^{(m)}, \mathbf{h}_{F,i}^{(m)}(n)\Big),\quad n = 1, 2, \cdots, Z-1 \tag{4.15}$$

where n is the realization index of CFRs collected for event S_i, and Z is the total number of CFRs. Then the log-normal parameters $(\mu_i^{(m)}, \sigma_i^{(m)})$ of $\gamma = 1 - \mathcal{TR}_i^{(m)}$ for event S_i on link m are estimated by

$$\mu_i^{(m)} = \frac{1}{Z-1}\sum_{n=1}^{Z-1} \ln\Big(1 - \mathcal{TR}_i^{(m)}(n)\Big) \tag{4.16}$$

$$\sigma_i^{(m)} = \sqrt{Var\Big[\ln\Big(1 - \mathcal{TR}_i^{(m)}\Big)\Big]} \tag{4.17}$$

where $Var[\cdot]$ is the sample variance function.

The training database is built with the collection of CSI representatives and log-normal distribution parameters for all the trained events. All the trained events can be divided into two groups: the normal events group $\mathcal{S}_{normal}$ where no alarm will be sounded when being detected, and the abnormal events group $\mathcal{S}_{abnormal}$ where an alarm will be reported to users when an abnormal event is detected.

- **Threshold Learning:** Based on the knowledge of $\mathcal{H}_{rep}$ and $\mathcal{Q}_{rep}$, the system builds the normal event checker and the abnormal event checker, through which the label of the testing CSI sample is determined in the monitoring phase. To determine whether event a testing CSI sample $\mathbf{H}_{F,test}$ belongs to an event S_i, a score is calculated first as

$$\mathcal{W}_{i,test} = \prod_{m=1}^{M} \mathcal{W}_{i,test}^{(m)} = \prod_{m=1}^{M} F_{(\mu_i^{(m)},\sigma_i^{(m)})}\Big(1 - \mathcal{TR}_{i,test}^{(m)}\Big) \tag{4.18}$$

where $\mathcal{TR}_{i,test}^{(m)} = \mathcal{TR}\Big(\mathbf{h}_{rep,i}^{(m)}, \mathbf{h}_{F,test}^{(m)}\Big)$. $\mathcal{W}_{i,test}^{(m)}$ is the statistical metric on link m of $\mathbf{H}_{F,test}$ conditioned on event S_i, defined as the value of log-normal CDF of $1 - \mathcal{TR}_{i,test}^{(m)}$ with parameter being $\mu_i^{(m)}$ and $\sigma_i^{(m)}$. The operation $\prod_{m=1}^{M}(\cdot)$ fuses the information among all links. $F_{(\mu,\sigma)}(x)$ represents the CDF of log-normal distribution with parameters (μ, σ) and the variable x.

The smaller the value of $\mathcal{W}_{i,test}^{(m)}$ is, the higher the probability for $\mathbf{H}_{F,test}$ belonging to event S_i is. Two thresholds γ_{normal} and $\gamma_{abnormal}$ are required for the normal event checker and the abnormal event checker to define the boundary for the value of metric $\mathcal{W}_{i,j}$. Consequently, when the value of $\mathcal{W}_{i,test}$ falls below

the threshold γ_{normal} or $\gamma_{abnormal}$, $\mathbf{H}_{F,test}$ is viewed as from event S_i. Hence, in order to correctly distinguish different events, both γ_{normal} and $\gamma_{abnormal}$ are carefully learned based on the metrics $\mathcal{W}_{i,test}$ where $\mathbf{H}_{F,test}$ is replaced by $\mathbf{H}_{rep,j}$ during the training phase. The criteria for choosing γ_{normal} and $\gamma_{abnormal}$ are as follows.

$$\begin{aligned} \gamma_{normal} &= \min_{S_i \in \mathcal{S}_{normal},\ S_j \in \mathcal{S}_{abnormal}} \mathcal{W}_{i,j} \\ \gamma_{abnormal} &= \min_{S_i \in \mathcal{S}_{abnormal},\ S_j \in \mathcal{S},\ S_j \neq S_i} \mathcal{W}_{i,j} \end{aligned} \tag{4.19}$$

4.2.1.2 Online Monitoring Phase

The statistics based event detector is designed to identify the real-time indoor events with the knowledge of training database. Once the occurrence of a trained event is detected, the system will decide to sound an alarm based on the characteristics of that event. If an untrained event is detected, the system will also notify user about the situation. The details are discussed as follows.

During the monitoring phase, the receiver keeps monitoring the environment by collecting the CSI as $\mathbf{H}_{F,test} = \left[\mathbf{h}_{F,test}^{(1)},\ \mathbf{h}_{F,test}^{(2)},\ \cdots,\ \mathbf{h}_{F,test}^{(M)}\right]$.

- **Statistical Metric Calculation:** Since the obtained CSI measurement $\mathbf{H}_{F,test}$ is corrupted by random phase offsets, a phase sanitization algorithm is applied. After that, for each trained indoor event, the TRRS between the CSI representative and the testing measurement is calculated. Given the TRRSs between the testing CSI sample and trained events, the statistical metric $\mathcal{W}_{i,test}$ between $\mathbf{H}_{F,test}$ and the trained event S_i is calculated using (4.18).

- **Decision:** The statistical metric $\mathcal{W}_{i,test}^{(m)}$ is a monotonic function of $\mathcal{TR}_{i,test}^{(m)}$ which depicts the similarity between the testing CSI samples and the CSI representative of event S_i. In other words, the more similar two CSI samples are, the smaller the value of $\mathcal{W}_{i,test}$ is. The detailed decision protocol based on $\mathcal{W}_{i,test}$ is described in the following.

  1. *Step 1 - normal event checker*:

     To begin with, the event detector checks whether the environment is normal, i.e., only one of the normal events in S_{normal} occurs, by the following rule.

$$D_{event} = \begin{cases} \arg \min\limits_{S_i \in \mathcal{S}_{normal}} \mathcal{W}_{i,test}, \\ \quad \text{if } \min\limits_{S_i \in \mathcal{S}_{normal}} \mathcal{W}_{i,test} \leq \gamma_{normal} \\ \text{go to } \textit{Step 2}, \text{ otherwise} \end{cases} \tag{4.20}$$

  2. *Step 2 - abnormal event checker*:

     In order to determine which trained abnormal event in $S_{abnormal}$ occurs, it follows the rule below:

$$D_{event} = \begin{cases} \arg \min\limits_{S_i \in \mathcal{S}_{abnormal}} \mathcal{W}_{i,test}, \\ \quad \text{if } \min\limits_{S_i \in \mathcal{S}_{abnormal}} \mathcal{W}_{i,test} \leq \gamma_{abnormal} \\ 0, \text{ otherwise} \end{cases} \tag{4.21}$$

     where $D_{event} = 0$ indicates the occurrence of some untrained event.

To summarize, the event detector labels the CSI sample $\mathbf{H}_{F,test}$ by the following

rule.

$$D_{event} = \begin{cases} \arg \min\limits_{S_i \in \mathcal{S}_{normal}} \mathcal{W}_{i,test}, \\ \qquad \text{if } \min\limits_{S_i \in \mathcal{S}_{normal}} \mathcal{W}_{i,test} \leq \gamma_{normal} \\ \arg \min\limits_{S_i \in \mathcal{S}_{abnormal}} \mathcal{W}_{i,test}, \\ \qquad \text{if } \min\limits_{S_i \in \mathcal{S}_{normal}} \mathcal{W}_{i,test} > \gamma_{normal} \text{ and} \\ \qquad\quad \min\limits_{S_i \in \mathcal{S}_{abnormal}} \mathcal{W}_{i,test} \leq \gamma_{abnormal} \\ 0, \qquad \text{otherwise} \end{cases} \tag{4.22}$$

4.2.2 TRIMS: Motion Detector

TRIMS is designed not only to determine which trained indoor event happens, but also to detect if environment has any dynamics by means of a motion detector proposed in TRIMS.

Motion always introduces fluctuations in the radio propagation environment, leading to significant changes of TRRSs between CSI samples within a time window. The impact introduced by motion is larger compared to the impacts brought by channel fading and noise, especially when motion happens close to the transmitter or the receiver. In this part, we propose a motion detector which uses the variance of TRRSs between CSI samples within an observation window as the metric to indicate the indoor dynamics. The proposed motion detector consists of two phases: an offline training phase and a real-time monitoring phase. The flow chart of the proposed motion detector is depicted in Figure 4.3.

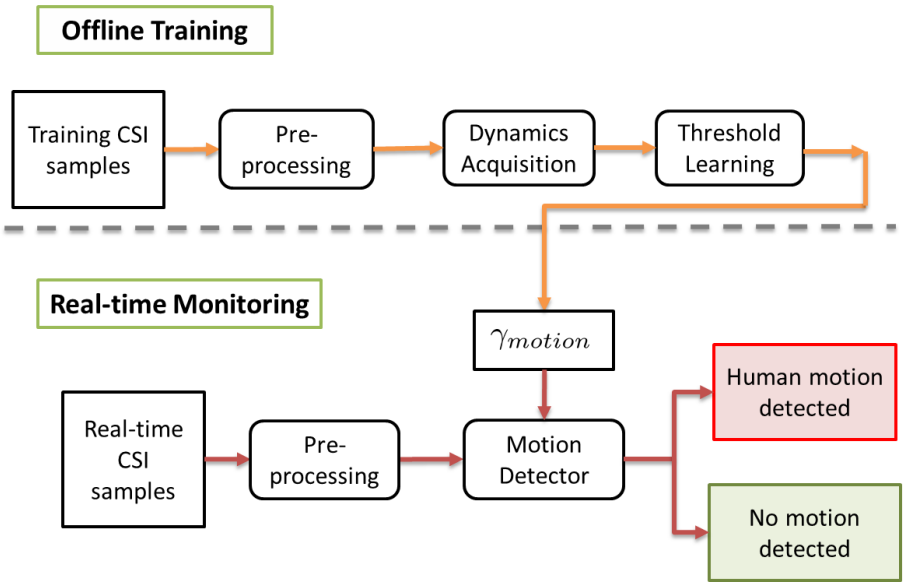

Figure 4.3: Diagram of the proposed motion detector in TRIMS.

4.2.2.1 Phase I. Offline Training

In the training phase, the proposed motion detector is trained with the dynamics, measured by the variance of a TRRSs time sequence, under both the static state and the dynamic state with motion in the indoor environment. The detailed steps are listed as follows.

- **Data Acquisition:** First, the state of an indoor environment is divided into two classes: $\mathcal{S}_1$ where the environment is static, and $\mathcal{S}_0$ where there is some motion happening in the monitoring area. The CSI is collected continuously in time for both classes as $\mathbf{H}_{F,i}(t) = [\mathbf{h}_{F,i}^{(1)}(t),\ \mathbf{h}_{F,i}^{(2)}(t),\ \cdots,\ \mathbf{h}_{F,i}^{(M)}(t)]$, where $\mathbf{H}_0(t)$ is collected when the environment is static and $\mathbf{H}_1(t)$ is from the dynamic environment. t is the time instance when the CFR is captured. The phase offset in CFRs is compensated individually and independently before learning the dynamics.

- **Dynamics Acquisition:** After time sequences of CFR measurements under both static state $\mathcal{S}_0$ and dynamic state $\mathcal{S}_1$ are obtained, the environmental dynamics is evaluated by tracking the variance of TRRSs within a time window. To study the variance under both states $\mathcal{S}_i$, $i = 0, 1$, a sliding window with length W samples and overlap $W-1$ is applied on the time sequence of $\mathbf{H}_{F,i}(t)$. For example, in a window of length W, CFRs from $\mathbf{H}_{F,i}(t_0)$ to $\mathbf{H}_{F,i}(t_0 + (W - 1) * T_s)$ are stored, where T_s is the channel probing interval. Within each window, the corresponding TRRS sequence between t_0 and $t_0 + (W - 1) * T_s$ is denoted as $\mathcal{TR}\Big(\mathbf{H}_{F,i}(t_0), \mathbf{H}_{F,i}(t)\Big)$, $t_0 \leq t \leq t_0 + (W - 1) * T_s$, which is calculated as follows.

$$\mathcal{TR}\Big(\mathbf{H}_{F,i}(t_0), \mathbf{H}_{F,i}(t)\Big) = \frac{\sum_{m=1}^{M} \mathcal{TR}\Big(\mathbf{h}_{F,i}^{(m)}(t_0), \mathbf{h}_{F,i}^{(m)}(t)\Big)}{M} \tag{4.23}$$

Then the dynamics within the time window can be quantitatively evaluated by the variance of $\Big\{\mathcal{TR}\Big(\mathbf{H}_{F,i}(t_0), \mathbf{H}_{F,i}(t)\Big),\ t_0 \leq t \leq t_0 + (W - 1) * T_s\Big\}$, which is denoted as $\sigma_i(t_0), i = 0, 1$. In order to have a fair and comprehensive analysis, multiple $\sigma_i's, i = 0, 1$ are captured at different time.

- **Threshold Learning:** After dynamics acquisition, multiple instances of σ_0 and σ_i are obtained, and the threshold γ_{motion} for differentiating between S_0 and S_i is determined by

$$\gamma_{motion} = \begin{cases} \alpha \max_t \sigma_0(t) + (1 - \alpha)\overline{\sigma_1(t)}, \\ \qquad \text{if } \max_t \sigma_0(t) \leq \overline{\sigma_1(t)} \\ \max_t \sigma_0(t), \text{ otherwise}, \end{cases} \tag{4.24}$$

where $\overline{\sigma_1(t)}$ denotes the average of multiple $\sigma_1's$ captured at different time. $\alpha,\ 0 \leq \alpha \leq 1$, is a sensitivity coefficient for motion detections in that the sensitivity of the proposed motion detector increases as α decreases.

4.2.2.2 Phase II. Online Monitoring

During the online monitoring phase, the dynamics in the environment is tracked by comparing the variance on real-time TRRSs with γ_{motion} as:

$$D_{motion}(t_0) = \begin{cases} 1,\ \sigma_{test}(t_0) \geq \gamma_{motion}, \\ 0,\ \text{otherwise}, \end{cases} \tag{4.25}$$

where $\sigma_{test}(t_0)$ is the variance on the testing TRRS sample sequence within a window of length W and overlap $W-1$ at time instance t_0. $D_{motion}(t_0) = 1$ indicates the existence of motion, i.e., someone is moving inside the monitoring area, while $D_{motion}(t_0) = 0$ means the environment is static.

4.2.3 TRIMS: Time Diversity for Smoothing

In a real environment, noise in wireless transmission and outside activities exist and corrupt the estimated CSI, leading to a misdetection or a false alarm in both the event detector and the motion detector of TRIMS. However, by leveraging the fact that these interferences are typically sparse and abrupt, a smoothing method relying on the time diversity is proposed to address that problem.

The essential idea of the proposed time-diversity smoothing algorithm is by applying the majority vote over decisions of each testing CSI sample, assuming that

the typical indoor event lasts for a couple of seconds. In both of the event detector and the motion detector, decisions will be accepted only if they are consistent along a short time period. The details are as follows.

With the help of a sliding window SW whose length is W and overlap length is O, the decisions $D_{out}(n)$ at time index n is obtained through

$$D_{out}(w) = \mathrm{MV}\Big\{ D_{in}(1 + (w-1) * O), \cdots, D_{in}(W + (w-1) * O) \Big\} \tag{4.26}$$

where $D_{in}(w)$ is the input decision sample at time index w, $\mathrm{MV}\{\cdot\}$ is the operator for taking majority vote. The corresponding time delay introduced by the sliding window SW is in general $(W - O) \times T$, where T is the time interval between consecutive D_{in} samples.

For example, in order to alleviate false alarms introduced by outside activities and imperfect CSI estimation to the proposed event detector, a two-level time-diversity smoothing is applied as follows.

1. *Level I:* A majority vote is applied directly on the raw decisions D_{motion} of each single CSI sample. Given a sliding window SW_1 whose length is W_1 and overlap length is O_1, the decisions of index w, $D_{MV1}(w)$, is obtained from taking a majority vote over $D_{event}(i + (w-1) * O_1)$, $1 \leq i \leq W_1$.

2. *Level II:* A second sliding window SW_2 is applied on $D_{MV1}(w)$ with length W_2 and overlap O_2. Consequently, the final decision output is $D_{final}(n)$. The system suffers a time delay $(W_2 - O_2) \times (W_1 - O_1) \times T_s$.

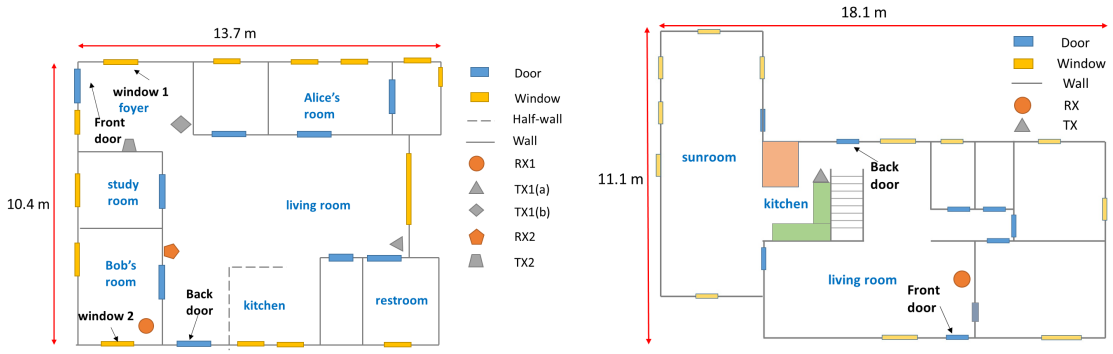

(a) The floorplan of House #1

(b) The floorplan of House #2.

Figure 4.4: Experimental setting for TRIMS: floorplans.

4.3 Experimental Results

In order to evaluate the feasibility and the performance of the proposed TRIMS in indoor monitoring, extensive experiments have been conducted.

4.3.1 Experimental Setting

We build a prototype on commodity WiFi devices performing 3×3 multiple-input and multiple-output (MIMO) transmission at 5.845GHz carrier frequency under the IEEE 802.11n standard. According to the IEEE 802.11n standard, both 2.4GHz band and 5GHz band support a 40 MHz bandwidth and the CSI at those two bands should share the same resolution. Therefore, with the obtained CSI, the proposed system should achieve a detection performance at 2.4GHz similar to that from 5.8GHz. In the prototype, the CSI is extracted from the Qualcomm network interface card (NIC) and composed by a complex-valued matrix for accessible subcarriers on all 9 links. With a single pair of devices, we conduct extensive ex-

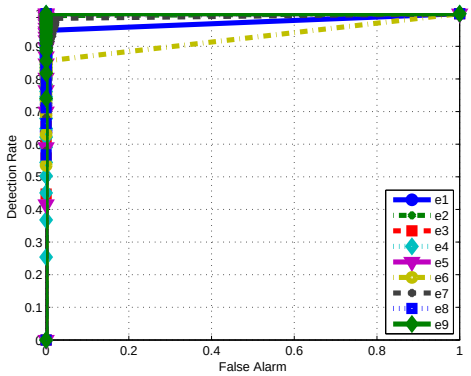

(a) ROC performance for all events (TX in the foyer).

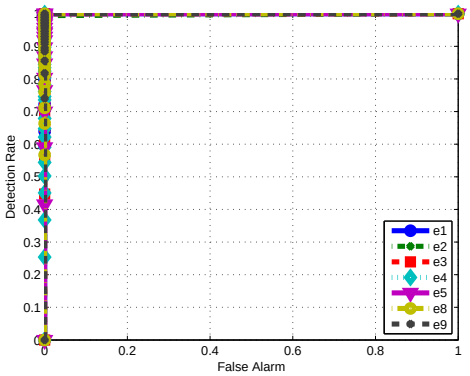

(b) ROC performance for targets events (TX in the foyer).

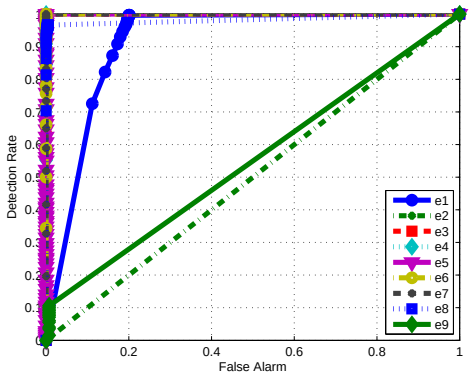

(c) ROC performance for all events (TX outside the study room).

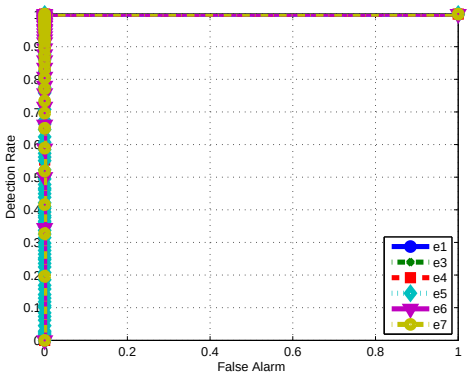

(d) ROC performance for targets events (TX outside the study room).

Figure 4.5: ROC performance for the proposed event detector.

periments in two real indoor environments: House #1 and House #2 with regular residence activities, whose floorplans are shown in Figure 4.4(a) and Figure 4.4(b). The locations of the transmitter and the receiver are marked on both floorplans.

4.3.2 TRIMS: Event Detection Performance

We start from the performance study of the proposed event detector in TRIMS and experiments are conducted in both facilities. In order to learn the statistics of

State Index	Description	State Index	Description
e1	All doors are closed.	e2	Front door open.
e3	Back door open.	e4	Bob's room door open.
e5	Study room door open.	e6	Alice's room door open.
e7	Restroom door open.	e8	Window 1 open.
e9	Window 2 open.		

Table 4.1: Events of interest in House #1.

intra-class TRRS, at least 300 realizations of CFRs corresponding to each indoor propagation environment should be collected. Furthermore, the CSI sounding rate is 100Hz in the training phase, while it becomes 30Hz in the real-time monitoring phase for the event detector in TRIMS. The two-level time diversity algorithm is applied in the event detector with $W_1 = 15, O_1 = 14, W_2 = 45, O_2 = 15$, considering that 30 CSI samples are collected per second.

4.3.2.1 Study on Location of TX-RX

As discussed in the previous sections, the proposed event detector is aimed at monitoring and detecting indoor events by leveraging the TR technique to capture changes in the CSI. Different events introduce different changes, depending on not only the characteristics of each indoor event but also the distance between the event location to the transceivers. The closer the indoor event is, the larger impact it

introduces. Hence, it is crucial to study how the locations of the TX and the RX affects the performance of the proposed event detector.

In House #1, we study the impact of TX-RX locations on TRIMS's performance in the event detection and the events of interest are listed in Table 4.1, while the candidate locations of TX and RX are labeled with "TX_1" and "RX_1" in Figure 4.4(a). The receiver is fixed in the study room while the transmitter is located either in the foyer against a wall or outside the restroom. The performance is evaluated through the receiver operating characteristic (ROC) curve, where the x-axis is the false alarm rate of an event e_i, i.e., the probability of other events being misclassified as e_i, whereas the y-axis is the detection rate of e_i.

As shown in Figure 4.5(a), the proposed event detector fails to differentiate between the CSI of e1, e6 and e7, in that the false alarm rates of e1, e6 and e7 are extremely high under the same detection rate, compared with others. The reason is that the changes in the wireless multipath channel introduced by e6 and e7 are too small for the proposed event detector to capture. A possible reason is that event e6 and e7 are far from the TX and the RX, when both devices are located in the front part of the house. Similarly, in Figure 4.5(c), when the TX is put outside the study room, i.e., in the back part of the house, event e2 and e8 are too far away while e9 is outside the circle range defined by the line segment between the TX and the RX. Consequently, the proposed event detector has an ambiguity over e1, e2, e8 and e9.

Here, we introduce the concept of "target event", to whom the proposed event detector has a perfect accuracy, as shown in Figure 4.5(b) and Figure 4.5(d). The target events are those events that satisfy a rule-of-thumb, which says that in order

to have it detected, the event should either be close to the TX-RX link or have a LOS path to one of the devices, given the location of the TX and the RX. Under the rule-of-thumb, the target event is able to change the CSI between the TX and the RX in a way that is significant enough. The proposed event detector can achieve a perfect ROC performance for target events.

4.3.2.2 Operational Test in House #1

In this part, to further study the performance of TRIMS in the real-time event monitoring, we imitate several intrusion and postman cases with locations of TX and RX being "TX_2" and "RX_2". In the intrusion test, an intruder enters the house from a door and walks inside the house before leaving from the same door. On the other hand, in the postman test, some one is walking outside the front door of each house to imitate a postman.

Moreover, in this part, the system is only trained for event e1, e2 and e3. In Figure 4.6, the system output is plotted along the time. The y-axis is the output decision, where "Allclosed" indicates e1, "Front" and "Back" represent e2 and e3 respectively, and "Unknown" means untrained events happening. Take Figure 4.6(a) as an example. The proposed event detector outputs state 1, i.e., "all doors are closed", during the test. As shown in Figure 4.6(c), during the test, the proposed event detector first reports e1 for about 20 seconds and then detects the occurrence of e2 when the front door is opened at the time index of the $20th$ second, with a single detection over the untrained event, i.e., the output falls to "Unknown". The

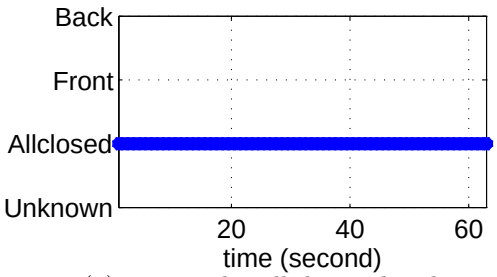

(a) Test under all doors closed.

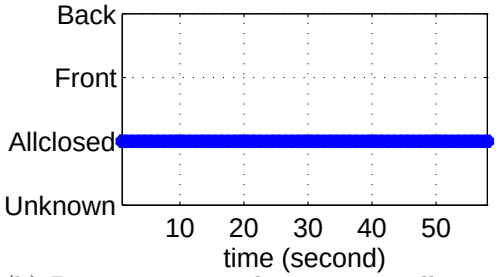

(b) Postman test with someone walking outside the front door.

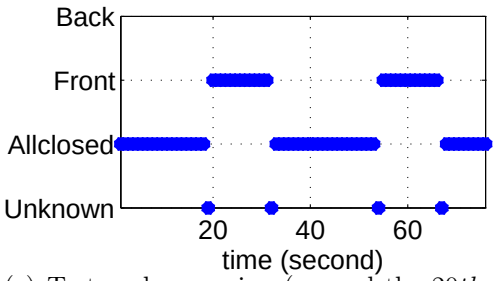

(c) Test under opening (around the $20th$ and the $50th$ second) and closing (around the $30th$ and the $60th$ second) front door from the outside the house twice.

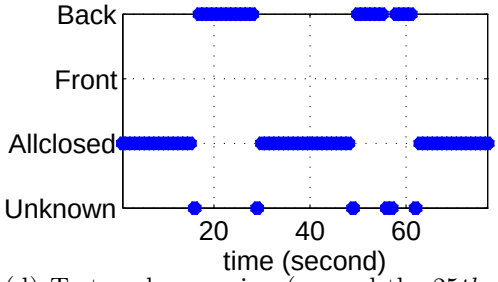

(d) Test under opening (around the $25th$ and the $55th$ second) and closing (around the $35th$ and the $65th$ second) back door from the outside the house twice.

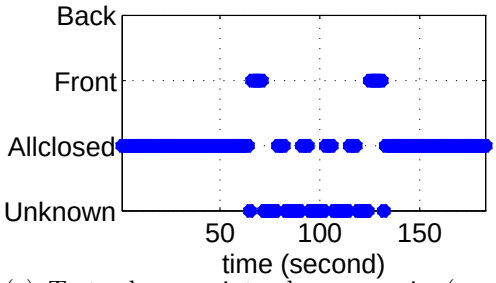

(e) Test when an intruder comes in (around the $60th$ second), walks inside, and leaves (around the $120th$ second) through front door.

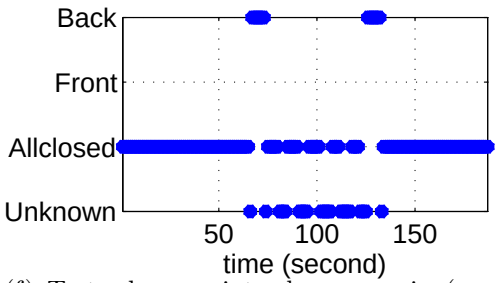

(f) Test when an intruder comes in (around the $60th$ second), walks inside, and leaves (around the $120th$ second) through back door.

Figure 4.6: System output of the proposed event detector for operational tests in House #1.

system starts to report e1 when the front door is closed at around the $30th$ second.

Figure 4.6(a), 4.6(c) and Figure 4.6(d) illustrate the ability of the proposed event detector to perfectly monitor and detect the trained events in real time when a) the environment is quiet and all doors are closed, b) the front door is opened and then closed twice from the outside, and c) the back door is opened and closed twice from the outside. In Figure 4.6(b), we simulate the postman case where someone wanders outside the front door, close to the target event. The proposed event detector shows its robustness to outside activities by reporting no false alarms in the postman case. In the next test, we simulate intrusions made by an intruder through the front door and the back door and the intruder is required to leave through the same door after walking inside the house for a certain period. As demonstrated in Figure 4.6(e) and Figure 4.6(f), the proposed event detector succeeds in capturing the intrusion. Moreover, between the door opening in both figures, the decision of the proposed event detector may become "Unknown" which is owing to the interference to the multipath channel brought by human motion inside the house.

4.3.2.3 Long-Term Test in House #1

Furthermore, we conduct a long-term monitoring test for the proposed event detector in TRIMS in House #1 for 6 days. The result is compared with that of a commercial home security system whose contact sensors are installed on the front and back door. During the first 6 days, TRIMS has 0 false alarm when the ground truth state of the indoor environment is e1. It detects with 100% accuracy over 21

times of front door opening while detects 15 out of 18 times of back door opening, i.e., an average accuracy of 92.31%.

The degradation in the accuracy is because the wireless channel keeps fading along the time while the training data for front door opening and back door opening is not updated. Hence, there eventually will be a mismatch between the testing CSI measurements and the training profiles. Considering the channel fading, the proposed event detector is designed to have an automatic updating scheme for e1, i.e., it will periodically update the training data of e1 as long as the environment is recognized as in the state of all doors closed by the event detector. The periodic refresh of e1 training metrics is to address the uncontrollable changes in the indoor environment but fails to fully resolve the problem. Due to the difficulty of labelling the testing CSI measurements from door opening in an unsupervised way, in this chapter we do not consider to update the training data for other events automatically.

4.3.2.4 Operational Test in House #2

In this part, the performance of TRIMS in real-time event monitoring is studied in House #2 with the event list being in Table 4.2. Moreover, all the parameters and hardware settings are as the same as the ones in House #1.

To begin with, the proposed event detector is set to monitor when (a) the environment is quiet and all doors are closed, (b) someone opens the front door and then closes it from the outside (twice), and (c) someone opens the back door and

State Index	Description
e1	All doors are closed.
e2	Front door open.
e3	Back door open.

Table 4.2: Events of interest in House #2.

then closes it from the outside (twice). The results are shown in Figure 4.7, where the decision output being "Unknown" means that an untrained event is happening, "Allclosed" indicates that environment is in the all-doors-closed and quiet, and "Front" and "Back" represent front door and back door is opening, respectively. All figures can be interpreted in the same way as those in Figure 4.6. The proposed event detector succeeds in capturing the trained events perfectly without false alarms.

4.3.2.5 Long-Term Test in House #2

Furthermore, the long-term behavior of the proposed event detector in TRIMS is investigated in House #2 through a test that lasts for 2 weeks. During the long-term test, resident activities are more often than that in House #1 and thus the indoor environment changes every day which might jeopardize the proposed event detector trained in day 1. Every day during the long-term test, tester performed the same operational test as in the previous part to evaluate the detection performance of the proposed event detector. The system outputs along the time are plotted in Figure 4.8, where y-axis is the system output with "unknown", "Allclosed", "Fron-

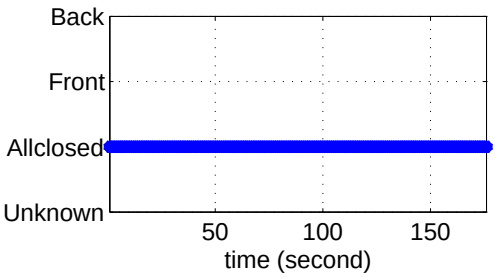

(a) Test under all doors closed.

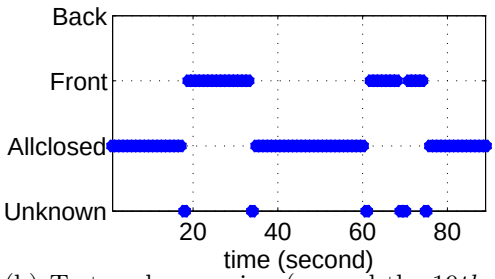

(b) Test under opening (around the 19th and the 61th second) and closing (around the 36th and the 72th second) front door from the outside the house twice.

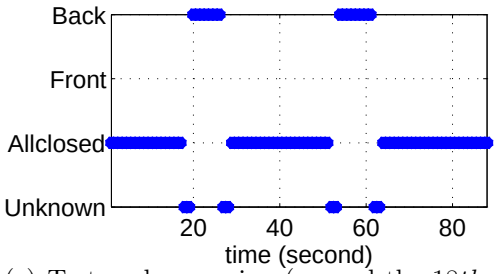

(c) Test under opening (around the 18th and the 50th second) and closing (around the 28th and the 64th second) back door from the outside the house twice.

Figure 4.7: System output of the proposed event detector for operational tests in House #2.

t" and "Back" representing the occurrence of untrained events, e1 "all doors are closed", e2 "front door is opened" and e3 "back door is opened", respectively.

As shown in Figure 4.8(a), Figure 4.8(b) and Figure 4.8(g), the proposed event detector is good at detecting the trained events with no false alarm during the same day when the system is trained. However, after 1 week or even 2 weeks, with the original training database built on day 1, the proposed system fails to detect the trained events and has a high false alarm rate on e2, as shown in Figure 4.8(l), 4.8(n), 4.8(c), 4.8(e), 4.8(h) and 4.8(j). For example, as depicted in Figure 4.8(l),

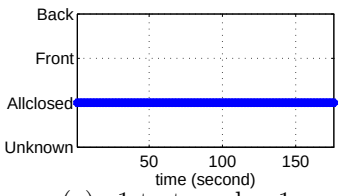

(a) e1 test on day 1.

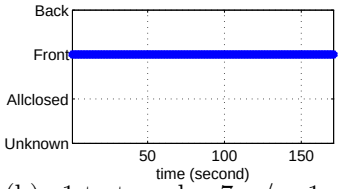

(b) e1 test on day 7 w/o e1 update.

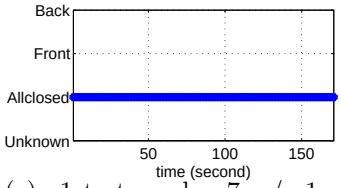

(c) e1 test on day 7 w/ e1 update.

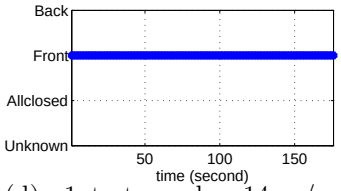

(d) e1 test on day 14 w/o e1 update.

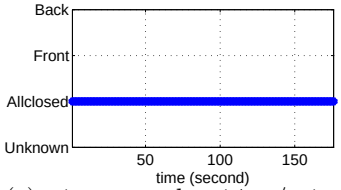

(e) e1 test on day 14 w/ e1 update.

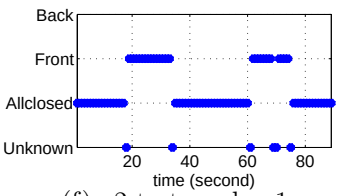

(f) e2 test on day 1.

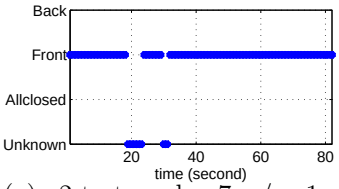

(g) e2 test on day 7 w/o e1 update.

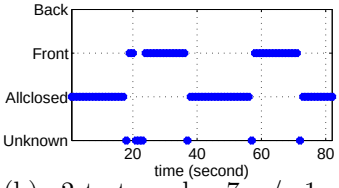

(h) e2 test on day 7 w/ e1 update.

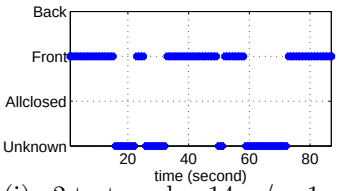

(i) e2 test on day 14 w/o e1 update.

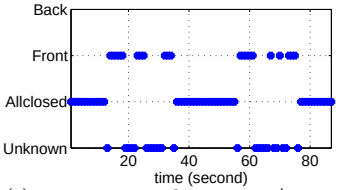

(j) e2 test on day 14 w/ e1 update.

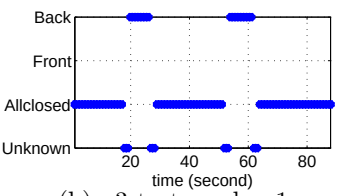

(k) e3 test on day 1.

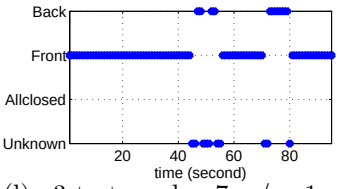

(l) e3 test on day 7 w/o e1 update.

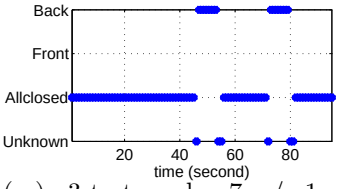

(m) e3 test on day 7 w/ e1 update.

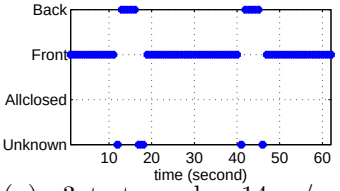

(n) e3 test on day 14 w/o e1 update.

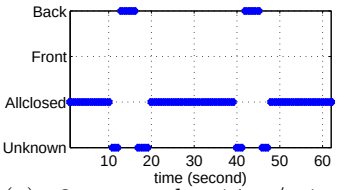

(o) e3 test on day 14 w/ e1 update.

Figure 4.8: System output of the proposed event detector for long-term tests in House #2.

the system keeps reporting "front door is opened", when the ground truth of the indoor state being e1 "all doors are closed". With uncontrolled resident activities, the indoor environment changes resulting in a different multipath profile not only for e1 but also for e2 and e3. With the help of the auto-update of e1, the proposed event detector is able to detect the trained events e2 and e3 during the 2-week experiment with no false alarm. The results are as shown in Figure 4.8(m), 4.8(o), 4.8(d), 4.8(f), 4.8(i) and 4.8(k).

As demonstrated by examples in Figure 4.8, with an automatic and periodic update of the training data for e1, TRIMS can maintain its accuracy in differentiating between and recognizing trained events in a single family house with normal resident activities during 2 weeks. The monitoring results of TRIMS in the 14-day experiment is compared with the history log provided by a commercial home security system. In general, the proposed event detector captures the incidents of e2 and e3, i.e., opening the front or the back door from the outside of the house, with an accuracy being 95.45% while a single misdetection happens on day 13.

4.3.3 TRIMS: Motion Detection Performance

The performance of the motion detector is tested in House #1 with the TX and RX devices located at positions marked by "TX_2" and "RX_2" in Figure 4.4(a). The parameter α defined in (4.24) is set to be either 0.8 or 0.2, while $W = 30$ indicates a 1-second window of continuously collected CSI as defined in (4.23). For the $D_{motion}(t_0)$ in (4.25), we apply a time-diversity smoothing with only one-level

Walking Location	Detection Rate $\alpha = 0.8$	Detection Rate $\alpha = 0.2$
Postman	0%	0%
Foyer	59.18%	12.24%
Laundry Room	100%	81.25%
Alice's Room	3.92%	0%
Study Room	1.92%	0%
Center of the house	83.33%	75.93%
Kitchen	48%	36%
Living Room	30.91%	0%
Restroom	0%	0%

Table 4.3: Detection rate for motion at different locations under 0 false alarm rate.

majority vote whose $W = 45$ and $O = 15$, to eliminate any possible false alarms due to burst noise or error in the CSI estimation.

During the training phase, the proposed motion detector learns the threshold γ_{motion} based on the data from 1-minute monitoring data collected under e1, and someone walking in and around the center of the house.

Given a zero false alarm, the detection rates of motion at different locations are listed in Table 4.3. The proposed motion detector is intelligent in that it learns and adapts its sensitivity automatically based on the characteristics of the radio

propagation environment where it is deployed, through the training phase. The change that motion introduces to the channel is proportional to the amount of the reflected signal energy that is generated by the moving object and collected at the receiver. Hence, by relying on the motion detector, TRIMS succeeds in captures motion inside the house occurring close to the devices or have a LOS path to either the TX or the RX. However, due to the large path loss for EM waves penetrating multiple walls, motion occurring inside the Alice's room or restroom will have no or tiny impacts on the CSI measurements and thus cannot trigger the motion detector. Moreover, a smaller value of α indicates the system being less sensitive and a smaller coverage of monitoring area.

4.4 Discussion

In this section, we are going to discuss some limitations of TRIMS proposed in this chapter, along with topics for further extending the proposed system.

4.4.1 Retraining TRIMS

As discussed in the long-term test in Section 4.3, the system keeps automatically and periodically updating the training data of e1, i.e., the state of that all doors are closed, based on its real-time detection results. Due to the difficulty in labelling the testing CSI of door opening in an unsupervised way, the proposed auto-updating scheme can only work for e1. As verified by experiments, with that automatic updating scheme, the proposed system is robust to normal EM perturbations introduced

by noise and slight environmental changes. However, environmental changes affect not only the CSI of state e1, but also that of event e2 and e3. If the environment changes significantly from that when e2 and e3 were trained, the proposed system would fail to find a match between the testing CSI and the one in the training database. That is when the system needs re-training, and it can be determined by comparing the very first e1 training data with the current one. Through experiments we found that when the TRRS between the earliest e1 training CSI and the current CSI measured under e1 drops below an empirical threshold of 0.7, the proposed system requires retraining over all states.

4.4.2 Monitoring with Multiple Transmitters

In current days, there are more than one device that usually connects to the same WiFi router in an office or at home, which inspires us to extend the proposed system by developing TRIMS to accommodate more transmitters. The performance of TRIMS can be improved since the information has more degrees of freedom by means of an increased spatial (device-level) diversity. Moreover, as shown in Section 4.3, for a single pair of the TX and the RX devices, it has a limited coverage in detecting events and motion. By deploying more transmitters at different locations, the monitoring area will be expanded. However, it requires further study to optimize the performance of the multi-TX TRIMS and will be one of our future work.

4.4.3 Detecting Dynamic Events

In the current event detector of TRIMS, the training database is built upon static CSI measurements collected for each events. Each dynamic event can be decomposed into several intermediate states sampled during its occurrence. Since the intermediate state can be viewed as static, the proposed algorithm can be applied to detect the occurrence of its intermediate states. Consequently, the state transition that depicts the occurrence of dynamic events can be captured, and thus dynamic events can also be monitored by the proposed system. Moreover, the authors are working on a new method for monitoring indoor dynamic events and details will be discussed in a future paper.

4.4.4 Identifying Motion

In this chapter, the proposed motion detector in TRIMS manage to detect the incidents of motion. Nevertheless, it is worthwhile to study how to utilize the TR technique to extract the characteristics of a motion with WiFi signals, e.g., the direction and the velocity. The potentiality of extracting motion information and even identifying motion with commercial WiFi devices is beneficial to various applications like elderly assistance and life monitoring.

4.4.5 Potential of TRIMS

The proposed TRIMS is not confined by WiFi and can be applied to other wireless technologies as long as CSI with enough resolution can be obtained. The

spatial resolution of CSI is determined by the transmission bandwidth of the RF device. UWB communication whose bandwidth exceeds 500MHz can provide CSI of a finer spatial resolution and enable a better discrimination than WiFi does. However, UWB-based indoor monitoring systems require to deploy specially designed RF devices and the coverage is small. On the other hand, as demonstrated by experiments, with the help of TRIMS, commercial WiFi devices with only a 40MHz bandwidth can support high-accuracy indoor monitoring. Due to the explosive popularity of wireless devices, increasing wireless traffic clogs WiFi and collisions delay the CSI probing with an unknown offset, which introduces difficulty to real-time wireless sensing systems. Taking advantage of the proposed smoothing algorithm, TRIMS is robust to non-uniform CSI probing and packages loss. Moreover, thanks to the ubiquitous deployment of WiFi, the proposed system is ready and can be easily put into practice for smart home indoor monitoring. In general, the proposed system can be integrated with all kinds of wireless technologies where CSI with enough resolution is accessible.

4.5 Summary

In this chapter, we presented a smart radio system, TRIMS, for real-time indoor monitoring, which utilizes TR technique to exploit the information in multipath propagations. Moreover, the statistical behavior of intra-class TRRS was analyzed theoretically. An event detector was built, where different indoor events are differentiated and quantitatively evaluated through TRRS statistics of the asso-

ciated CSI. Furthermore, a motion detector was designed in TRIMS to detect the existence of dynamics in the environment. The performance of TRIMS was studied through extensive experiments with TRIMS's prototype implemented on a single pair of commodity WiFi devices. Experimental results demonstrate that TRIMS addresses the problem of recognizing different indoor events in real-time. In general, TRIMS succeeds in achieving a high accuracy in long-term indoor monitoring experiments, demonstrating its prominent and promising role in future intelligent WiFi-based low-complexity smart radios.

Chapter 5

Indoor Monitoring: Training with Continuous Channel State Information

During the wireless transmission, wireless signals propagate through a multipath channel such that the received signal consists of copies of the transmitted signal reflected and scattered by different objects in the environment. When an object in the indoor environment moves, the resulted propagation path changes accordingly, leading to a new multipath profile. On the other hand, the occurrence of an indoor event consists of multiple states, each of which corresponds to a single multipath profile. In other words, the evolving of an indoor event is equivalent to a transition between multiple intermediate states, which uniquely determines the order and composition of a sequence of multipath profiles, a.k.a., the CSI. By leveraging the concept of TR space, each indoor event in the physical space is mapped into a unique trajectory of points in the TR space. Therefore, the indoor event information is embedded not only in the CSI domain but also in the temporal domain of a CSI time series.

In this chapter, we propose an indoor monitoring system that monitors the occurrence of different indoor events in real time with commercial WiFi devices. Different from the previous work proposed in Chapter 3 and Chapter 4 that only

represents each indoor event by a specific multipath profile, the proposed system in this chapter also exploits the temporal information embedded in the CSI time series. Since the occurrence of an indoor event lasts for a certain period and possesses a similar transition pattern among different realizations, information is embedded not only in each CSI sample but also in that of how CSI changes along time. Instead of treating each CSI as an independent feature, the time series of CSI samples captured continuously is used for identifying and classifying different indoor events.

The rest of this chapter is organized as follows. System model is introduced in Section 5.1. In Section 5.2, we present the detailed algorithms for the proposed system, including the feature extraction algorithm, the classification algorithm for real-time monitoring, and the proposed unsupervised retraining algorithm. The performance of the proposed system is studied and evaluated through extensive experiments in Section 5.3 and Section 5.4. This chapter is summarized and overviewed in Section 5.5.

5.1 System Model

As discussed in Section 2.1, during the wireless transmission, wireless signals propagate through a multipath channel such that the received signal consists of copies of the transmitted signal reflected and scattered by different objects in the environment. Multipaths can be viewed as virtual antennas and the CSI records the information of objects indoors. Suppose one of the virtual antenna is moving while others are static, then the corresponding CSI as defined in (2.6) can be decomposed

as

$$h_F(l,t) = \alpha_\Delta(t) e^{-j2\pi\tau_\Delta(t)\frac{l+1}{NT_s}} + \sum_k \alpha_k e^{-j2\pi\tau_k\frac{l+1}{NT_s}}, l = 0, 1, \cdots, L-1, \tag{5.1}$$

where $h_F(l,t)$ is the time-varying CFR coefficient on subcarrier l, $\alpha_\Delta(t)$ and $\tau_\Delta(t)$ denote the multipath coefficient and ToF associated to the moving antenna at current instance t.

When the virtual antenna is moving, a sequence of $(\alpha_\Delta(t), \tau_\Delta(t))$ is uniquely associated to the moving path. Hence, the CFR coefficient $h_F(l,t)$ is determined by the moving path of the virtual antenna. Let $\mathbf{h}_F(t)$ denote the CFR vector as $\mathbf{h}_F(t) = \Big[h_F(0,t), \cdots, h_F(L-1,t)\Big]$. Because each indoor event S_i involves a set of moving virtual antennas, each S_i uniquely determines a sequence of CFR $\mathbf{h}_{F,i}(t)$'s. In other words, with the help of multipath information in $\mathbf{h}_{F,i}(t)$'s, current indoor state can be deciphered by finding out which event is happening. Ultimately, changes introduced by human activities and moving objects can be extracted from the CSI and recognized through wireless sensing.

CLAIM: The trajectory of a moving virtual antenna in the physical space corresponds to a continuous logical trajectory in the TR space, represented by a time sequence of CSI.

Recall the CSI definition in (5.1) at time instance t, then we can have the CFR at time instance $t + \delta t$ $(\delta t > 0)$ as

$$h_F(l, t+\delta t) = \alpha_\Delta(t+\delta t) e^{-j2\pi\tau_\Delta(t+\delta t) f_l} + \sum_k \alpha_k e^{-j2\pi\tau_k f_l}. \tag{5.2}$$

Assuming $\alpha_\Delta(t+\delta t) = \alpha_\Delta(t)$, the difference between $h_F(l, t+\Delta t)$ and $h_F(l,t)$ on

subcarrier l becomes

$$\begin{aligned}
&\Big|h_F(l,t+\delta t)-h_F(l,t)\Big| \\
\leq&\Big|\alpha_\Delta(t)\Big|\Big|e^{-j2\pi f_l\tau_\Delta(t)}\Big(e^{-j2\pi\frac{f_l}{c}\int_t^{t+\delta t}v(u)du}-1\Big)\Big| \\
=&\Big|\alpha_\Delta(t)\Big|\Big|e^{-j2\pi\frac{f_l}{c}\int_t^{t+\delta t}v(u)du}-1\Big|,
\end{aligned} \tag{5.3}$$

where $v(u)$ is the time-varying moving speed of the moving virtual antenna with respect to the TX-RX link, $\int_t^{t+\delta t}v(u)du$ represents path length change between time interval $(t,t+\delta t)$ of the propagation path associated to the virtual antenna. Moreover, $\Big|e^{-j2\pi\frac{f_l}{c}\int_t^{t+\delta t}v(u)du}-1\Big|=0$, if and only if $\frac{f_l}{c}\int_t^{t+\delta t}v(u)du\in\mathbb{Z}$ where $\mathbb{Z}$ is the set of integer.

In other words, $\forall\epsilon>0$, $\Big|e^{-j2\pi\frac{f_l}{c}\int_t^{t+\delta t}v(u)du}-1\Big|<\epsilon/\Big|\alpha_\Delta(t)\Big|$ holds for all $\delta t\in\Big\{\delta t\mid\int_t^{t+\delta t}v(u)du=\frac{c}{f_l}k,k\in\mathbb{Z}\Big\}$. Hence, $\forall\epsilon>0$, $\exists\delta>0$ such that

$$\Big|h_F(l,t+\delta t)-h_F(l,t)\Big|<\epsilon,\text{and }\delta>\delta t, \tag{5.4}$$

which proves the continuity of $h_F(l,t)$ on t.

Therefore, when a virtual antenna is moving, the corresponding CSI changes continuously. As stated in [83, 85], each indoor location or an indoor state can be viewed as a unique point in the TR space which is represented by a multipath profile. Since each position of a moving virtual antenna uniquely determines a multipath profile (a.k.a. CFR), the moving trajectory in the physical space correspondes to a continuous logical trajectory in the TR space.

5.1.1 Multi-Antenna Diversity

MIMO transmission introduces a large number of degrees of freedom delivered through spatial diversity for RF sensing. Suppose there is a number of $|S|$ indoor events to be monitored and let $\mathbf{h}_{F,i}^{(m,n)}[k]$ denote the k^{th} complex-valued CSI vector, a.k.a., CFR, measured on the link between the m^{th} TX antenna and the n^{th} RX antenna during event $S_i \in S$. $\mathbf{h}_{F,i}^{(m,n)}[k]$ is captured at time instance kT_s, with T_s being the channel probing interval. To fully utilize the spatial diversity, we concatenate CSI vectors from different links into a single column vector as the augmented CSI by

$$\mathbf{H}_{F,i}[k] = \left[\mathbf{h}_{F,i}^{(1,1)}[k]^{\mathrm{T}}, \cdots, \mathbf{h}_{F,i}^{(N_{TX},N_{RX})}[k]^{\mathrm{T}}\right]^{\mathrm{T}}. \tag{5.5}$$

Here, $\mathbf{H}_{F,i}[k]$ is a complex-valued column vector of length $L \times N_{TX} \times N_{RX}$, L denotes the number of accessible subcarriers, and N_{TX} and N_{RX} denote the number of TX and RX antennas respectively.

A real-valued waveform vector $\mathbf{G}_i[k]$ is generated by concatenating the real and imaginary part of the obtained augmented CSI $\mathbf{H}_{F,i}[k]$, i.e.,

$$\mathbf{G}_i[k] = \left[\Re\{\mathbf{H}_{F,i}[k]^{\mathrm{T}}\}, \Im\{\mathbf{H}_{F,i}[k]^{\mathrm{T}}\}\right]^{\mathrm{T}}, \tag{5.6}$$

where $\Re\{\cdot\}$ and $\Im\{\cdot\}$ are operations to take the real and imaginary part of a complex value.

Even though information on all transmission links is included in $\mathbf{G}_i[k]$'s, the dimension of feature increases dramatically and makes the classification more difficult. In this work, we propose a feature extraction algorithm that performs refinement and dimension reduction on $\mathbf{G}_i[k]$'s.

5.2 Proposed Algorithms

In this section, the design of the proposed indoor monitoring system is presented. During the training phase, feature extraction algorithms are designed to refine the most distinct and representative sequence of CSI from the entire time series as the training template. Moreover, principle component analysis (PCA) is adopted to remove the correlation among different subcarriers and links, and to reduce the noise, in pursuit of a compact representation for training series.

Real-time monitoring faces several practical challenges, including unknown of start and end point of event occurrence, event inconsistency, accurate detection with low latency. To address those challenges, in this work, a modified classifier based on the k-nearest-neighbor (kNN) is proposed to overcome the perturbation and divergence in the real-time measurements. The similarity between training and testing feature series can evaluated through either Euclidean distance or dynamic time warping (DTW).

Long-term robustness is another challenge in real-time indoor monitoring system, due to the inevitable and unpredictable changes in the environment along the time. In this work, an automated unsupervised retraining algorithm is designed for the proposed system that guarantees high accuracy against environmental changes. The system diagram is shown in Figure 5.1 and detailed algorithms are discussed in the following.

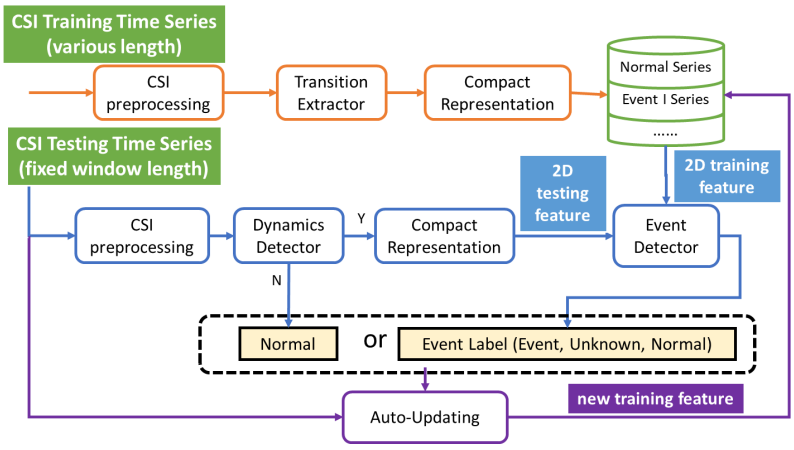

Figure 5.1: System diagram.

5.2.1 Algorithms for Feature Extraction

In this part, we introduce the proposed algorithm that refines the measured CSI time series and extracts distinct features for all indoor events of interest during the training phase.

5.2.1.1 Refinement of CSI Time Series

The essential part of the proposed algorithm is to extract the most representative segment in the CSI time series captured during the occurrence of each indoor event for building a good classifier later.

Low-Pass Filtering: CSI measurements provided directly by commercial WiFi devices are often inherently noisy, due to thermal noise, noise from analog-to-digital converters,and changes in transmit power and rates. To make the measured CSI training sequences helpful and useful in representing different indoor events, the noise must be first removed from the CSI time series. In the proposed system, a

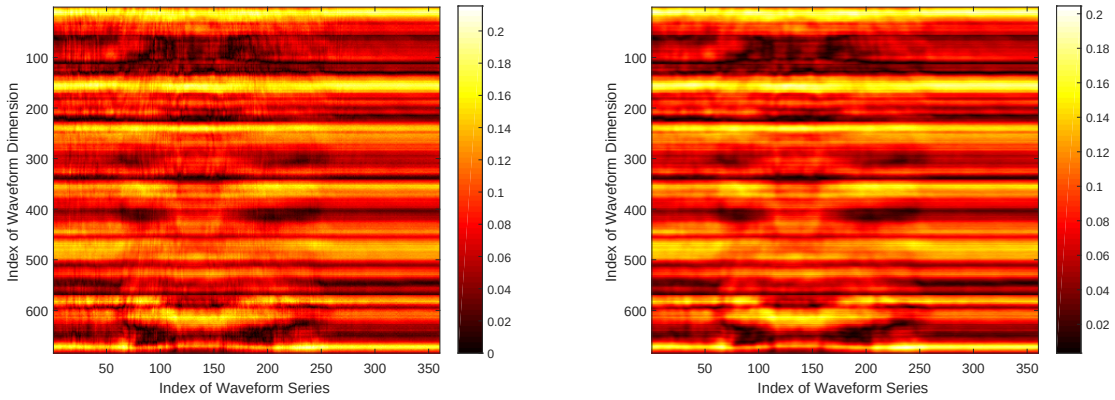

(a) Before Gaussian filtering.

(b) After Gaussian filtering.

Figure 5.2: Waveform Spectrogram: example of waveform series before and after low pass filtering.

Gaussian filter with length being $\frac{1}{3T_s}$ is applied to the waveform sequence $\mathbf{G}_i[k]$'s for each event S_i, where T_s is the channel probing interval.

An example of waveform series before and after passing through the Gaussian filter is shown in Figure 5.2, where the waveform series is measured during a door open/closed event with a sounding rate of 30 Hz. Compared with Figure 5.2(a), the waveform series in Figure 5.2(b) exhibits a much smoother transition pattern.

In the training phase the CSI time series received at the RX may capture some indoor status similar to other indoor events at the beginning and the end part of the series. Resembling CSI sub-sequences, captured from different indoor events, introduce ambiguity into pattern matching and degrade the classification performance. On the other hand, from our observation on real data and the channel model in (2.6), information among different subcarriers and links are highly correlated. Therefore, it is necessary for applying PCA over training waveform series to

generate a compact representation, given the high dimension of data. In order to learn an efficient PCA projection matrix, it is important to keep only the dynamic and distinct transition pattern of the waveform series, and discard all the static part. As shown in Figure 5.2(b), it is clear that the significant segment in $\mathbf{G}_i[k]$'s approximately starts from the 70^{th} sample to the 240^{th} sample, while others only contain useless static information.

To address that, a waveform extraction algorithm is proposed to track the change in waveform series and extract the most representative, dynamic segment. Taking into consideration that different links may capture different environmental information, the proposed waveform extraction evaluates link-wise dynamics. To do so, the waveform $\mathbf{G}_i[k]$ is first decomposed into $N_{TX} \times N_{RX}$ sequences, and can be rewritten as

$$\mathbf{G}_i[k] = \left[\mathbf{G}_i^{(1,1)}[k]^{\mathrm{T}}, \cdots, \mathbf{G}_i^{(m,n)}[k]^{\mathrm{T}}, \cdots, \mathbf{G}_i^{(N_{TX},N_{RX})}[k]^{\mathrm{T}}\right]^{\mathrm{T}},\ k = 1, 2, \cdots, M, \quad (5.7)$$

where M is the number of samples in the time series, and each $\mathbf{G}_i^{(m,n)}[k]$ is of dimension $2L \times 1$ with L being the number of accessible subcarriers on one link, given by

$$\mathbf{G}_i^{(m,n)}[k] = \left[\Re\{\mathbf{h}_{F,i}^{(m,n)}[k]^{\mathrm{T}}\},\ \Im\{\mathbf{h}_{F,i}^{(m,n)}[k]^{\mathrm{T}}\}\right]^{\mathrm{T}}. \quad (5.8)$$

Taking into consideration that due to spatial diversity, different links in a MIMO transmission may observe different multipath changes introduced by an event. Hence, the proposed feature extraction algorithm evaluate transition dynamics on each link. The details are described as in Algorithm 1. An example of applying feature extraction algorithm onto the waveform series in Figure 5.2 is shown in Figure

Algorithm 1 Waveform Extraction

Input: $\mathbf{G}_i^{(m,n)}[k],\ k = 1, 2, \cdots, M, \forall(m,n)$ captured for event S_i as defined in (5.8) after Gaussian filtering.

Output: index $k_{s,i}$ and $k_{e,i}$ s.t. $\mathbf{G}_i[k],\ k_{s,i} \leq k \leq k_{e,i}$ only contains significant variations

1: Calculate $D_\delta^{(m,n)}[k] = F\Big\{\Big|\Big(\mathbf{G}_i^{(m,n)}[k+\delta] - \mathbf{G}_i^{(m,n)}[k]\Big) \cdot /\mathbf{G}_i^{(m,n)}[k]\Big|\Big\}, k = 1, 2, \cdots, M-\delta$, with "$\cdot/$" denoting element-wise division between vectors and $F\{\cdot\}$ being the function to take median value among all elements in a vector.

2: Obtain the best link among all $(m,n) \in \{1 \leq m \leq N_{TX}, 1 \leq n \leq N_{RX}\}$ by $(m^*, n^*) = \arg\max_{(m,n)} \sum_k^{M-\delta} D_\delta^{(m,n)}[k]$.

3: $k_{s,i} = \arg\min_k \big\{k | D_\delta^{(m^*,n^*)}[k] > \gamma\big\}$ and $k_{e,i} = \arg\max_k \big\{k | D_\delta^{(m^*,n^*)}[k] > \gamma\big\}$, with an empirical threshold γ.

5.3(a), where static parts have been discarded.

5.2.1.2 Denoising and Compact Representation

Unfortunately, only applying a Gaussian filter to the incoming waveform series does not yield an effective and efficient denoising outcome. Moreover, as we discussed in the previous section, the channel information on all subcarriers are highly correlated. Based on that, we proposed to apply PCA for the purpose of noise removal, de-correlation, and dimension reduction. Also, PCA is applied to waveform vectors of all indoor events after the process in Section 5.2.1.1, in order to seek an efficient feature representation that amplifies the distinction among

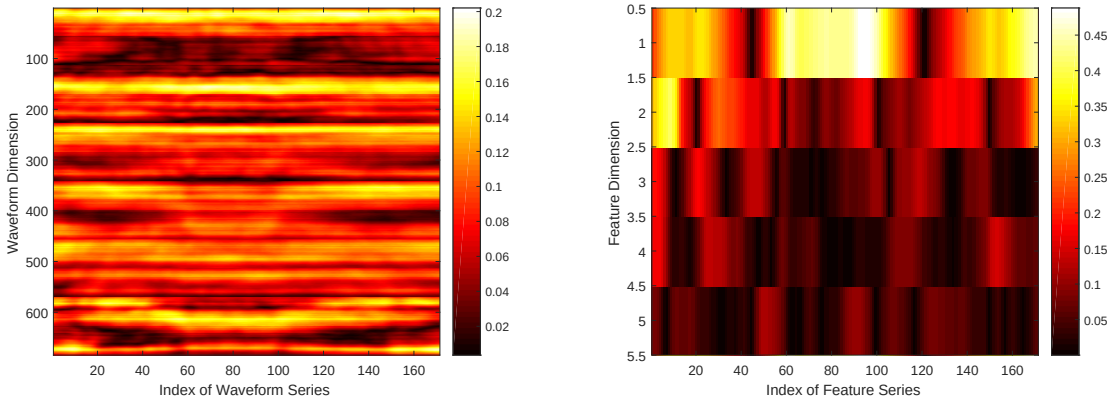

(a) Waveform series after feature extraction. (b) Feature series after PCA.

Figure 5.3: Waveform Spectrogram: example of waveform series before and after PCA.

waveforms. The details are as follows.

Let Ω_{all} denote the super waveform matrix generated by

$$\Omega_{all} = \Big[\mathbf{G}_1[k_{s,1} : k_{e,1}], \cdots, \mathbf{G}_i[k_{s,i} : k_{e,i}], \cdots, \mathbf{G}_{|S|}[k_{s,|S|} : k_{e,|S|}]\Big], \tag{5.9}$$

where $\mathbf{G}_i[k_{s,i} : k_{e,i}]$ denotes the waveform series after feature extraction for event S_i and Ω_{all} has a dimension of $2L \times K_{|S|}$. The mean waveform vector $\overline{\mathbf{G}}$ can be obtained by

$$\overline{\mathbf{G}} = \frac{1}{K_{|S|}} \sum_{k=1}^{K_{|S|}} \Omega_{all}[k]. \tag{5.10}$$

The PCA projection is learnt with the correlation matrix of $\Big(\Omega_{all}[k] - \overline{\mathbf{G}}\Big)$'s. By taking out the mean waveform $\overline{\mathbf{G}}$, we anticipate the impact of environmental background information is mitigated. Meanwhile, the projection matrix Φ of dimension $p_c \times P$ is obtained as the collection of normalized eigenvectors of the correlation matrix of $\Big(\Omega_{all}[k] - \overline{\mathbf{G}}\Big)$'s, and p_c represents the number of principle components (PCs) to be kept. In practice, the value of p_c is selected by picking the first several

largest eigenvalues that contains over 80% of the total energy among all eigenvalues. Since only the first few PCs are considered, the PCA can be computed efficiently through thin-SVD.

Then, for each event S_i, the final feature vector $\mathbf{Z}_i[k]$ can be obtained by

$$\mathbf{Z}_i[k] = \Phi \times (\mathbf{G}_i[k] - \overline{\mathbf{G}}), \forall k, \tag{5.11}$$

where the projected feature vector $\mathbf{Z}_i[k]$ is now of length p_c. An example of comparison between $\mathbf{G}_i[k]$'s and $\mathbf{Z}_i[k]$'s is plotted in Figure 5.3, where the projected feature series $\mathbf{Z}_i[k]$'s exhibits a significant variations among all PC dimensions while changes in original waveform series $\mathbf{G}_i[k]$'s is too small and too diffused to be observed.

After walking through all the preprocessing algorithms proposed in Section 5.2.1, the final feature waveform $\mathbf{Z}_i[k]$'s will be stored in the training database for all event S_i, as the reference for the real-time monitoring.

5.2.2 Algorithms for Real-Time Monitoring

In this section, we present algorithms designed for real-time monitoring phase, which addresses event inconsistency and difficulties in locating either the start or the end point of event occurrence in the incoming testing stream.

5.2.2.1 Challenges in Real-Time Monitoring

There are plenty of problems making bottlenecks in the performance of real-time wireless indoor monitoring. On one hand, considering the low latency requirement for a practical indoor monitoring system, it is hard to locate either the start

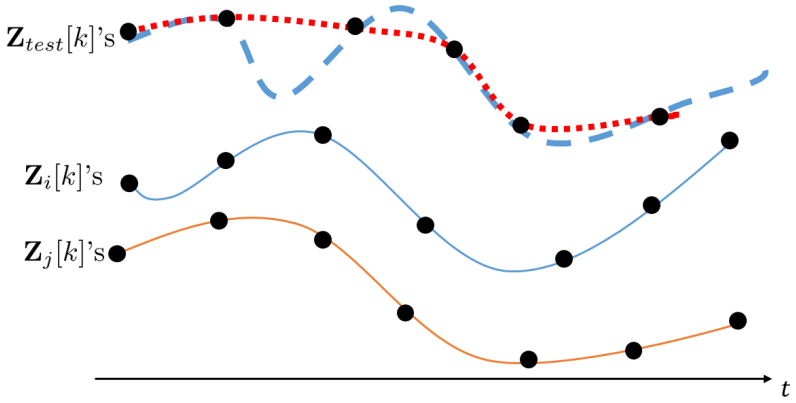

Figure 5.4: Illustration of event inconsistency.

or the end point marking an event happening in the incoming infinite testing CSI stream. The real-time indoor monitoring system should be able to detect the trained event promptly, even before the event stops. Furthermore, in the course of daily monitoring, the event occurrence may be halted due to unknown reason. Moreover, because different indoor events take distinct time to happen and evolve, the length of training feature series is different. In order to have a fair similarity comparison between the same testing series and training series with different lengths, the training feature sequences need trimming to the same length. Because the loss of information, downsampling over training sequences fails meet the requirement. Therefore, the proposed system is required to be able to perform high accuracy classification over partial training information.

On the other hand, in practical, the manner of how an event occurs and evolves will be different when performed by different individuals, resulting in a testing feature series different from the training one. Moreover, asynchronized sampling during the event occurrence that is continuous in time also leads to a altered testing feature.

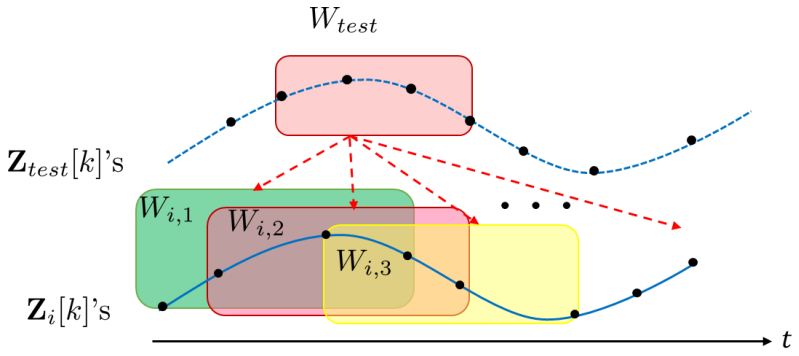

Figure 5.5: Illustration of monitoring with partial information by sliding window.

The proposed system should be capable of handling event inconsistency discussed above.

An example that illustrates event inconsistency is shown in Figure 5.4. Incoming testing series $\mathbf{Z}_{test}[k]$'s is denoted by dashed curves where sampled points are marked by black dots. The bottom two curves represent fixed-length training series $\mathbf{Z}_i[k]$'s and $\mathbf{Z}_j[k]$'s. By comparing the dashed curve with both solid curves, it is observed that $\mathbf{Z}_{test}[k]$'s contains full information of the curve denoted by $\mathbf{Z}_i[k]$'s. However, because of sampling problem, the sampled version of $\mathbf{Z}_{test}[k]$'s exhibits a pattern in red dotted curve, which is similar to $\mathbf{Z}_j[k]$'s.

5.2.2.2 Monitoring with Partial Training Information

To address the first challenge of partial information monitoring, in this work, a sliding window with length T_{win} is applied over the incoming testing stream. In practice, the window length T_{win} is selected to be 2 or 3 seconds, considering the fact that typically an indoor event last for at least 3 seconds.

As demonstrated in Figure 5.5, the incoming testing stream $\mathbf{Z}_{test}[k]$'s passes

through a sliding window and the newest sample with its $T_{win}/T_s - 1$ preceding samples form the current testing window W_{test}. Similar to that, the training series $\mathbf{Z}_i[l]$'s for every event is also partitioned into several shortened training window, denoted as $W_{i,l}$'s with $W_{i,l}$ being the l^{th} training window for training series $\mathbf{Z}_i[l]$'s. Then the similarity comparison is made between testing window W_{test} and all training windows $W_{i,l}$'s, for all i's and l's.

By applying a sliding window over income testing stream, the proposed system is able to promptly report the current indoor state. In practise, the length of the stride for sliding window, i.e., the number of antecedent feature samples to be included in W_{test} is set to be $1/T_s$ and the overlap between consecutive training window $W_{i,1}$ and $W_{i,2}$ is set to be $1/2T_s$, for the purpose of avoiding misdetection and unnecessary calculation complexity.

5.2.2.3 Similarity Comparison with Event Inconsistency

In this part, we will present how the proposed system detect current indoor state based on the information in W_{test}. The proposed system adopts a two-stage detection algorithm: (1) a dynamics detector works first over W_{test} to see if the environment is static or dynamic, (2) an event detector then works to determine which trained event occurs if the motion detector reports dynamic.

The dynamics detector measures and tracks the variations within W_{test} by

$$\beta_{test} = \sum_{k=1}^{|W_{test}|} \left\| \mathbf{Z}_{W,test}[k] - \mathbf{Z}_{W,test}[1] \right\|^2, \tag{5.12}$$

where $\mathbf{Z}_{W,test}[k]$ denotes the k^{th} sample in W_{test}, $|W_{test}|$ represents the total number

of samples in W_{test}, and β_{test} is the in-window dynamic metric. When $\beta_{test} \geq \gamma_{\text{dynamic}}$, the proposed dynamics detector considers current indoor environment to be dynamic and the event detector will respond and work.

Once the system detects dynamics in the environment, it will determine the current indoor event by comparing W_{test} with all training templates $W_{i,l}, \forall\ i\ \&\ l$. Taking into consideration of possible event inconsistency, in this work, we adopt DTW to measure the similarity between testing and training windows. As proposed in [89, 90], DTW adopts dynamic programming to obtain minimum distance alignment between two time series. The DTW distance is indeed the Euclidean distance between two time series, calculated along the optimal warping path and under the boundary conditions as well as global constraints.

In the proposed algorithm, given two sequences of feature series $\mathbf{Z}_1[l]$'s and $\mathbf{Z}_2[l]$'s with equal length L, the DTW optimal cost c is defined as the normalized distance of a warping path, i.e.,

$$c(\mathbf{Z}_1, \mathbf{Z}_2) = \frac{1}{|P^*|} \sum_{w=1}^{|P^*|} \left\| \mathbf{Z}_1[k^*_{1,w}] - \mathbf{Z}_2[k^*_{2,w}] \right\|^2, \tag{5.13}$$

where P^* denotes the optimal warping path with length $|P^*|$, and $k^*_{1,w}$ and $k^*_{2,w}$ are the indexes of $\mathbf{Z}_1[k]$'s and $\mathbf{Z}_2[k]$'s at the w^{th} point on the path P^*.

For all possible warping paths P with ($l_{1,w},\ l_{2,w}$)'s, P^* is the optimal one in that

$$\frac{1}{|P^*|} \sum_{w=1}^{|P^*|} \left\| \mathbf{Z}_1[k^*_{1,w}] - \mathbf{Z}_2[k^*_{2,w}] \right\|^2 \leq \frac{1}{|P|} \sum_{w=1}^{|P|} \left\| \mathbf{Z}_1[k_{1,w}] - \mathbf{Z}_2[k_{2,w}] \right\|^2,\ \forall P. \tag{5.14}$$

With a warping step-size $\Delta > 1$, i.e., the allowable largest stepsize for path advancing, the DTW algorithm is able to overcome issues of missing feature samples

introduced by event inconsistency and WiFi traffic collision. In addition, in the proposed algorithm, the Sakoe-Chiba Band [89] is adopted which reduces the number of searchable indexes and thus the proposed algorithm benefits from a quick and low-complexity computation of DTW.

After that, the final distance between W_{test} and all training templates $\mathbf{Z}_i$'s is defined based on (5.13) as

$$\hat{c}(W_{test}, \mathbf{Z}_i) = \min_{W_{i,l} \subseteq \mathbf{Z}_i' s} c(W_{test}, W_{i,l}). \tag{5.15}$$

With the help of DTW, a simple kNN classifier is sufficient to classify testing window W_{test}. The decision rule is as follows.

$$D_{test}(W_{test}) = \begin{cases} \arg\min\limits_{S_i \in S} \ \hat{c}(W_{test}, \mathbf{Z}_i), \ \text{if} \ \ \min\limits_{S_i \in S} \ \hat{c}(W_{test}, \mathbf{Z}_i) \leq \gamma_{event} \\ \text{Unknown, otherwise} \end{cases} \tag{5.16}$$

where γ_{event} is an empirical threshold and $D_{test}(W_{test}) = \text{Unknown}$ indicates the occurrence of an unrecognized indoor event or indoor state.

5.2.3 Algorithms for Unsupervised Retraining

Another big challenge for real-time wireless indoor monitoring is unpredictable and inevitable changes in the indoor propagation environment. Due to normal human activities inside the monitored areas and channel fading, the estimated multi-path CSI keeps changing along the time and it may result in mismatch between testing and training feature series. It is crucial to design a real-time indoor monitoring system that can adapt itself to environment changes and maintain its performance in long-term. In this section, we propose an unsupervised automatic retraining al-

gorithm that keeps update the training database of the proposed system on the fly. The proposed algorithm contains two part: (1) retraining for static environment and (2) retraining for dynamic events. The details are as follows.

1. *Retraining for static environment*: Feature sequence from static environment can be easily and reliably labelled through the proposed dynamic detector. Hence, in the proposed system, the training series $\mathbf{Z}_i[l]$'s that represent a static environment is periodically updated with the testing series W_{test} which is classified as a static state by the proposed system. In order to guarantee the robustness of retraining for static state, a boundary condition is set for the candidate feature series W_{test} to be qualified in that the decision outputs before and after W_{test} must be static consistently for a certain period (e.g., one hour).

2. *Retraining for dynamic events*: The unsupervised retraining procedure for trained dynamic events is much more complicated. The criterion to select a qualified testing series as a new training series for an event can either be too loose which may introduce more false alarms to the system, or be too strict which may reject all possible candidates and make the proposed system incapable of self adapting to environmental changes. In the proposed system, the retraining for dynamic events works under the following protocols as listed in Algorithm 2.

During the monitoring phase, whenever the system detects the current indoor states to be a trained events and the distance score $\hat{c}(W_{test}, \mathbf{Z}_{D_{test}}) \leq \gamma_{un}$, the corresponding testing series W_{test} will be stored temporarily in a buffer W_{buffer} and the system decision is put into D_{prev}. Subsequent W_{test}'s will be concatenated into the same buffer W_{buffer} with repeated feature samples being discarded, if their

decision D_{test} is as same as D_{prev} and the distance score satisfies $\hat{c}(W_{test}, \mathbf{Z}_{D_{test}}) \leq \gamma_{un}$. When the current D_{test} is different from D_{prev} or $\hat{c}(W_{test}, \mathbf{Z}_{D_{test}}) \geq \gamma_{un}$, the stored testing features in W_{buffer} will be filtered and the length of it is examined before putting it into the training dataset as a new training sequence $\widehat{W}$ for event D_{test}. Lastly, the buffer W_{buffer} is reset and ready for the next coming testing series. In Algorithm 2, γ_{un} is an empirical threshold, chosen to satisfy $\gamma_{un} \leq \gamma_{event}$ such that the confidence of testing samples in W_{buffer} belonging to event D_{test} is guaranteed. Moreover, as the system works along the time, the number of training series for an event grows. Hence, the proposed system keeps forgetting the oldest training series for each event obtained from Algorithm 2 when the total number of training series for that event exceeds a predefined capacity.

5.3 Experimental Results

To evaluate the performance of the proposed algorithms, extensive experiments have been conducted to protect a multi-room office from intrusion in various setting. In this work, we use door open/closed event monitoring as an example to illustrate the performance of the proposed algorithms. The proposed real-time indoor monitoring system can be extended to other applications. Moreover, contact sensors as well as a video recording system provide the ground truth in the experiments.

Algorithm 2 Unsupervised retraining for dynamic events.

Input: Incoming testing stream $\mathbf{Z}_{W,test}[k]$'s as in W_{test}, D_{test} for W_{test} using (5.16).

Output: Candidate training series $\widehat{W}$.

Initiate $W_{\text{buffer}} \leftarrow$ empty matrix of $p_c \times 0$.

$W_{\text{buffer}} \leftarrow \mathbf{Z}_{W,test}[k]$, if $\hat{c}(W_{test}, \mathbf{Z}_{D_{test}}) \leq \gamma_{un}$.

while TRUE do

    $D_{prev} \leftarrow D_{test}$.

    $W_{test} \leftarrow$ new testing features $\mathbf{Z}_{W,test}[k]$'s.

    Obtain D_{test} for current W_{test} based on (5.16).

    if $D_{prev} == D_{test}$ and $D_{test} \in S$ and $\hat{c}(W_{test}, \mathbf{Z}_{D_{test}}) \leq \gamma_{un}$ **then**

        $W_{\text{buffer}} \leftarrow$ concatenate W_{buffer} and $\mathbf{Z}_{W,test}[k]$'s with repeated testing feature vectors discarded.

    else

        if W_{buffer} is not empty **then**

            $W_{\text{buffer}} \leftarrow$ feature extraction over Gaussian filtered W_{buffer}.

            if $|W_{\text{buffer}}| \geq |W_{test}|$ **then**

                $\widehat{W} \leftarrow W_{\text{buffer}}$ for event D_{test} and is put into training database.

            $W_{\text{buffer}} \leftarrow$ empty matrix of $p_c \times 0$.

5.3.1 Experimental Setting

A prototype of the proposed indoor monitoring system is implemented using a pair of commercial WiFi devices, which performs 2×3 MIMO transmission with the carrier frequency being 5.8GHz and under a 40MHz bandwidth. The sounding

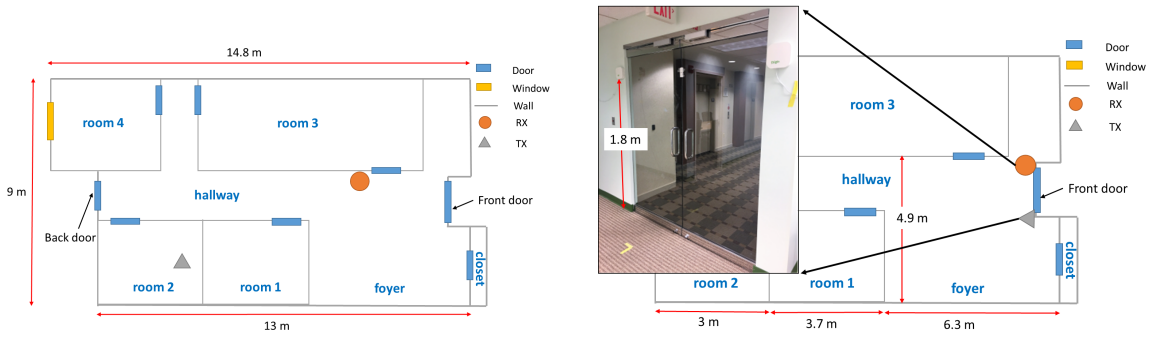

(a) Setting 1. (b) Setting 2.

Figure 5.6: Experimental setting: floorplans.

rate $1/Ts$ is 30 Hz.

The experiments are carried out in the offices at the 10^{th} floor in a commercial building of 16 floors in total. The experimental offices are surrounded by multiple offices and elevators as discussed before in Section 3.2.1. The experimental setting is shown in the floorplans in Figure 5.6. The location of the TX and RX are marked in Figure 5.6. In setting 1 the system is aimed to monitoring both front door and back door opening event, while the system only monitors the front door in setting 2. The window length $|W_{test}|$ is set to be $3/T_s$, representing a window of 3 seconds.

We divide the experiment into two parts. First, the robustness of the proposed system is evaluated under the existence of event inconsistency (Section 5.3.2), the existence of outdoor activities (Section 5.3.3), and the existence of indoor activities (Section 5.3.4). Then, the performance of the proposed system in long-term test is studied in an experiment lasting for 32 days.

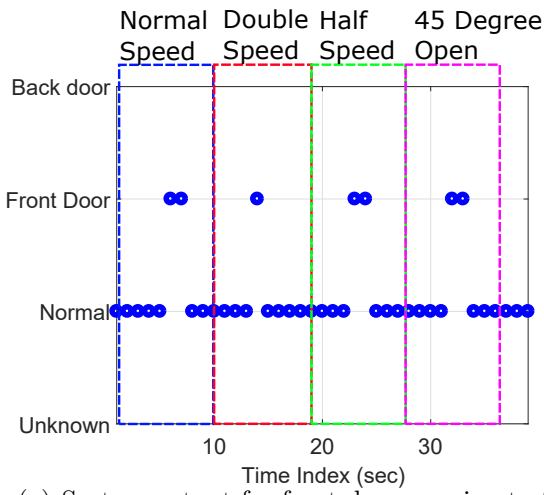

(a) System output for front door opening test.

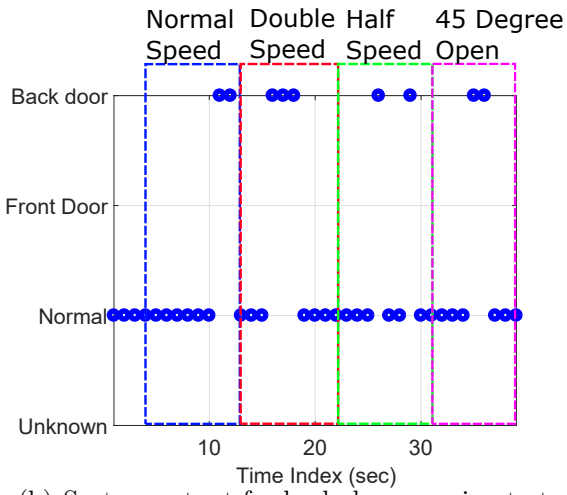

(b) System output for back door opening test.

Figure 5.7: Experimental results: robustness to event inconsistency in setting 1.

5.3.2 Robustness to Event Inconsistency

In this part, we deploy the system in setting 1 (as shown in Figure 5.6(a)) and in the training phase, one trainer performs door opening event from door close to door 90 degree open, at both the front door and the back door once with a normal speed. Then, in the testing phase, the tester, other that the trainer, intentionally introduces event inconsistency, by performing door opening event at the same training speed, twice of the training speed, and half of the training speed. Moreover, the tester also performs door opening event at the same training speed, but pauses at a 45 degree. The system output is shown in Figure 5.7, where the x-axis is the time index in seconds and the y-axis is the event name.

From Figure 5.7, we have the following observations.

- When the speed to perform door opening is slow, the proposed system sometime may consider the current environment as static.

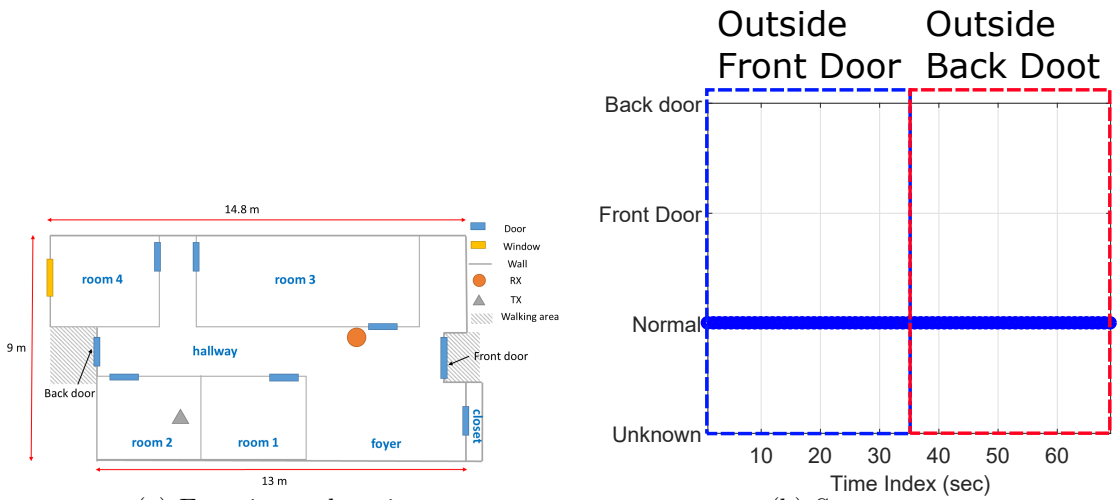

(a) Experimental setting.

(b) System output.

Figure 5.8: Experimental results: robustness to outside activities (Experiment 1).

- By leveraging DTW, the proposed system can handle difference in training and testing speed.

- With the help of sliding window, the proposed system can detect indoor state with partial training information. Hence, even when the door opening process is paused at half open which is the middle point of the training series, the proposed system can still reliably and promptly detect the occurrence of event.

In general, the proposed system is robust to event inconsistency.

5.3.3 Robustness to Outside Activities

In this part, we conduct experiments to evaluate how system respond to outside activities. The experimental setting is shown in Figure 5.8(a) and Figure 5.9(a), where the tester is random walking in the shaded area close to the target event.

According to the system outputs of both experiments plotted along the time

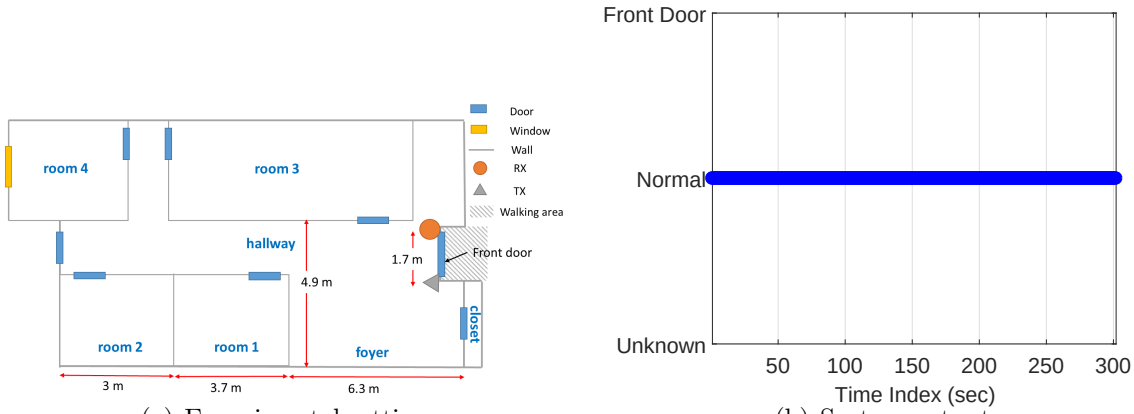

(a) Experimental setting. (b) System output.

Figure 5.9: Experimental results: robustness to outside activities (Experiment 2).

in Figure 5.8(b) and Figure 5.9(b), the proposed real-time indoor monitoring system is insusceptible to activities outside the monitoring area.

5.3.4 Robustness to Inside Activities

Because of the limited amount of multipath leakage to the outside of monitoring area, the proposed real-time indoor monitoring system is robust to outside activities. However, as most of the multipaths concentrate inside the monitoring area and especially around the TX/RX device, inside activities perturb the measured multipath CSI and may introduce a lot of false alarms, posing a great challenge to the wireless monitoring. In this part, we conduct three sets of experiments to test the robustness of the proposed system to inside activities. In Scenario 1 whose setting is shown in Figure 5.10(a), one tester is asked to walk randomly in the foyer or along the hallway while the system is trained with front and back door opening events. From the system output plotted in Figure 5.10(b), no false alarm is triggered

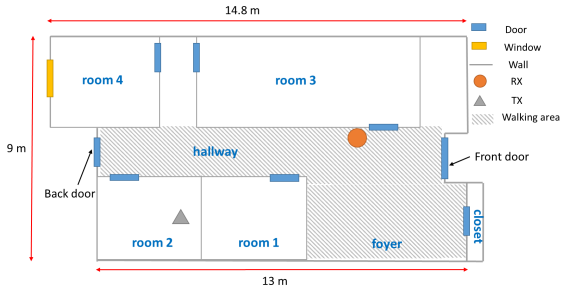

(a) Experimental setting 1.

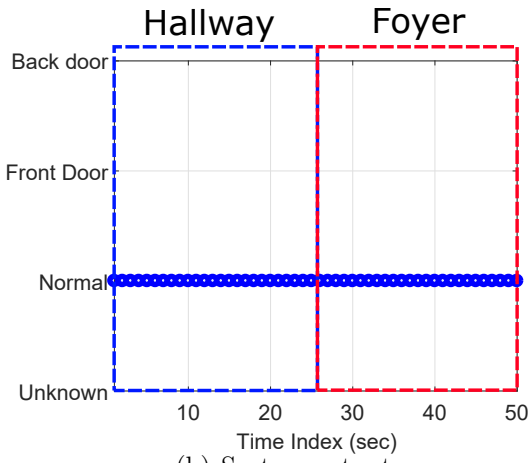

(b) System output.

Figure 5.10: Experimental results: robustness to inside activities (Scenario 1).

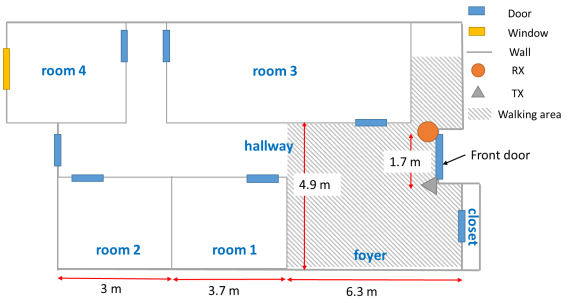

(a) Experimental setting 2.

(b) System output.

Figure 5.11: Experimental results: robustness to inside activities (Scenario 2).

and the system works correctly along the time.

Then the system is deployed under the setting 2 and is trained to monitoring the front door opening events. We start with Scenario 2 where one and two testers are asked to walk randomly in the shaded area, close to the trained event and the TX/RX. In this 6 minutes test, the system output, as shown in Figure 5.11(b), is correct no matter how many people is walking inside the monitoring area.

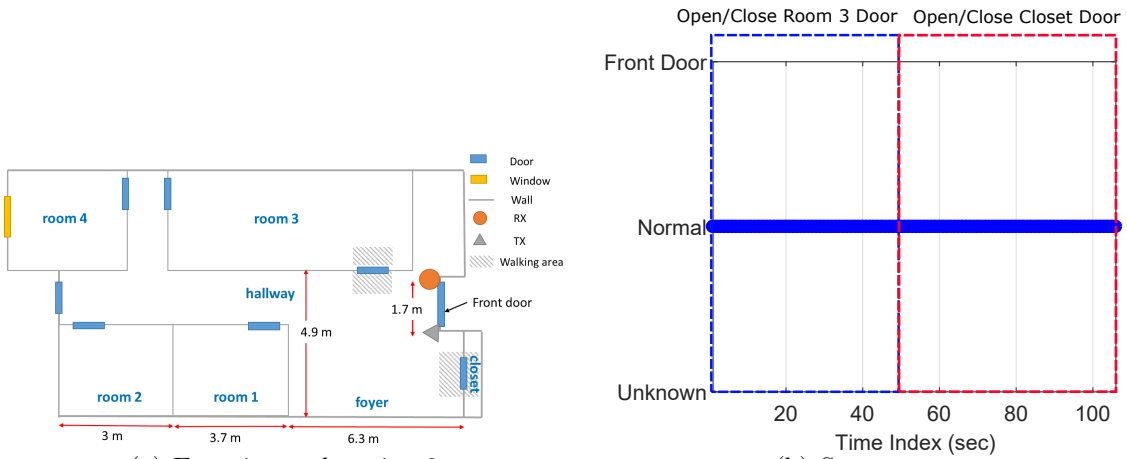

(a) Experimental setting 3.

(b) System output.

Figure 5.12: Experimental results: robustness to inside activities (Scenario 3).

Besides the human walking test in Figure 5.11, we also perform door opening tests to see whether a similar but untrained event will introduce false alarms to the proposed system. In Scenario 3, one tester is asked to open and close the room 3 door and closet door 4 times, respectively. The experiment setting of Scenario 3 is shown in Figure 5.12(a).

Based on the experimental experiments in this part, we can conclude that the proposed real-time monitoring system guarantee its robustness to various indoor activities.

5.3.5 Long-Term Performance

To evaluate the long-term performance and the unsupervised retraining algorithms of the proposed system, the prototype is deployed in setting 2 for 32 days without human intervention. The system is aimed to protect the front door and only gets trained once on the first day. The front door is the major entrance for the

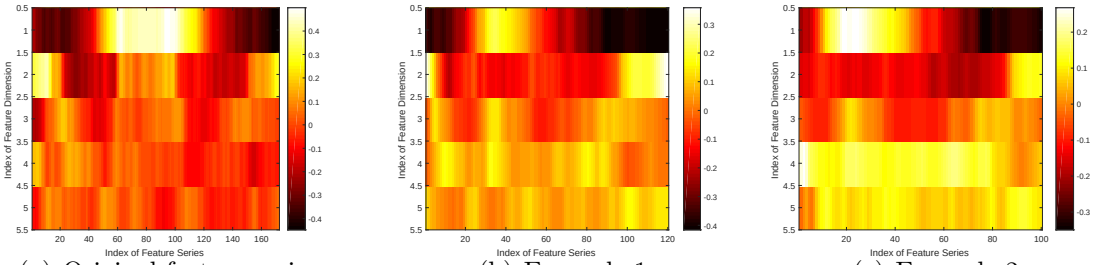

(a) Original feature series. (b) Example 1. (c) Example 2.

Figure 5.13: Examples of feature series generated by Algorithm 2.

Total Duration of Monitoring (seconds)	1,968,420
Total Number of Event Occurrence	2085
Number of Detected Event Occurrence	2078
Detection Accuracy	99.66%
Number of False Alarm (seconds)	17

Table 5.1: Long-term test results.

entire office area which is occupied by over 12 people. Moreover, during the testing, normal work day activities happen inside the testing area and the furniture inside the foyer and room 3 gets moved from time to time. The result is summarized in Table 5.1.

According to the results listed in Table 5.1, the proposed system succeeds in maintaining a high accuracy of trained event detection with the help of the proposed automatic unsupervised training algorithm. To the best of our knowledge, this work is the first real-time indoor monitoring system performing fine-grained event

detection that has been tested in a busy office environment for over one month without human intervention.

During the 32-day experiments, the front door opening event has been updated for 475 times in an unsupervised manner, while the latest 19 and the original one are kept in the database. Examples of new training feature series obtained from unsupervised retraining during the long-term test are shown in Figure 5.13. Although same trend exhibits in those three sequences, the new feature series in either Figure 5.13(b) or 5.13(c) is slightly different from the original training series in Figure 5.13(a) captured at the initialization.

5.4 Discussion

In this section, we will study the impact of length of sliding window W_{test} and the proposed unsupervised retraining algorithm. Moreover, we will demonstrate how the proposed system can be utilized for future smart home or smart office applications.

5.4.1 Impact of Sliding Window Length

In this part, experiments in Section 5.3.4 are repeated to study how different lengths of W_{test} will affect system performance. The false alarm rate is studied based on different window length $|W_{test}|$, and the result is plotted in Figure 5.14 for setting 1 and setting 2.

According the result in Figure 5.14, for both settings, the false alarm rate

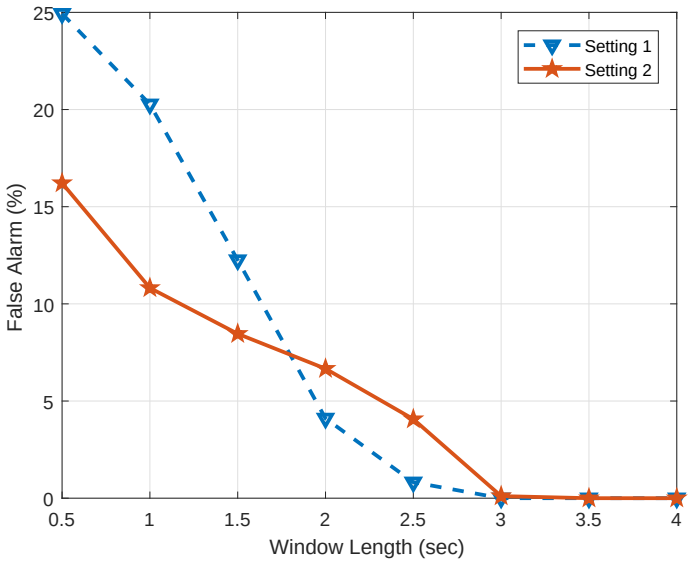

Figure 5.14: Experimental results: impact of sliding window length.

increases dramatically as the window length $|W_{test}|$ decreases. That is because the distinctive information of events is embedded not only in each CSI sample but also in the transition information of the CSI time sequence. As we increase the window length $|W_{test}|$, more environmental information in the CSI is included for event recognition. Although two events may share resembling individual CSI samples, the associated CSI time sequence should be differentiable. Hence, as more information is included as the representative pattern, a higher detection accuracy can be achieved and fewer false alarms will be triggered by nearby human interference. On the other hand, with a larger $|W_{test}|$, the system latency increases which is undesirable for real-time system. Hence, in order to guarantee the performance of the proposed system, the window length $|W_{test}|$ should be carefully selected.

Total Duration of Monitoring (seconds)	1,968,420
Total Number of Event Occurrence	2085
Number of Detected Event Occurrence	1844
Detection Accuracy	88.44%
Number of False Alarm (seconds)	2

Table 5.2: Long-term test result without unsupervised retraining for dynamic events.

5.4.2 Impact of Unsupervised Retraining

In this part, the long-term system performance with and without the proposed unsupervised retraining algorithms is compared and discussed. The result without unsupervised retraining for dynamic events is summarized in Table 5.2.

Comparing Table 5.2 and Table 5.1, the proposed unsupervised retraining algorithm helps to maintain the detection performance in long term when the background environment changes along the time. Without the proposed unsupervised retraining, the detection rate drops from 99.66% to 88.44%. However, because of the nature of unsupervised labelling, the candidate training series extracted from testing CSI stream may introduce slight false alarms coming from the interference of human activities happening before or after the trained events. Overall, the proposed system equipped with the automatic unsupervised retraining scheme is promising for real-time indoor monitoring applications.

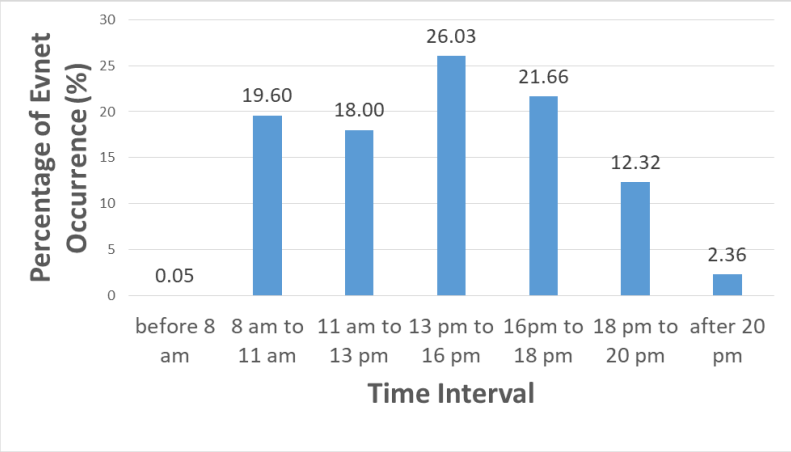

Table 5.3: Smart office analysis.

5.4.3 Potential for Smart Home

In this part, we discuss how the proposed real-time indoor monitoring system can be deployed in future smart home/office. By performing analytics over the monitoring results generated by the proposed system, we can analyze human behaviors happened in the protected area and get the following chart as shown in Table 5.3.

Table 5.3 indicates active and inactive hours of the office area where the long-term experiment is conducted. That measured human behavioral information can incorporate with applications like smart air conditioner, smart lights and other smart devices, to create a smart office environment, which is energy efficient and user-friendly.

5.5 Summary

In this chapter, we proposed a real-time indoor event monitoring system that utilizes CSI time series to differentiate between indoor states. A feature extraction

algorithm was designed to extract and refine a low-dimensional feature from measured CFR sequences. To address practical issues of real-time monitoring, e.g., event inconsistency and unknown start and end point in the incoming testing stream, we proposed a sliding window based classification algorithm with the help of DTW to measure the similarity between training and testing features. Moreover, an automatic unsupervised retraining algorithm was designed to improve the system performance in long-time monitoring. Extensive experiments were conducted to demonstrate the potential of the proposed system in future real-time indoor monitoring applications.

Chapter 6

Radio Biometrics: Human Recognition Through a Wall

Nowadays, the capability of performing reliable human identification and recognition has become a crucial requirement in many applications, such as forensics, airport custom check, and bank securities. Current state-of-the-art techniques for human identification rely on the discriminative physiological and behavioral characteristics of human, known as biometrics.

Biometric recognition refers to the automated recognition of individuals based on their human biological and behavioral characteristics [91, 92]. The well-known biometrics for human recognition include fingerprint, face, iris, and voice. Since biometrics are inherent and distinctive to an individual, biometric traits are widely used in surveillance systems for human identification. Moreover, due to the difficulty for biometrics counterfeit, techniques based on the biometrics have clear-cut advantages over traditional security methods such as passwords and signatures in countering the growing security threats and in facilitating personalization and convenience. Even though the current biometrics systems are accurate and can be applied in all environments, all of them require special devices that capture human biometric traits in an extremely LOS environment, i.e., the subject should make contact with the devices.

Another category of biometrics is gait analysis and it relies on the individual walking pattern to distinguish between different identities. Conventional gait recognition requires high-speed cameras, wearable sensors and floor sensors [93]. Recently, gait recognition has been extended to RF platform where the Doppler shift or the time-of-fligh (ToF) of the signal reflected by human body is used to extract individual gait pattern [34, 94, 95]. However, to get a high-resolution gait profile, it relies on special devices to scan over ultra-wide spectrum and LOS transmission is often required to guarantee the accuracy of gait extraction. Moreover, the computational complexity introduced by the necessary image processing and machine learning algorithms for gait recognition is high. Unlike the aforementioned system, in this work, a novel concept of radio biometrics is proposed, and accurate human identifications and verifications can be implemented with commercial WiFi devices in a through-the-wall setting.

In [96], researchers studied the relationship between the EM absorption of human bodies and the human physical characteristics in the carrier frequency range of 1 to 15 GHz, in which the body's surface area is found to have a dominant effect on absorption. Moreover, the interaction of EM waves with biological tissue was studied [97] and the dielectric properties of biological tissues were measured in [98, 99]. According to the literature, the wireless propagation around the human body highly depends on the physical characteristic (e.g., height and mass), the total body water volume, the skin condition and other biological tissues. The human-affected wireless signal under attenuations and alterations, containing the identity information, is defined as *human radio biometrics*. Considering the combination of all the

physical characteristics and other biological features that affect the propagation of EM waves around the human body and how variable those features can be among different individuals, the chance for two humans to have the identical combinations is significantly small, no matter how similar those features are. Even if two have the same height, weight, clothing and gender, other inherent biological characteristics may be different, resulting in different wireless propagation patterns round the human body. Take the DNA sequence as an example. Even though all humans are 99.5% similar to any other humans, no two humans are genetically identical which is the key to techniques such as genetic fingerprinting [100]. Since the probability of two individuals to have exactly the same physical and biological characteristics is extremely small, the multipath profiles after human interferences are therefore different among different persons. Consequently, human radio biometrics, which record how the wireless signal interacts with a human body, are altered accordingly to individuals' biological and physical characteristics and can be viewed as unique among different individuals. One example is that the face recognition has been implemented for many years to distinguish from and recognize different people, thanks to the fact that different individuals have different facial features. Human radio biometrics, which record how RF signals respond to the entire body of a human, should contain more information than a face, and thus become more distinct among humans.

In this chapter, we show the existence of human radio biometrics and present a human identification system that can discriminate individuals even through the walls in a NLOS condition. Using commodity WiFi devices, the proposed system

captures the CSI and extracts human radio biometric information from WiFi signals using TR technique. This procedure is called *radio shot*. By leveraging the fact that broadband wireless CSI has a significant number of multipaths, which can be altered by human body interferences, the proposed system can recognize individuals, utilizing not only the face, but also the entire individual physical characteristic profiles.

- We introduce for the first time the concept of human radio biometrics, which account for the wireless signal attenuation and alteration brought by human. Through experiments, its existence has been verified and its ability for human identification has been illustrated. The procedure to collect human radio biometrics is named as radio shot.

- Due to the fact that the dominant component in the CSI comes from the static environment rather than human body, the human radio biometrics are embedded and buried in the multipath CSI. To boost the identification performance, we design novel algorithms for extracting individual human radio biometrics from the wireless channel information.

- Radio biometrics extracted from the raw CSI are complex-valued and high-dimensional, which complicates the classification problem. To address this problem, we apply the TR technique to fuse and compress the human radio biometrics and to differentiate between radio biometrics of different people, by using the strength of the spatial-temporal resonances.

- For performance evaluation, we build the first prototype that implements the

TR human identification system using off-the-shelf WiFi chipsets, and test in an indoor office environment during normal working hours.

The rest of this chapter is organized as follows. We introduce the theoretical foundation of the proposed system and define the human radio biometrics in Section 6.1. Section 6.2 presents the proposed novel algorithms for extracting individual human radio biometrics from the wireless channel information and the human recognition method using TR technique. The performance of the proposed system is studied and evaluated through extensive experiments with results being presented in Section 6.3. We briefly discuss the limitation of the proposed system and compare it with the RSSI based approach in Section 6.4. This chapter is concluded in Section 6.5.

6.1 System Model

The proposed system is built upon the fact that the wireless multipath comes from the environment where the EM signals undergo different reflecting and scattering paths and delays. According to the literature, the wireless propagation around the human body highly depends on the physical characteristic (e.g., height and mass), the total body water volume, the skin condition and other biological tissues. Since it is rare for two individuals to have exactly the same biological physical characteristics, the multipath profiles after human interferences are therefore different among different persons. The human radio biometrics, which record how the wireless signal interacts with a human body, is altered accordingly to individuals' biological

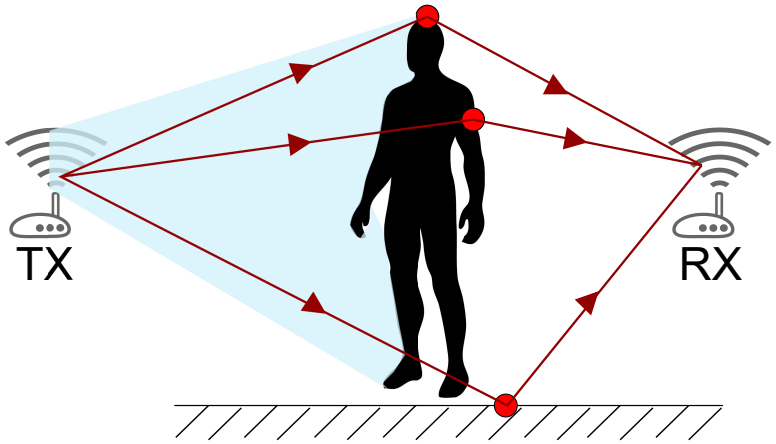

Figure 6.1: RF reflections and scattering.

physical characteristics and can be viewed as unique among different individuals. Through WiFi sounding, the wireless CSI is collected, as well as the human radio biometrics.

Mathematically, the indoor CSI (a.k.a. Channel frequency response, CFR) for the m^{th} link with the presence of human body can be modeled as the sum of the common CSI component and the human affected component:

$$\mathbf{h}_{F,i}^{(m)} = \mathbf{h}_{F,0}^{(m)} + \delta\mathbf{h}_{F,i}^{(m)}, \quad i = 1, 2, \cdots, N, \tag{6.1}$$

where N is the number of individuals to be identified. $\mathbf{h}_{F,i}^{(m)}$ is a $L \times 1$ complex-valued vector, which denotes the CSI when the i^{th} individual is inside. L is the number of subcarriers, i.e., the length of the CSI. $\mathbf{h}_{F,0}^{(m)}$, defined as the static CSI component, is generated from the static environment in the absence of human, and $\delta\mathbf{h}_{F,i}^{(m)}$ denotes the perturbation in the CSI introduced by the i^{th} individual. Here, the $\delta\mathbf{h}_{F,i}^{(m)}$ is the raw human radio biometric information of the i^{th} individual embedding in the CSI of the m^{th} link.

At the receiver side, after each channel state sounding, we can collect a $L \times M$ raw CSI matrix for each individual as

$$\mathbf{H}_{F,i} = [\mathbf{h}_{F,i}^{(1)},\ \mathbf{h}_{F,i}^{(2)},\ \cdots,\ \mathbf{h}_{F,i}^{(M)}],\ \forall\ i, \tag{6.2}$$

with the corresponding human radio biometric information matrix being

$$\delta\mathbf{H}_{F,i} = [\delta\mathbf{h}_{F,i}^{(1)},\ \delta\mathbf{h}_{F,i}^{(2)},\ \cdots,\ \delta\mathbf{h}_{F,i}^{(M)}],\ \forall\ i, \tag{6.3}$$

where M is the number of links between the transmitter and the receiver.

At this point, for human identification and recognition, there are two major problems:

1. both $\delta\mathbf{H}_{F,i}$ and $\mathbf{H}_{F,i}$ are $L \times M$ complex-valued matrix. Without appropriate data processing, the classification problem based on the raw data is complex-valued and of high computation complexity.

2. Since we have no idea of what $\mathbf{h}_{F,0}^{(m)}$ is, it is hard to extract the buried biometric information $\delta\mathbf{H}_{F,i}$ directly from the CSI measurement $\mathbf{H}_{F,i}$. Moreover, the embedded human radio biometric information $\delta\mathbf{H}$ is small compared with other CSI components in measurement $\mathbf{H}$. In order to improve the identification performance, we need to remove the common components from each CSI measurement, and to extract and refine the embedded human biometrics features after taking the radio shot.

To tackle the first problem, we incorporate the TR technique to reduce the data dimension by quantifying the similarity between two measurements using TR

spatial-temporal resonance. Specifically, for two CSI measurements $\mathbf{H}_{F,i}$ and $\mathbf{H}_{F,j}$ obtained through a MIMO transmission, we can obtain a $1 \times M$ TRRS vector as

$$[\mathcal{TR}(\mathbf{h}_{F,i}^{(1)}, \mathbf{h}_{F,j}^{(1)}),\ \mathcal{TR}(\mathbf{h}_{F,i}^{(2)}, \mathbf{h}_{F,j}^{(2)}),\ \cdots,\ \mathcal{TR}(\mathbf{h}_{F,i}^{(M)}, \mathbf{h}_{F,j}^{(M)})], \tag{6.4}$$

where $\mathcal{TR}(\mathbf{h}_{F,i}^{(2)}, \mathbf{h}_{F,j}^{(2)})$ is calculated using (2.7). Then, the TRRS between $\mathbf{H}_{F,i}$ and $\mathbf{H}_{F,j}$ is defined as the average of the TRRSs on each of the links,

$$\mathcal{TR}(\mathbf{H}_{F,i}, \mathbf{H}_{F,j}) = \frac{1}{M} \sum_{m=1}^{M} \mathcal{TR}(\mathbf{h}_{F,i}^{(m)}, \mathbf{h}_{F,j}^{(m)}). \tag{6.5}$$

Furthermore, for the second problem, data post-processing algorithms are proposed to refine the human radio biometrics from the raw CSI information as discussed in Section 6.2.

We show an example of the TRRS matrices of each link for different CSI measurements captured by our prototype in Figure 6.2. Due to the different spatial distributions of each link, how the human body affects the CSI of each link varies. Some link succeeds in capturing the human biometric information and shows distinct TRRSs between different individuals as in Figure 6.2(c). Whereas, some link fails and the TRRSs between test subjects are similar as shown in Figure 6.2(e).

6.2 Radio Biometric Refinement Algorithms

Consider the simplified example in Figure 6.1. In an indoor wireless signal propagation environment, the human body acts as a reflector and the red dots represent the reflecting and scattering point due to the human body and other objects. Since the wireless signal reaches the receiving antenna from more than

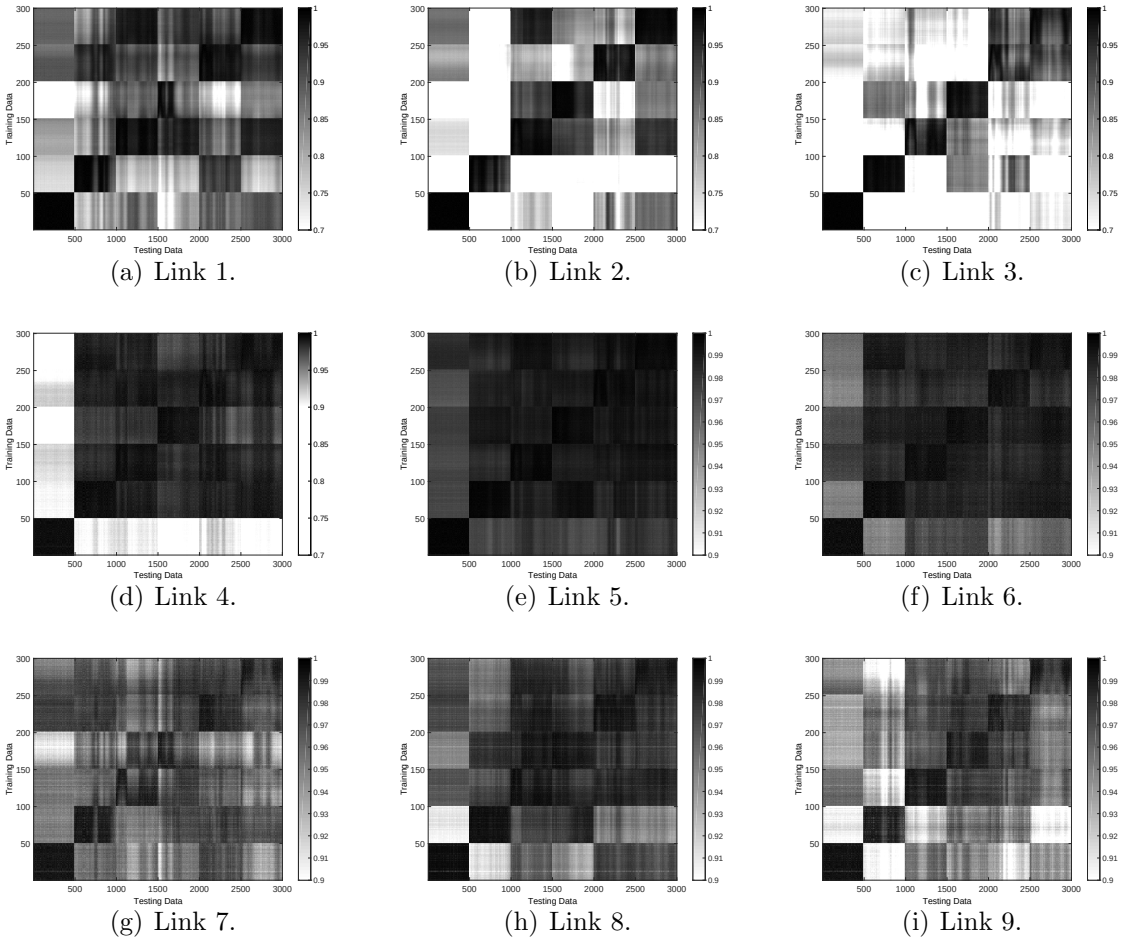

(a) Link 1. (b) Link 2. (c) Link 3.

(d) Link 4. (e) Link 5. (f) Link 6.

(g) Link 7. (h) Link 8. (i) Link 9.

Figure 6.2: TRRS map for each link.

one path, the human radio biometrics are implicitly embedded in the multipath CSI profile. However, the human body may only introduce a few paths to the multipath CSI, and the energy of those paths is small due to the low reflectivity and permittivity, compared with other static objects such as the walls and furniture. As a result, the human radio biometrics, captured through radio shot, are buried by other useless components in the CSI. Without a refinement of the radio biometric information, the common feature $\mathbf{h}_{F,0}^{(m)}$ in the CSI dominates in the TRRS in (6.4).

To address the above problem, we propose several post-processing algorithms

to extract the human radio biometrics and magnify the difference among individuals. Specifically, we develop a background subtraction algorithm such that the common information in the CSI can be removed and the distinctive human radio biometrics are preserved. By leveraging the TR technique, the human radio biometrics in the form of complex-valued matrices are related to the corresponding individual through a real-valued scalar, the TRRS.

The design of the proposed time reversal human identification system exploits the above idea and is made up of two key components:

- *Human radio biometrics refinement:* This module extracts the human biometric information from the raw CSI measurement which is a 9×114 complex-valued matrix. Due to the independency of each link, the background for each link should be calculated and compensated individually. An important consideration is that, for each CSI measurement, it may be corrupted by the SFO and the STO. Hence, before background calculation and compensation, the phase of each CSI measurement should be aligned first. After alignment, based on the assumption that the human radio biometrics only contribute small changes in the multipath, the background can be obtained by taking the average of several CSI measurements.

- *TR-based identification:* Once the 9×114 complex-valued human radio biometric information is refined, this component simplifies the identification problem by reducing the high-dimension complex-valued feature into a real-valued scalar. By leveraging the TR technique, the human radio biometrics are

mapped into the TR space and the TRRS quantifies the differences between different radio biometrics.

6.2.1 Phase Alignment Algorithm

Considering the phase errors, each CSI $\mathbf{h}_F^{(m)}$ can be mathematically modeled as:

$$\mathbf{h}_F^{(m)}[l] = \left|\mathbf{h}_F^{(m)}[l]\right| \exp\Big\{ - j(k\phi_{linear} + \phi_{ini})\Big\}, l = 0, 1, \cdots, L-1, \tag{6.6}$$

where ϕ_{linear} denotes the slope of the linear phase. ϕ_{ini} is the initial phase, and both of them are different for each CSI.

Unfortunately, there is no way to explicitly estimate either ϕ_{linear} or ϕ_{ini}. To address the phase misalignment among the CSI measurements, for each identification task, we pick one CSI measurement in the training database as the reference and align all the other CSI measurements based on this reference.

To begin with, we find the linear phase difference $\delta\phi_{linear}$ between the reference and other CSI samples. For any given CSI $\mathbf{h}_{F,2}$ with the reference $\mathbf{h}_1$ from the same link, we can have

$$\delta\phi_{linear} = arg\max_{\phi} \Big| \sum_{l} \mathbf{h}_{F,1}[l]\mathbf{h}_{F,2}^{*}[l] \exp\Big\{jl\phi\Big\}\Big|. \tag{6.7}$$

To align the linear phase of the CSI $\mathbf{h}_{F,2}$ according to the reference, we simply compensate for this difference on each subcarrier through

$$\widehat{\mathbf{h}}_{F,2}[k] = \mathbf{h}_{F,2}[k] \exp\Big\{ - jk\delta\phi_{linear}\Big\},\ k = 0,\ 1,\ \cdots, L-1. \tag{6.8}$$

Once upon all the linear phase differences of the CSI measurements have been compensated based on the reference, the next step is to cancel the initial phase of

the CSI for each link, including the reference. The initial phase is obtained as the phase on the first subcarrier for each CSI $\angle\widehat{\mathbf{h}}_F[0]$, and can be compensated as

$$\mathbf{h}_{align} = \widehat{\mathbf{h}}_F \exp\Big\{ - j\angle\widehat{\mathbf{h}}_F[0]\Big\}. \tag{6.9}$$

In the following discussion, both the background and the refined human biometric information are extracted from the aligned CSI measurements $\mathbf{h}_{align}$. To simplify notation, we will use $\mathbf{h}_F$ instead of $\mathbf{h}_{align}$ to denote the aligned CSI in the rest of this chapter.

6.2.2 Background Subtraction Algorithm

In the proposed CSI model in (6.1), the radio biometrics $\delta\mathbf{h}_{F,i}^{(m)}$ also involves two parts: the common radio biometric information and the distinct radio biometric information. Thus, $\mathbf{h}_{F,i}^{(m)}$ can be further decomposed as following:

$$\mathbf{h}_{F,i}^{(m)} = \mathbf{h}_{F,0}^{(m)} + \delta\mathbf{h}_{F,i,ic}^{(m)} + \delta\mathbf{h}_{F,i,c}^{(m)}, \quad \forall i, m, \tag{6.10}$$

where $\delta\mathbf{h}_{F,i}^{(m)} = \delta\mathbf{h}_{F,i,c}^{(m)} + \delta\mathbf{h}_{F,i,ic}^{(m)}$. $\delta\mathbf{h}_{F,i,c}^{(m)}$ denotes the common radio biometric information, which is determined by all the participants in the identification system. Meanwhile, $\delta\mathbf{h}_{F,i,ic}^{(m)}$ is the corresponding distinct radio biometric information, remaining in the extracted radio biometrics after taking out the common biometric information.

The background CSI components for several CSI measurements of N individuals can be estimated by taking the average over the aligned CSI as:

$$\mathbf{h}_{bg}^{(m)} = \frac{1}{N}\sum_{i=1}^{N} \frac{\mathbf{h}_{F,i}^{(m)}}{\left\|\mathbf{h}_{F,i}^{(m)}\right\|^2}. \tag{6.11}$$

Then the human radio biometrics for each individual can be extracted through subtracting a scaled version of the background in (6.11) from the original CSI.

$$\widetilde{\mathbf{h}}_{F,i}^{(m)} = \mathbf{h}_{F,i}^{(m)} - \alpha \mathbf{h}_{bg}^{(m)}, \tag{6.12}$$

where α is the the background subtraction factor, $0 \leq \alpha \leq 1$. It can not be too close to 1 as the remaining CSI will be noise-like. The impact of α is studied in Section 6.3.2.

After obtaining the refined radio biometrics $\widetilde{\mathbf{h}}_i^{(m)}$ for each link, the classification problem based on the TRRS in (6.15) becomes:

$$\hat{i} = \begin{cases} arg\max_i \mathcal{TR}(\widetilde{\mathbf{H}}_F, \widetilde{\mathbf{H}}_{F,i}), \text{ if } \max_i \mathcal{TR}(\widetilde{\mathbf{H}}_F, \widetilde{\mathbf{H}}_{F,i}) \geq \mu, \\ 0, \qquad otherwise, \end{cases} \tag{6.13}$$

where $\widetilde{\mathbf{H}}_i$ is the refined radio biometric information matrix for individual i and

$$\widetilde{\mathbf{H}}_{F,i} = [\widetilde{\mathbf{h}}_{F,i}^{(1)}, \ \widetilde{\mathbf{h}}_{F,i}^{(2)}, \ \cdots, \ \widetilde{\mathbf{h}}_{F,i}^{(M)}], \ \forall \ i. \tag{6.14}$$

$\widetilde{\mathbf{H}}_{F,i}$ is an approximation of the distinctive component in the human radio biometric information matrix $\delta\mathbf{H}_{F,i}$ defined in (6.3).

An example is shown in Figure 6.3, where the TRRS $\mathcal{TR}(\mathbf{H}_F, \mathbf{H}_{F,i})$ before background subtraction is plotted in Figure 6.3(a) while that of $\mathcal{TR}(\widetilde{\mathbf{H}}_F, \widetilde{\mathbf{H}}_{F,i})$ is in Figure 6.3(b), with the background as the average of all CSI measurements in training database. The comparison between two figures demonstrates that the refinement of human radio biometrics helps to improve the sensitivity of TRRS for differentiating between individuals. The proposed background subtraction algorithm suppresses the spatial-temporal resonance of the CSI between different classes while maintaining strong resonance within the same class.

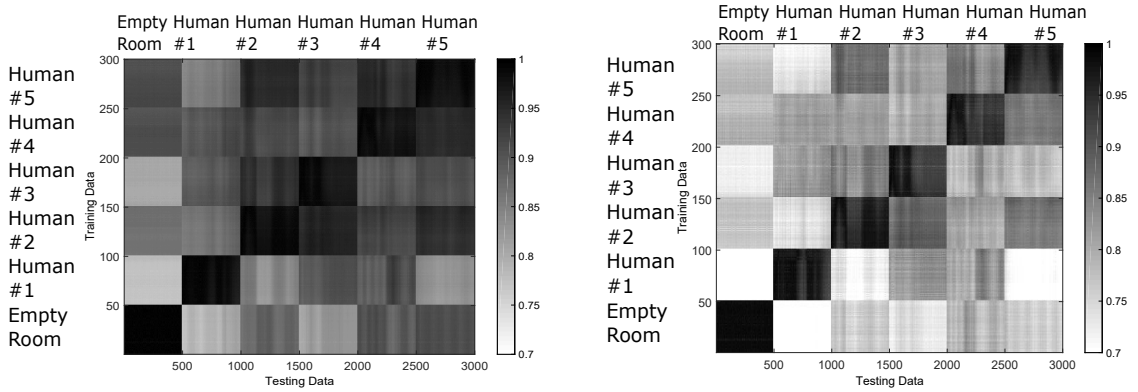

(a) No background subtraction. (b) After background subtraction with $\alpha = 0.5$.

Figure 6.3: Comparison on TRRS maps with and without background subtraction.

For the proposed system, if there are K subjects to be identified, the computational complexities for building the training database and testing are both $O(M \times (K+1) \times N\log_2 N)$, where M is the number of either the training CSI samples or the testing CSI samples for each subject. N is the search resolution for ϕ in (6.7), where typical values for N are 512 and 1024.

In the following discussion, to simplify notation, we will use $\mathbf{H}_{F,i}$ instead of $\widetilde{\mathbf{H}}_{F,i}$) to denote the refined CSI samples, a.k.a. the distinctive component in the human radio biometric information, in the rest of this chapter.

6.2.3 Identification Methodology

After taking the radio shot, by means of the TR signal processing, the high-dimension complex-valued human radio biometrics embedded in the CSI measurements are mapped into the TR space, and the feature dimension is reduced from $L \times M$ to 1. The human recognition problem can be implemented as a simple multi-class classification problem as following.

For any radio biometric measurement $\mathbf{H}_F$, given a training database consisting of the radio biometric samples of each individual $\mathbf{H}_{F,i},\ \forall\, i$, the predicted individual identity (ID) is obtained based on the TRRS as:

$$\hat{i} = \begin{cases} arg\max_i \mathcal{TR}(\mathbf{H}_F, \mathbf{H}_{F,i}), & \text{if } \max_i \mathcal{TR}(\mathbf{H}_F, \mathbf{H}_{F,i}) \geq \mu, \\ 0, & otherwise, \end{cases} \tag{6.15}$$

where $\mathcal{TR}(\mathbf{H}_F, \mathbf{H}_{F,i})$ is calculated using (6.5) with refined biometric measurement, μ is a predefined threshold for triggering the identification, and $\hat{i} = 0$ denotes an unidentified individual.

6.3 Experimental Results

By leveraging the TR technique to capture human radio biometrics embedded in the CSI of WiFi signals, the proposed system is capable of identifying different individuals in real office environments with high accuracy. In this section, the performance of human identification is evaluated. For the proposed system, the training, i.e., taking the radio shot, is simple and can be done in seconds.

6.3.1 Experimental Setting

The evaluation experiments are conducted in the office at the 10^{th} floor of a commercial office building with a total of 16 floors. The floorplan of the experiment office is shown in Figure 6.4(a). Surrounding the experiment area, there are 4 elevators and multiple occupied rooms. All the experiments are conducted during the normal working hours in weekdays, so that outside the experiment office there

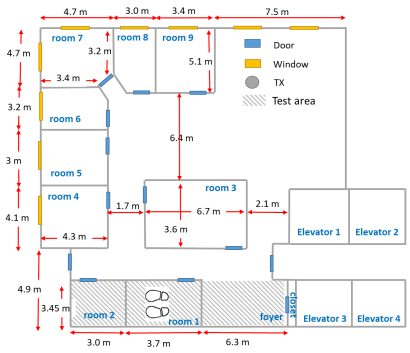

(a) Indoor experiment floorplan with dimensions.

(b) Transmitter or receiver devices.

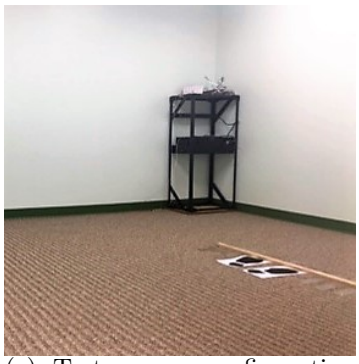

(c) Test room configuration (room 1).

Figure 6.4: Experiment setting: floorplan and device.

Test Subject	**♯1**	**♯2**	**♯3**	**♯4**	**♯5**	**♯6**	**♯7**	**♯8**	**♯9**	**♯10**	**♯11**
Height (cm)	172	164	173	168	176	170	170	172	180	166	155
Weight (kg)	74	53	70	90	90	90	70	69	75	68	45
Gender (M/F)	M	F	M	M	M	M	F	M	M	M	F
Glasses (Y/N)	Y	N	Y	Y	Y	Y	N	Y	Y	Y	N

Table 6.1: Physical characteristics of test subjects in human identification experiment.

are many activities, such as human walking and elevator running, happening at the same time as the experiments run. In Figure 6.4 the experiment configurations of the transmitter, the receiver and individuals are demonstrated. Both WiFi devices are placed on the cart or table with height from the ground being 2.8ft as shown in Figure 6.4(b). When taking the radio shot, each individual, to be recognized, stands in the center of the room 1, as marked by the footprint.

Furthermore, in the experiments, we build the training database with 50 CSI measurements for each class, while the size of the testing database for identification is 500 CSI measurements per class. The physical characteristics of test subjects are listed in Table 6.1. The first five subjects participate in experiments in Section 6.3.2 and Section 6.3.3, while all the 11 subjects take part in the identification experiment in Section 6.3.4. The 2^{nd} individual is the subject in the verification experiments in Section 6.3.5.

6.3.2 Study on Background Subtraction

To begin with, we first quantitatively study the impact of the proposed background subtraction and biometrics refinement algorithms on human recognition. The experiment setup is shown in Figure 6.5. When the transmitter (bot) is on location denoted as "A", the receiver (RX) is placed on the locations denoted from "Loc 1" to "Loc 5". Otherwise when the bot is on location "B", the receiver is on "Loc 6" to "Loc 10" respectively. These 10 TX-RX locations can represent LOS scenario ("Loc 1"), NLOS scenarios ("Loc 2" to "Loc 6"), and through-the-wall scenarios ("Loc 7" to "Loc 10").

As shown by Figure 6.3, after refinement the spatial-temporal resonance between the training and the testing CSI from different classes is suppressed a lot while maintaining a high TRRS for the CSI from the same class. In Table 6.2, the performance matrices for human identification are listed to show the performance improvement after refining the radio biometrics. Each element of the performance

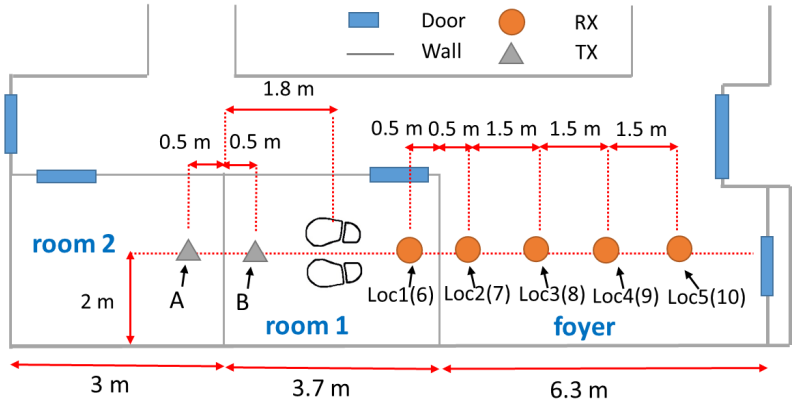

Figure 6.5: Experiment setting for background subtraction study.

(a) No background subtraction.

Training Data \ Testing Data	Empty room	Human #1	Human #2	Human #3	Human #4	Human #5
Empty room	1	0	0	0	0	0
Human #1	0	0.9812	0	0	0	0
Human #2	0	0	0.9972	0.0024	0	0
Human #3	0	0	0	0.9635	0	0
Human #4	0	0	0	0	0.9696	0
Human #5	0	0	0.0011	0	0	0.9842

(b) After background subtraction with $\alpha = 0.5$.

Training Data \ Testing Data	Empty room	Human #1	Human #2	Human #3	Human #4	Human #5
Empty room	1	0	0	0	0	0
Human #1	0	0.9812	0	0	0	0
Human #2	0	0	0.9972	0.0024	0	0
Human #3	0	0	0	0.9635	0	0
Human #4	0	0	0	0	0.9696	0
Human #5	0	0	0.0011	0	0	0.9842

Table 6.2: Performance matrix of individual identification with and without background subtraction.

matrix is the probability for that the TRRS between the training and the testing classes is higher than the threshold μ. A higher value in the diagonal means a larger chance of correct identifications. However, larger off-diagonal elements indicate higher false alarm rates because it implies that the testing sample may be misclassified to the wrong training class with a higher probability if the testing class has never been included in the training set.

Both of the matrices in Table 6.2 have the same threshold $\mu = 0.9$ as defined in (6.15) and (6.13). Without background subtraction, although the diagonal value can reach 100%, the off-diagonal ones can be as high as 99.99% as shown in Table 6.1(a). A high off-diagonal value implies a larger chance to have a false alarm between these particular training and testing classes. Nevertheless, after background subtraction, when using the refined radio biometrics for identification, the largest off-diagonal value drops to 0.24% while maintaining the diagonal elements higher than 96.35%.

6.3.2.1 Background Selection

How to choose the background CSI components is essential for a good radio biometrics refinement. In this part, we study the performance of identification under three schemes: no background subtraction, subtraction with the static environment background, subtraction with the background consisting of static environment and common radio biometrics. We compare the ROC curves in Figure 6.6. The ROC curves, which are obtained by averaging the ROC performance measured at all 10 TX-RX locations, show how the identification rate and false alarm rate vary as the decision threshold μ changes. The red dashed line denotes the performance when using all the CSI measurements in training data set as the background (i.e., the background consisting of static environment and common radio biometrics), while the blue solid line and green dotted line represent the case of no background subtraction and subtraction with the static environment background, respectively. Here, the background subtraction factor is $\alpha = 0.5$. The performance of the system

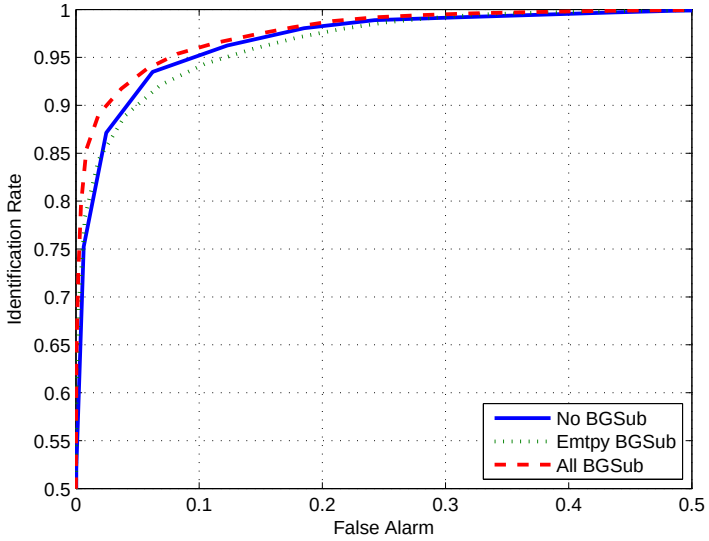

Figure 6.6: Evaluation on ROC curves for background selection.

using all the training CSI measurements outperforms the others. The reason is that, by taking the average of the CSI samples from all the classes as the background, we effectively eliminate the high correlated and similar component in radio biometrics for different individuals, which is the estimation of $\mathbf{h}_{F,0}^{(m)} + \delta\mathbf{h}_{F,i,c}^{(m)}$ as defined in (6.10), and thus enlarge the difference between the radio biometrics of different people.

6.3.2.2 Background Subtraction Factor

After we have determined the optimal background, the next question is to find the optimal background subtraction factor α. In Figure 6.7, the ROC performance is plotted to evaluate the impact of different α, considering and averaging over all TX-RX locations. When $\alpha = 0.9$, the identification performance is the worst because the remaining CSI components after background subtraction is noisy and has few information for human biometrics. Through the experiment, we find $\alpha = 0.5$ is

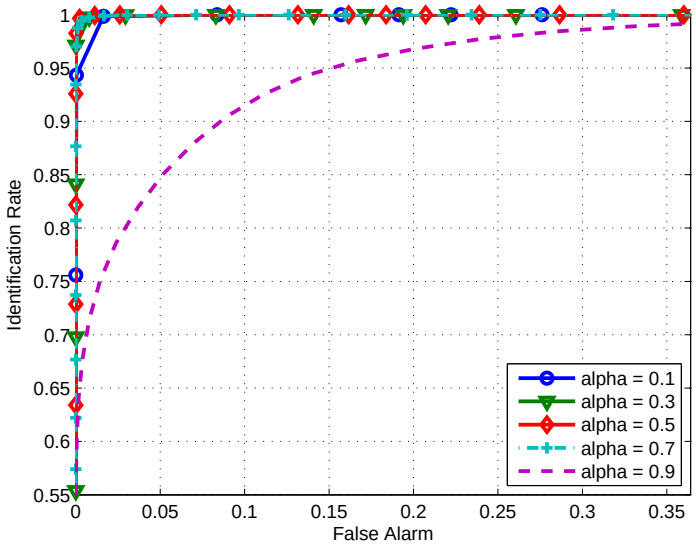

Figure 6.7: Evaluation on ROC curves for background subtraction factor.

optimal for individual identification. In the rest experiments, we adopt $\alpha = 0.5$ and the all-CSI background scheme.

6.3.3 Study on TX-RX Locations

Next, we would like to evaluate the impacts of TX-RX configurations on the performance of human identification. "Loc 1" represents LOS scenario where the transmitter, receiver and experiment individual are in the same room. "Loc 2" to "Loc 6" represent the NLOS case where either the transmitter or the receiver is in the same room with the individual, while the other device is placed outside. Moreover, in the through-the-wall scenarios, represented by "Loc 7" to "Loc 10", the individual to be identified is in the room while both the transmitter and the receiver are outside and in different locations.

The identification performance of different scenarios is plotted in Figure 6.8.

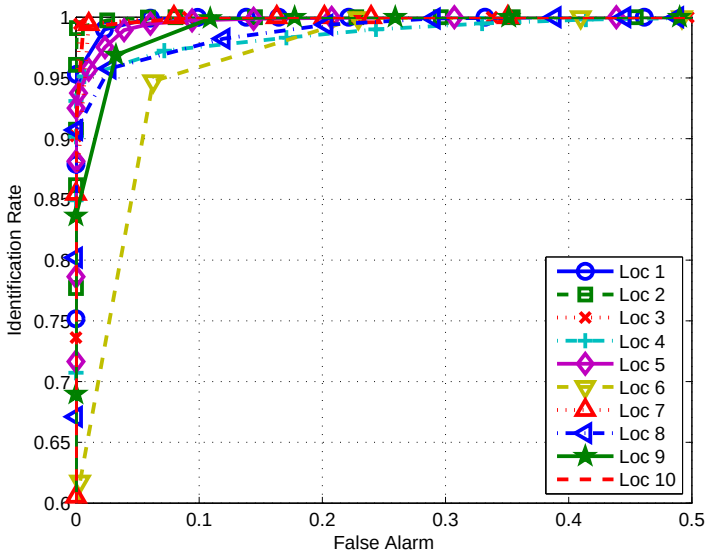

Figure 6.8: Evaluation on ROC curves for different TX-RX locations.

The performance comparison can be summarized from the best to the worst as: Loc 7 > Loc 2 > Loc 3 > Loc 10 > Loc 1 >Loc 5 > Loc 9 > Loc 4 > Loc 8 > Loc 6. There is no direct relation between identification performance and the distance between the transmitter and the receiver. Moreover, the LOS scenario is not the best configuration for human identification. As we discussed, the human radio biometrics are embedded in the multipath CSI. Due to the independency of each paths in the multipath CSI, the more paths the CSI contains, the larger number of degrees of freedom it can provide in the embedded human radio biometrics. Consequently, owing to the fact that there are fewer multipath components in the CSI of the LOS scenario, less informative radio biometrics are extracted, which degrades the performance of identification. The results in Figure 6.8 also demonstrate the capability of the proposed system for through-the-wall human identification, in that no matter which configuration is selected the proposed system has a high accuracy.

(a) Loc 1.

Training Data \ Testing Data	Empty room	Human #1	Human #2	Human #3	Human #4	Human #5
Empty room	1	0	0	0	0	0
Human #1	0	0.9762	0	0	0	0
Human #2	0	0	0.9887	0	0	0
Human #3	0	0	0	0.9272	0	0
Human #4	0	0	0	0	0.9306	0
Human #5	0	0	0	0	0	0.5159

(b) Loc 6.

Training Data \ Testing Data	Empty room	Human #1	Human #2	Human #3	Human #4	Human #5
Empty room	1	0	0	0	0	0
Human #1	0	0.9896	0	0	0.0912	0
Human #2	0	0	0.9836	0.8820	0.7128	0.1296
Human #3	0	0	0.9732	0.9969	0.2052	0.3014
Human #4	0	0	0.1190	0	1	0.0174
Human #5	0	0	0.1426	0.3633	0	0.9991

(c) Loc 7.

Training Data \ Testing Data	Empty room	Human #1	Human #2	Human #3	Human #4	Human #5
Empty room	1	0	0	0	0	0
Human #1	0	0.9812	0	0	0	0
Human #2	0	0	0.9972	0.0024	0	0
Human #3	0	0	0	0.9635	0	0
Human #4	0	0	0	0	0.9696	0
Human #5	0	0	0.0011	0	0	0.9842

Table 6.3: Comparison on performance matrices with fixed threshold $\mu = 0.9$.

(a) Loc 1.

Training Data \ Testing Data	Empty room	Human #1	Human #2	Human #3	Human #4	Human #5
Empty room	1	0	0	0	0	0
Human #1	0	1	0	0	0	0.0430
Human #2	0	0	1	0.6678	0	0
Human #3	0	0	0.9190	0.9997	0	0
Human #4	0	0	0	0.0004	1	0
Human #5	0	0.1564	0	0	0	0.9977

(b) Loc 6.

Training Data \ Testing Data	Empty room	Human #1	Human #2	Human #3	Human #4	Human #5
Empty room	1	0	0	0	0	0
Human #1	0	0.9972	0	0	0.4843	0
Human #2	0	0	0.9956	0.9753	0.8852	0.3906
Human #3	0	0	0.9947	0.9990	0.3744	0.6113
Human #4	0	0.0110	0.5126	0.0130	1	0.0771
Human #5	0	0	0.5020	0.6238	0.0048	0.9999

(c) Loc 7.

Training Data \ Testing Data	Empty room	Human #1	Human #2	Human #3	Human #4	Human #5
Empty room	1	0	0	0	0	0
Human #1	0	0.9966	0	0	0	0
Human #2	0	0	0.9995	0.0443	0	0.0005
Human #3	0	0	0	0.9905	0	0
Human #4	0	0	0	0	0.9936	0
Human #5	0	0	0.0248	0	0	0.9984

Table 6.4: Comparison on performance matrices with the minimum diagonal element larger than 99%.

6.3.3.1 Special Case Study

To better understand the impact of TX-RX locations on the identification capability of the proposed system, six examples are investigated and compared in Table 6.3 by using the performance matrices defined at the beginning of Section 6.3.2.

In Table 6.2(a), 6.2(b) and 6.2(c), the performance matrices for LOS case "Loc 1", NLOS case "Loc 6" and the through-the-wall case "Loc 7" with the threshold $\mu = 0.9$ are listed. For "Loc 1", there is no off-diagonal element larger than 0, but the diagonal element for the 5^{th} individual is only 51.59%. This is because in the

LOS configuration the human body to be identified is close to both the transmitter and the receiver, which leads to stronger radio biometrics embedded in the CSI. This makes different individuals more distinguishable while making the identification system sensitive and vulnerable to small variations on the human body, e.g., the slight inconsistency in poses and standing location of human. "Loc 6" has the worst performance, since its off-diagonal element could reach 97.32%. Meanwhile, the through-the-wall scenario "Loc 7" becomes the most ideal configuration for individual identification in that the minimum diagonal element is higher than 96% and the largest off-diagonal element is only 0.24%.

Similarly, in Table 6.3(a), 6.3(b) and 6.3(c), with the requirement of the minimum diagonal element larger than 99%, the corresponding performance matrices of the aforementioned three cases are shown. To maintain the diagonal values, the identification system has to reduce the threshold μ which inevitably introduces larger off-diagonal elements and more false alarms. Except for the ideal configuration "Loc 7", the other two examples sacrifice the off-diagonal performance to 91.9% and 99.46% respectively.

We can conclude that among the 10 TX-RX locations tested in the experiment, "Loc 7" is the optimal configuration for the proposed system, and is adopted in the following experiments.

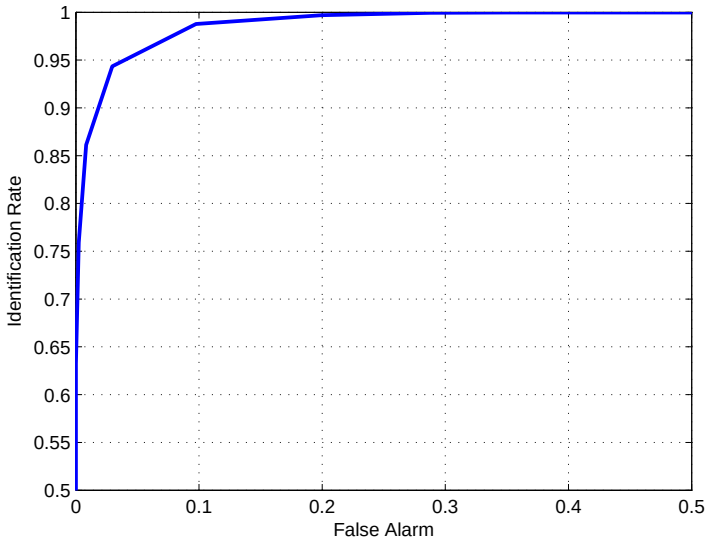

Figure 6.9: ROC curve of identifying 11 individuals.

6.3.4 Human Identification

From the above analysis, we have already observed that the performance of the proposed human identification system is influenced by both the background subtraction and the TX-RX configurations. In this part, the performance is evaluated in a large data set of 11 individuals, with optimal background subtraction applied and "Loc 7" TX-RX configuration. The corresponding ROC curve is plotted in Figure 6.9. With a threshold μ being 0.91, the average identification rate is 98.78% and the average false alarm rate is 9.75%. This is because, when two individuals have similar body contour, the possibility of misclassifying between them increases. However, since not only the contour but also the permittivity and conductivity of body tissue, which is more distinct for different individuals, will affect the WiFi signal propagation that encounters the human body, the accuracy of identification is still high. In the current performance evaluation, the number of participants is

11. We are inviting more people to participate in the experiment and collecting more data for further validation and analysis.

6.3.5 Human Verification

In this set of experiments, we study the performance of individual verification using proposed system. Instead of finding the correct identity among several possible ones, the individual verification is to recognize a specific individual with variations in both the human body and the environment.

6.3.5.1 Stationarity over Time

To begin with, the stationarity of human verification performance is discussed. We collect the CSI measurements for both the empty room and with one individual inside twice a day for three consecutive days. The TRRS maps are demonstrated in Figure 6.10. As shown in Figure 6.10(a), if we only use the CSI from the first measurement as the training set, the TRRS within the same class gradually decreases. This leads to a 90.83% identification rate with the threshold $\mu = 0.75$. However, if we update the training set every time after measurement and identification, e.g. for Day 2 morning experiment the training set consists of the CSI from measurements at Day 1 morning and afternoon, the identification rate increase to 97.35%. The details of the verification accuracy is listed in Table 6.5. Hence, to combat the variations over time, the training data set for both identification and verification should be updated regularly.

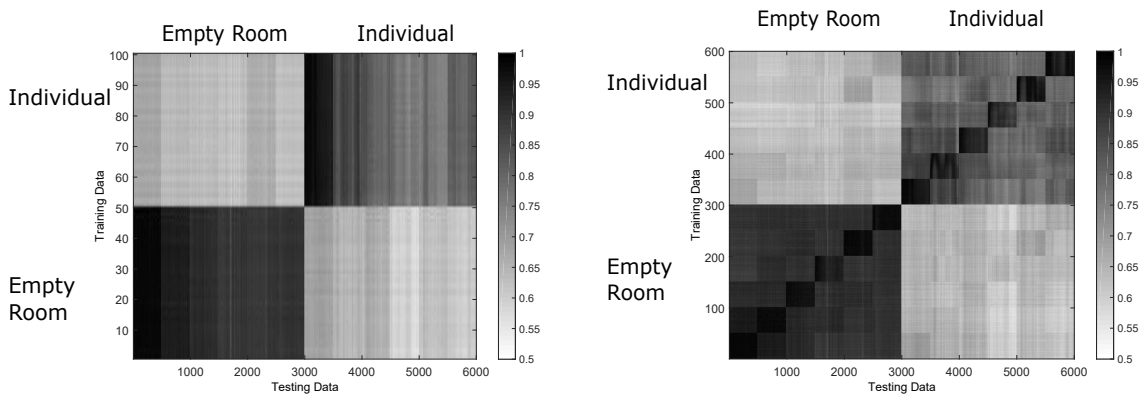

(a) No training database updating. (b) With training database updating.

Figure 6.10: Comparison on TRRS map for stationarity study.

Training Data \ Testing Data	Day1-AM	Day1-PM	Day2-AM	Day2-PM	Day3-AM	Day3-PM
DAY1-AM	1	1	1	0.8522	0.7400	1
DAY1-PM	1	1	1	0.9998	0.9856	1
DAY2-AM	1	0.9989	1	0.9990	0.9997	1
DAY2-PM	1	0.9926	1	1	0.9999	0.9997
DAY3-AM	0.88858	0.8005	0.9997	0.9833	1	0.9996
DAY3-PM	1	0.9746	0.9998	0.9420	0.9996	1

Table 6.5: Performance matrix for stationarity study.

6.3.5.2 Other Variations

In this experiment, the impact of other types of variations such as wearing a coat, carrying a backpack/laptop on the accuracy of verification is discussed. We consider six classes as listed in the Table 6.6 and the corresponding TRRS map is shown in Figure 6.11.

Class Index	Coat	Backpack	Laptop in the backpack
#1	No	No	No
#2	Yes	No	No
#3	Yes	Yes	No
#4	Yes	Yes	Yes
#5	No	Yes	No
#6	No	Yes	Yes

Table 6.6: List of the six variation classes.

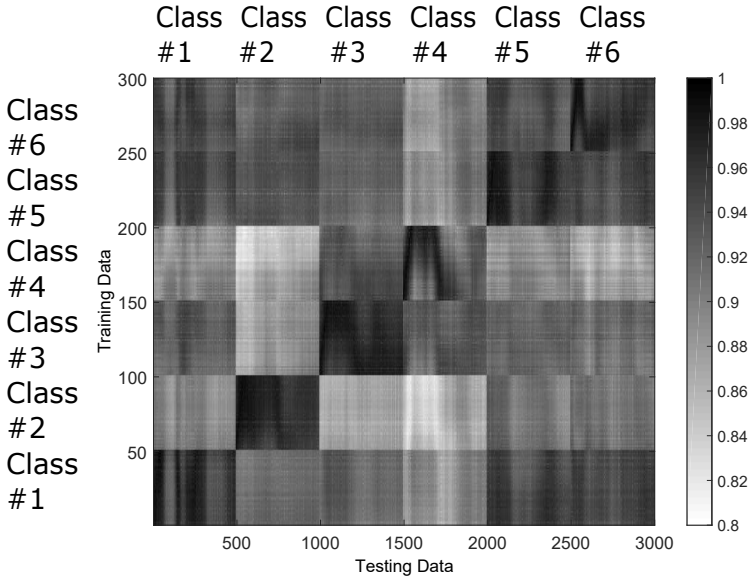

Figure 6.11: TRRS map of variation.

The detailed verification performance is discussed in Table 6.7 where the relation of the threshold μ and the capability of differentiating between different variations is studied. Here, the training set only contains the CSI from class #1. A low

	Threshold 0.92	Threshold 0.9	Threshold 0.85	Threshold 0.84
Class #1	0.9873	0.9994	1	1
Class #2	0.9688	0.9992	1	1
Class #3	0	0.3275	0.9985	1
Class #4	0.4668	0.9756	1	1
Class #5	0.2734	0.9659	1	1
Class #6	0.9720	0.9996	1	1

Table 6.7: Identification rate under variations.

threshold μ reduces the sensitivity of the proposed system in verification. When the threshold μ increases, it may be able to tell whether the individual is wearing a coat and a backpack, shown by the 0 percentage for class #3 to be misclassified as class #1 in Table 6.7. In terms of the backpack with or without laptop inside, as they are shadowed by the human body, the introduced variations have relatively small impact on the accuracy of verification.

6.4 Discussion

Through the above experiments, the capability of identifying and verifying individuals through-the-wall of the proposed TR human identification system has been proved. In this section, the impacts of obstructions and test subjects' postures are evaluated and discussed. The performance of the proposed system is further studied by comparing with a RSSI-based identification system, and the current limitation of the proposed system is discussed.

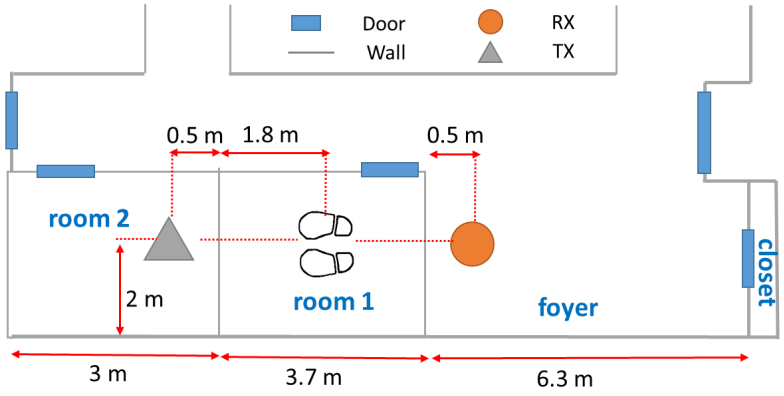

Figure 6.12: Study on impacts of obstructions: test floorplan.

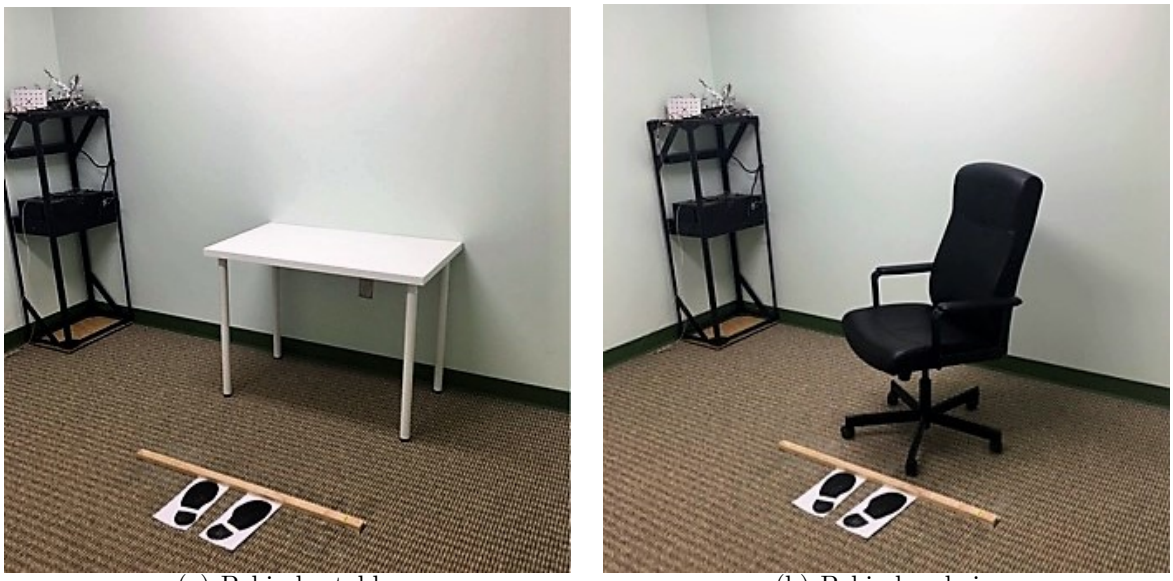

(a) Behind a table.

(b) Behind a chair.

Figure 6.13: Study on impacts of obstructions: different obstructions.

6.4.1 Impact of Obstructions

Experiments are conducted to evaluate and compare the identification accuracy when there is an obstruction in front of and in the same room with the test subject. The office configuration is shown in Figure 6.12. The ROC curves for testing under no obstruction, behind a desk as in Figure 6.13(a) and behind a big

chair as in Figure 6.13(b) are plotted and compared in Figure 6.14. With a similar level of false alarm, the average identification rate for the no-obstruction scenario is 97.57% and the corresponding average false alarm rate is 9.85%. When there is a table in front of the subject against to the wall, the average identification rate increases to 99.53% while the average false alarm rate is 8.82%. When a big chair is put in front of the test subject with a very short distance, the system has an average identification rate of 97.44% and an average false alarm rate of 8.43%. When there is an obstruction between the test subject and the transceiver, because of the reflections and penetrations, more copies of the transmitted signal are created, along with more multipath components. If the obstruction does not attenuate the signal much, most of the signals radiated from the obstruction will eventually encounter the test subject. Then more radio biometric information can be captured through the multipath propagation, which helps the identification performance. However, if the obstruction is thick in size and has a large vertical surface which attenuates and blocks most of the incoming signals, there will be fewer multipath components passing through the human body. As a result, less informative radio biometrics are obtained, compared with the no-obstruction case. Furthermore, as demonstrated in this experiment, the existence of furniture as the obstruction does not affect the system much.

However, the multipath profile changes when the obstruction changes, especially when the obstruction locates between the transmitter and the receiver link and in front of the test subject. The TR technique is trying to capture the difference in multipath profile, and of course it will capture the difference introduced by

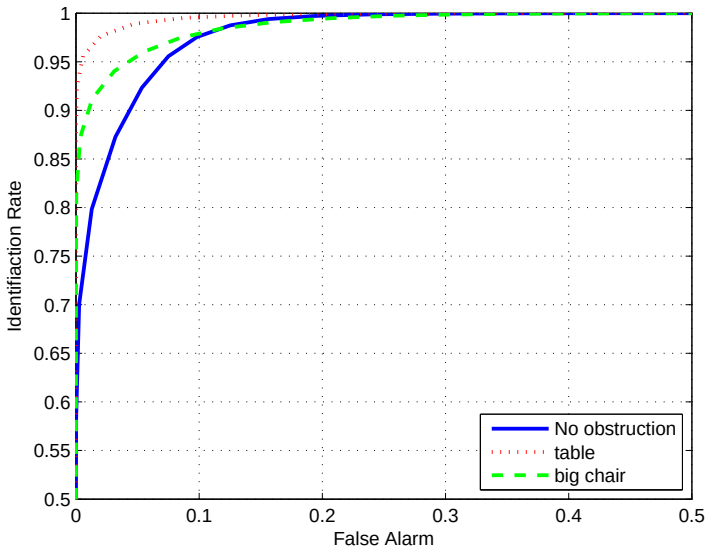

Figure 6.14: Study on impacts of obstructions: ROC curves with different obstructions.

obstruction changes in the meantime. Hence, if an individual is behind a large desk during the training phase and later stands behind a small desk for the testing, the proposed system will notice this change in multipath profiles, leading to a mismatch in the training database.

6.4.2 Impact of Human Postures

Experiments have been conducted to evaluate the effects introduced by human poses. Under the setting in Figure 6.12, 4 participants are asked to stand at the same location and perform 5 different poses by lifting their arms with different degrees and directions, as shown in Figure 6.15. The corresponding ROC curves are shown in Figure 6.16.

In the experiment, we select 50 samples for each subject under the 1^{st} pose

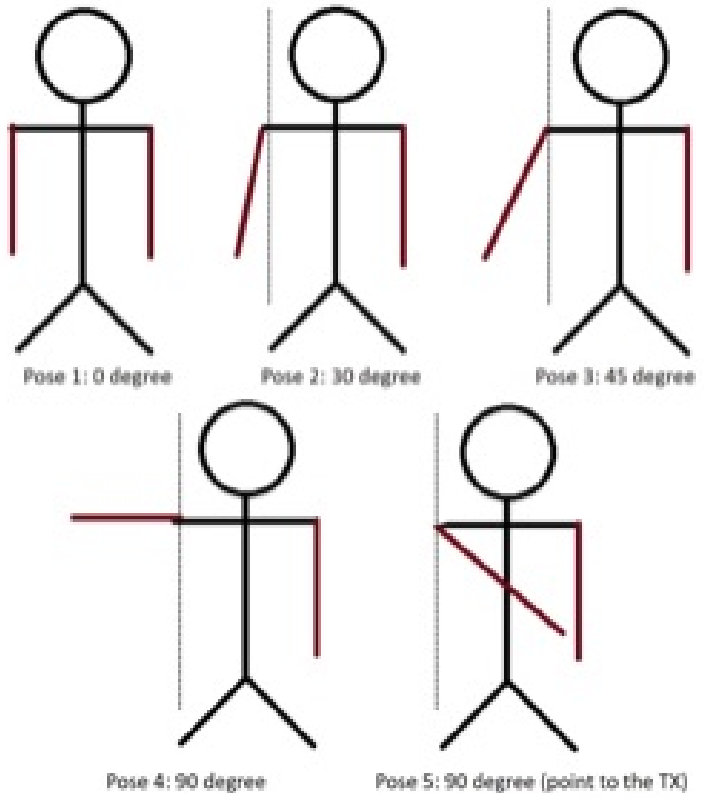

Figure 6.15: Study on human pose effects: test poses.

as the training set. When the testing samples come from the same pose, the identification rate reaches 97.67% with a false alarm rate being 5.58%. However, as the participants change their poses from the 2^{nd} one to the 5^{th} one, the identification rate drops from 95.66% to 88.06%, 58.83% and 79.29% with a false alarm rate around 5.6%. The experimental results validate that pose changes will degrade the system performance. The system is robust to slight changes in posture, e.g., from pose 1 to pose 2. However, as shown by the ROC curve of testing over pose 4 data with the pose 1 training in Figure 6.16, when the pose alters the propagation environment a lot, the proposed TR human identification system fails to find a match in the

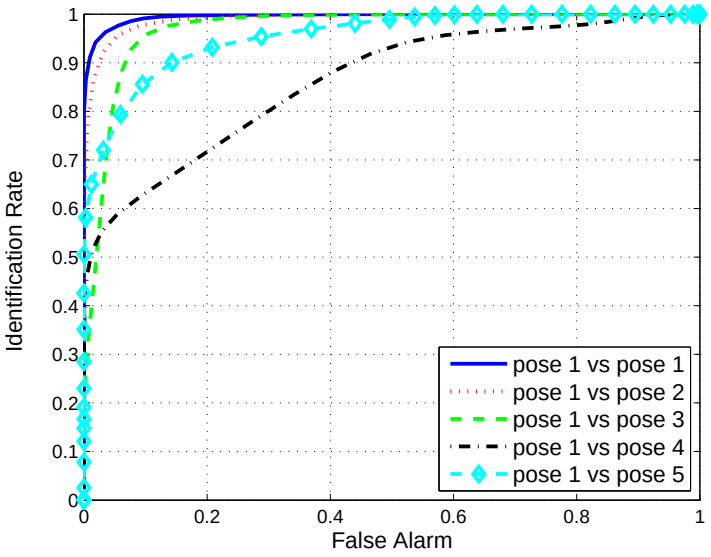

Figure 6.16: Study on human pose effects: ROC curves with different poses.

training database. In the 4^{th} pose, the test subject is asked to lift the left arm with 90 degree and the direction being perpendicular to the link between the transmitter and the receiver. On the other hand, in the 5^{th} pose, test subjects lift the arm at the same height but the arm is parallel to the TX-RX link. Compared the result of testing over the 5^{th} pose with that over the 4^{th} pose, it is noticed that the identification accuracy drops more if the pose changes the silhouettes in a manner that is perpendicular to the TX-RX link.

Hence, when poses or standing locations change, the multipath profiles in the TR space for a test subjects might fall out of the "proximity" (range of a high similarity) of his or her self, which results in a reduce in the identification rate. Moreover, a worse situation is that the changed multipath profiles fall into the "proximity" of other test subjects which leads to an increase in the false alarm rate.

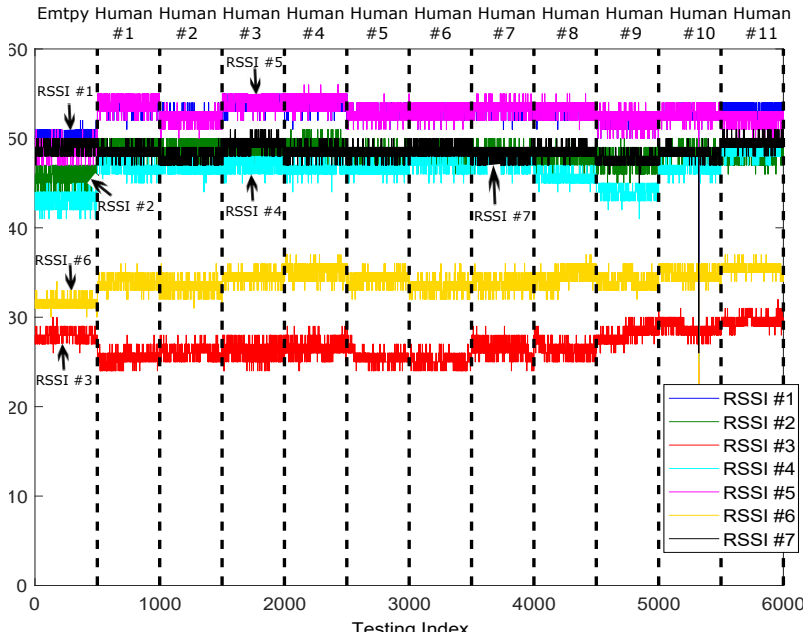

Figure 6.17: RSSI values variation of 11 individuals.

6.4.3 Comparison with RSSI-based Approach

Using the standard WiFi chipsets, besides the CSI, in each measurement we can also obtain a 7×1 RSS vectors, consisting of 6 RSS values for 3 receiving antenna in each 20 MHz band and 1 overall RSS value. Here, we treat each real-valued 7×1 vector as the feature and apply the k nearest neighbors (kNN) classifiers to the measurements.

6.4.3.1 RSSI for Identification

We first test the identification accuracy of the RSSI-based approach on the dataset of 11 individuals. From the results in Figure 6.17, the RSSI difference between different individuals is small. The false alarm rate is 68.07% and the identification rate is only 31.93%, which is far inferior to the proposed identification

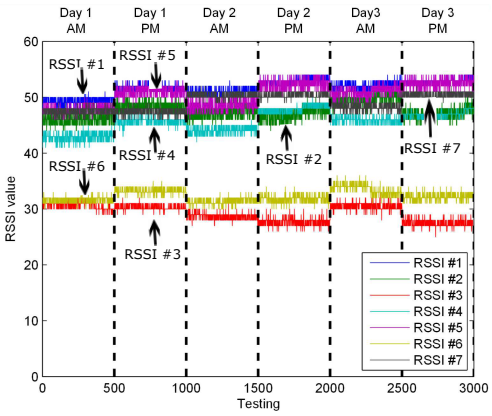

(a) RSSI for empty room.

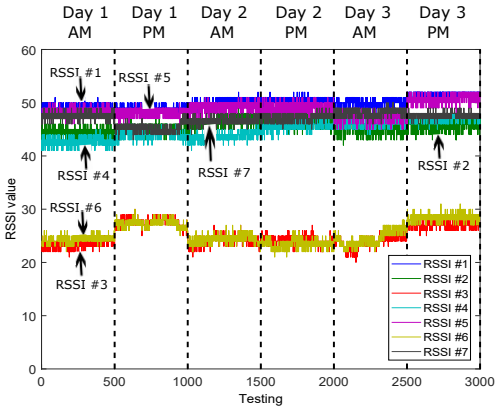

(b) RSSI with individual present.

Figure 6.18: RSSI values comparison on stationarity.

system.

6.4.3.2 RSSI for Verification

In Figure 6.18, the stationarity is evaluated and from the plot it is obvious that the RSS value is not stable over time. Without training database update, the identification rate for the individual is only 89.67% with a 10.33% possibility that the individual is misclassified as an empty room. Even with the training database update, the identification rate does not improve due to the instability of the RSS values over time.

Furthermore, in terms of verifying individual with small variations as listed in Table 6.7, the RSSI-based approach can hardly differentiate between different variations by only using the 7×1 RSS vector as shown in Figure 6.19 and in the confusion matrix of individual verification in Table 6.8. The reason for its insensitivity to small variations is the same as that for its incapability in human identification. The

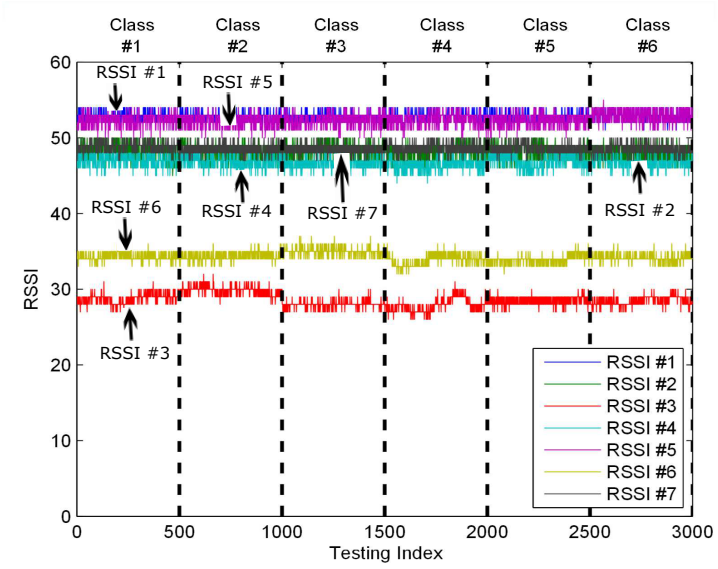

Figure 6.19: RSSI values comparison on variations.

Training Data \ Testing Data	Class #1	Class #2	Class #3	Class #4	Class #5	Class #6
Class #1	0. 3140	0.3680	0.0840	0.0840	0.1980	0. 2260
Class #2	0. 0220	0. 0280	0. 0020	0	0. 0420	0. 0040
Class #3	0. 0640	0. 0840	0. 2920	0. 1360	0. 0660	0. 0980
Class #4	0. 2340	0. 0220	0. 4600	0. 4360	0. 2940	0. 2600
Class #5	0. 1040	0. 1160	0. 0100	0. 1020	0. 1260	0. 0740
Class #6	0. 2620	0. 3820	0. 1520	0. 2420	0. 2740	0. 3380

Table 6.8: Confusion matrix under RSSI-based approach.

7×1 RSS vector feature only captures little human radio biometric information and loses the individual discrimination.

Hence, even though the RSSI-based approach is robust to the small variations on human body, it cannot be put into practice for human identification and ver-

ification. Moreover, since RSSI is only a real-valued scaler which approximately represents the received signal power, it is less informative, susceptible to noise and has large intra-class variations which degrades the identification accuracy a lot when the number of test subjects increases. Compared with the RSSI-based approach, the proposed TR human identification system succeeds in capturing and extracting the human radio biometric information embedded in the CSI, and in distinguishing individuals with high accuracy through-the-wall.

6.4.4 Limitations

At current stage, the proposed TR human identification system exhibits some limitations:

1. The proposed system adopts a simple model for human radio biometrics embedded in the CSI as shown in (6.1). As a result, the obtained human radio biometrics $\delta\mathbf{h}$ and the environment component $\mathbf{h}_{F,0}$ is correlated. In other words, the human radio biometrics $\delta\mathbf{h}$ is location-dependent, which requires the system to run in an environment consistent over time. Future work includes developing algorithms to separate the human radio biometrics and the outside environment.

2. Current system is equipped with only one pair of the transmitter and the receiver, and hence its performance can be improved by deploying more transceiver pairs to capture fine-grained human radio biometrics from different directions simultaneously.

3. In the current work, it is difficult to scientifically prove the uniqueness of human radio biometrics, when taking into account how complicated the techniques it requires to extract all of these biological features from each individual are. In the future work, experiments that involve more subjects will be conducted and techniques that can record other biological features will be utilized to provide more details in human biological characteristics, such as the muscle mass index and the body temperature. With more detailed information regarding individual biological features besides the common information like height, weight, gender and clothing, the uniqueness of radio biometrics can be well studied, tested and verified.

Despite these limitations, we believe the proposed TR human identification system should be viewed as a milestone in the development of both the human identification systems and wireless sensing systems. For the current system, it can be implemented in the environments that remain stationary most of the time. For example, it can be implemented for identity verification at places like bank vaults to allow the entry of authorized staff. It can also be used in home security systems, functioning as wireless electronic keys in vacation houses. Moreover, the location embedded radio biometrics are helpful in applications that require to tell both who the test subject is and where the test subject is. Once the environment-independent radio biometric information is extracted out, the proposed system can work to identify individuals without being noticed by test subjects and implement in applications that require no direct contact with test subjects or where there are obstructions

in-between the sensor and the subject.

6.5 Summary

In this chapter, we presented a TR human identification system to identify individuals through the walls (i.e., in the absence of any LOS path), based on the human radio biometrics in WiFi signals. To the best of our knowledge, this is the first effort to show and verify the existence of human radio biometrics, which can be found embedding in the wireless CSI. Moreover, we proposed a human recognition system that extracts the unique radio biometrics as features from the CSI for differentiating between people through the wall. We defined the term *radio shot* as the procedure to take and record human radio biometrics via WiFi signals. Our work demonstrates the potential of using commercial WiFi signals to capture human radio biometrics for individual identifications.

Chapter 7

Conclusions and Future Work

7.1 Conclusions

Thanks to the multipath propagation, indoor activities affect the surrounding wireless signal propagation, and information describing those activities is in turn embedded in the wireless signals. Hence, one can decipher the surrounding environment by analyzing instantaneous CSI and extracting activity-induced changes from it. Radio analytics was proposed as the notion of concept that represents techniques to reveal information of activities and surrounding environments from radio waves. In these dissertation, we demonstrated the feasibility as well as the capability of radio analytics by proposing three indoor monitoring systems and one human recognition system using WiFi, and evaluating the system performance through extensive experiments conducted in real indoor environments.

We introduced the fundamental theory behind radio analytics in Chapter 2. We first elaborated on the concept of treating each multipath component in the CSI as a virtual antenna, which enables us to analyze, model and extract indoor activity information and human radio biometrics from measured CSI, and theoretically supports the proposed systems. Then, we reviewed the history of TR technique and

described the notion of TR space. Moreover, we defined the TRRS and explained its calculation for both frequency domain and time domain CSI. By leveraging TRRS, one can quickly and accurately quantify the similarity between different multipath profiles.

In Chapter 3, we proposed a TR based wireless indoor events detection system, TRIEDS. By representing each indoor event with a specific complex-valued multipath profile and exploiting TR technique to measure and evaluate the changes of CSI in the indoor environment, the proposed TRIEDS system was able to achieve high accuracy through-the-wall multiple-event detection with low-complexity single-antenna devices that operate in the ISM band. We built a prototype on single-antenna transceivers which operate on ISM band with the carrier frequency being 5.4 GHz and under a 125 MHZ bandwidth. We deployed the prototype in a multi-room office to detect the open/close state of wooden doors. Unlike previous works on wireless indoor monitoring that rely on multiple antennas, dedicated sensors, ultra-wideband transmission or LOS environment, TRIEDS introduced a novel and practical solution to future IoT applications.

In Chapter 4, we designed a new TR based indoor monitoring system, TRIMS, with off-the-shelf WiFi devices. TRIMS was capable of exploiting both the amplitude and the phase information in the CSI and performing real-time indoor environments monitoring under both LOS and NLOS scenarios. Different from the system proposed in Chapter 3 that used TRRS directly as a similarity score for event detection, TRIMS delivered indoor multiple events detection and human motion monitoring by analyzing the statistical behavior of TRRS. We derived the statistics

of TRRS in this chapter and evaluated the performance of TRIMS through intruder detection experiments conducted in different single family houses with resident activities. In general, by achieving a high accuracy in long-term indoor monitoring experiments, TRIMS demonstrated its prominent and promising role in future intelligent WiFi-based low-complexity smart radios.

At the end of the first part of this dissertation, in Chapter 5, we proposed an indoor monitoring system that not only analyzed the single CSI sample but also extracted the temporal information embedded in the CSI time series, which makes it different from the systems in Chapter 3 and Chapter 4. Because the occurrence of each indoor event can be decomposed into a continuous transition between multiple intermediate indoor states, it usually takes several seconds for an indoor event evolving and a similar CSI transition pattern will be exhibited among different realizations. In other words, indoor event information is embedded not only in each CSI sample but also in that of how CSI changes along time. We designed algorithms to address practical problems in feature extraction, real-time monitoring, and channel fading or changes in the background environment along the time.Results from robustness test and long-term experiments indicated that the proposed system is a promising solution to future IoT applications in indoor monitoring.

Lastly, in Chapter 6 which composes the second part of this dissertation, we presented a human identification system that can discriminate individuals even through walls, i.e., in a NLOS condition. The proposed system relied on the human radio biometric information which records how RF signals interact with and respond to the entire body of a human that is present in the propagation envi-

ronment. We modeled the human radio biometrics in the CSI and validated its existence through experiments. By leveraging TR technique, the proposed system extracted human radio biometric information from WiFi signals with commercial WiFi devices. Considering the fact that the dominant component in the CSI comes from the static environment rather than human body and thus the human radio biometrics are embedded and buried in the multipath CSI, we designed novel algorithms for extracting individual human radio biometrics and mitigating common information from the wireless channel information. We conducted extensive experiments to demonstrate the potential of radio biometrics based human identification using commercial WiFi devices.

7.2 Future Work

With the proliferation of wireless devices that connect and communicate with each other, wireless sensing makes IoT into practice and has dramatically changed our daily life. Meanwhile, the concept of radio analytics has gained a lot of attention. By leveraging the large degree of freedom delivered via multipath propagation, one can retrieve the environmental information embedded in the CSI and decipher as well as perceive the surrounding world. In this dissertation, we have demonstrated the idea and the capability of radio analytics, and proposed wireless indoor monitoring systems and one through-the-wall human identification systems. However, several critical issues remain to be resolved.

In our indoor monitoring research, we have demonstrated the performance of

proposed systems using door opening and closing examples. Because the physical location of a trained door will not change, its opening and closing event yields a fixed physical moving trace, resulting in a fixed CSI time series. However, there are many indoor events that may happen at different locations from time to time. In other words, such kind of indoor events are only associated with a relative trajectory of moving paths, with the initial position unknown. Consequently, the corresponding CSI time series is altered among multiple occurrences of an event. Nonetheless, the CSI time series captured at different realizations should implicitly possess a distinct but consistent pattern, thanks to the relative moving trajectory determined uniquely in the course of an event. Therefore, in the future, we would like to investigate the possibility of modelling, extracting and analyzing the inherent location-independent pattern brought by each indoor event to the CSI time series, which will enable new radio analytic technique with environment independent radio features embedded in the multipath.

Secondly, in our previous study of indoor monitoring, we model each indoor event independently, considering at one time only one event will happen and change the multipath propagation. However, multiple different events may happen in the same time duration in a real indoor environment. The change introduced to a multipath profile is indeed a composition or integration of co-occurred events, which will definitely be different from the change introduced by a single event. Therefore, to successfully deploy indoor monitoring systems, we need to study and analyze the decoupling of multi-event changes in CSI and develop the corresponding algorithms.

In our radio biometrics research, we have validated the existence of radio bio-

metrics and successfully implemented a TR based human identification system which achieved high accuracy through-the-wall human recognition using radio biometrics. With the surge of super computers with high computation powers and the ubiquity of cameras, vision based human identification has entered the era of big data, and the accuracy along with the robustness of face recognition has been improved a lot through deep learning. It would be of interest to apply big data approach to the proposed radio biometrics and analyze how it will affect the radio biometric based recognition performance. Because the CSI is different from an image which is much more straight-forward, the existing deep learning methods may not work for radio biometric based system. In the future, we would like to develop novel deep learning based algorithms dedicated to radio biometrics. Meanwhile, it is also urgent to collect more radio biometric information from human groups of various diversity. It is our belief that radio biometrics can achieve comparable identification accuracy with vision based approach, but outperforms it in terms of privacy and restriction of deployment, e.g., no requirement of LoS. We hope that one day the radio biometrics based human identification system will enter our everyday life and become as prevalent as today's face recognition.

Bibliography

[1] Yan Chen, Feng Han, Yu-Han Yang, Hang Ma, Yi Han, Chunxiao Jiang, Hung-Quoc Lai, David Claffey, Zoltan Safar, and K. J. Ray Liu. Time-reversal wireless paradigm for green Internet of Things: An overview. *IEEE Internet of Things Journal*, 1(1):81–98, 2014.

[2] Beibei Wang, Qinyi Xu, Chen Chen, Feng Zhang, and K. J. Ray Liu. The promise of radio analytics: A future paradigm of wireless positioning, tracking, and sensing. *IEEE Signal Processing Magazine*, 35(3):59–80, May 2018.

[3] R. Cucchiara, C. Grana, A. Prati, and R. Vezzani. Computer Vision System for In-house Video Surveillance. *IEE Proceedings-Vision, Image and Signal Processing*, 152(2):242–249, April 2005.

[4] Ali Maleki Tabar, Arezou Keshavarz, and Hamid Aghajan. Smart Home Care Network using Sensor Fusion and Distributed Vision-based Reasoning. In *Proceedings of the 4th ACM International Workshop on Video Surveillance and Sensor Networks*, pages 145–154. ACM, 2006.

[5] Avik Ghose, Kingshuk Chakravarty, Amit Kumar Agrawal, and Nasim Ahmed. Unobtrusive Indoor Surveillance of Patients at Home Using Multiple Kinect Sensors. In *Proceedings of the 11th ACM Conference on Embedded Networked Sensor Systems (SenSys 13)*, SenSys '13, pages 1–2, New York, NY, USA, 2013. ACM.

[6] María José Gómez, Fernando García, David Martín, Arturo de la Escalera, and José María Armingol. Intelligent Surveillance of Indoor Environments based on Computer Vision and 3D Point Cloud Fusion. *Expert Systems with Applications*, 42(21):8156–8171, 2015.

[7] Milo Spadacini, Stefano Savazzi, Monica Nicoli, and S Nicoli. Wireless Networks for Smart Surveillance: Technologies, Protocol Design and Experiments. In *Proceedings of the Wireless Communications and Networking Conference Workshops (WCNCW)*, pages 214–219. IEEE, 2012.

[8] Dian Zhang, Jian Ma, Quanbin Chen, and Lionel M. Ni. An rf-based system for tracking transceiver-free objects. In *Proceedings of the 5th Annual IEEE International Conference on Pervasive Computing and Communications*, pages 135–144, March 2007.

[9] Chunmei Han, Kaishun Wu, Yuxi Wang, and L.M. Ni. Wifall: Device-free fall detection by wireless networks. In *Proceedings of the International Conference on Computer Communications*, pages 271–279, April 2014.

[10] Yu Gu, Fuji Ren, and Jie Li. Paws: Passive human activity recognition based on wifi ambient signals. *IEEE Internet of Things Journal*, 3(5):796–805, Oct 2016.

[11] Heba Abdelnasser, Moustafa Youssef, and Khaled A. Harras. WiGest: A ubiquitous wifi-based gesture recognition system. In *Proceedings of the 2015 IEEE Conference on Computer Communications*, pages 1472–1480, April 2015.

[12] Chenshu Wu, Zheng Yang, Zimu Zhou, Xuefeng Liu, Yunhao Liu, and Jiannong Cao. Non-invasive detection of moving and stationary human with wifi. *IEEE Journal on Selected Areas in Communications*, 33(11):2329–2342, Nov 2015.

[13] Yunze Zeng, Parth H Pathak, Chao Xu, and Prasant Mohapatra. Your AP knows how you move: fine-grained device motion recognition through wifi. In *Proceedings of the 1st ACM workshop on Hot topics in wireless*, pages 49–54. ACM, 2014.

[14] Yan Wang, Jian Liu, Yingying Chen, Marco Gruteser, Jie Yang, and Hongbo Liu. E-eyes: device-free location-oriented activity identification using fine-grained WiFi signatures. In *Proceedings of the 20th Annual International Conference on Mobile Computing and Networking*, pages 617–628. ACM, 2014.

[15] Wei Wang, Alex X. Liu, Muhammad Shahzad, Kang Ling, and Sanglu Lu. Device-free human activity recognition using commercial WiFi devices. *IEEE Journal on Selected Areas in Communications*, 35(5):1118–1131, May 2017.

[16] Kamran Ali, Alex Xiao Liu, Wei Wang, and Muhammad Shahzad. Keystroke recognition using WiFi signals. In *Proceedings of the 21st Annual International Conference on Mobile Computing and Networking*, pages 90–102. ACM, 2015.

[17] Sheng Tan and Jie Yang. Wifinger: Leveraging commodity WiFi for fine-grained finger gesture recognition. In *Proceedings of the 17th ACM International Symposium on Mobile Ad Hoc Networking and Computing*, MobiHoc '16, pages 201–210, New York, NY, USA, 2016. ACM.

[18] Kun Qian, Chenshu Wu, Zheng Yang, Yunhao Liu, and Zimu Zhou. Pads: Passive detection of moving targets with dynamic speed using phy layer information. In *Proceedings of the 20th IEEE International Conference on Parallel and Distributed Systems*, pages 1–8, Dec 2014.

[19] Jiang Xiao, Kaishun Wu, Youwen Yi, Lu Wang, and L.M. Ni. FIMD: Fine-grained device-free motion detection. In *Proceedings of the 18th International Conference on Parallel and Distributed Systems*, pages 229–235, Dec 2012.

[20] Wei Wang, Alex X Liu, Muhammad Shahzad, Kang Ling, and Sanglu Lu. Understanding and modeling of WiFi signal based human activity recognition. In *Proceedings of the 21st Annual International Conference on Mobile Computing and Networking*, pages 65–76. ACM, 2015.

[21] Hai Zhu, Fu Xiao, Lijuan Sun, Ruchuan Wang, and Panlong Yang. R-TTWD: Robust device-free through-the-wall detection of moving human with WiFi. *IEEE Journal on Selected Areas in Communications*, 35(5):1090–1103, May 2017.

[22] Kazuya Ohara, Takuya Maekawa, and Yasuyuki Matsushita. Detecting state changes of indoor everyday objects using Wi-Fi channel state information. volume 1, pages 88:1–88:28, New York, NY, USA, September 2017. ACM.

[23] Kun Qian, Chenshu Wu, Zheng Yang, Yunhao Liu, Fugui He, and Tianzhang Xing. Enabling contactless detection of moving humans with dynamic speeds using csi, January 2018.

[24] Mohammed Abdulaziz Aide Al-qaness, Fangmin Li, Xiaolin Ma, and Guo Liu. Device-free home intruder detection and alarm system using wi-fi channel state information. *International Journal of Future Computer and Communication*, 5(4):180, 2016.

[25] Qifan Pu, Sidhant Gupta, Shyamnath Gollakota, and Shwetak Patel. Whole-home gesture recognition using wireless signals. In *Proceedings of the 19th Annual International Conference on Mobile computing & networking*, pages 27–38. ACM, 2013.

[26] Bo Tan, Alison Burrows, Robert Piechocki, Ian Craddock, Qingchao Chen, Karl Woodbridge, and Kevin Chetty. Wi-Fi based passive human motion sensing for in-home healthcare applications. In *Proceedings of the IEEE 2nd World Forum on Internet of Things (WF-IoT)*, pages 609–614. IEEE, 2015.

[27] Kun Qian, Chenshu Wu, Zimu Zhou, Yue Zheng, Zheng Yang, and Yunhao Liu. Inferring motion direction using commodity WiFi for interactive exergames. In *Proceedings of the 2017 CHI Conference on Human Factors in Computing Systems*, pages 1961–1972, New York, NY, USA, 2017. ACM.

[28] Daqing Zhang, Hao Wang, Yasha Wang, and Junyi Ma. Anti-fall: A non-intrusive and real-time fall detector leveraging CSI from commodity WiFi devices. In *Proceedings of the International Conference on Smart Homes and Health Telematics*, pages 181–193. Springer, 2015.

[29] Hao Wang, Daqing Zhang, Yasha Wang, Junyi Ma, Yuxiang Wang, and Shengjie Li. Rt-fall: A real-time and contactless fall detection system with commodity wifi devices. *IEEE Transactions on Mobile Computing*, 16(2):511–526, Feb 2017.

[30] Gaurav K Nanani and MVV Kantipudi. A study of WiFi based system for moving object detection through the wall. *International Journal of Computer Applications*, 79(7), 2013.

[31] Yanzi Zhu, Yibo Zhu, Ben Y Zhao, and Haitao Zheng. Reusing 60ghz radios for mobile radar imaging. In *Proceedings of the 21st Annual International Conference on Mobile Computing and Networking*, pages 103–116. ACM, 2015.

[32] Deepak Vasisht, Swarun Kumar, and Dina Katabi. Decimeter-level localization with a single wifi access point. In *Proceedings of the 13th USENIX Symposium on Networked Systems Design and Implementation (NSDI 16)*, pages 165–178, Santa Clara, CA, 2016. USENIX Association.

[33] Fadel Adib, Zach Kabelac, Dina Katabi, and Robert C. Miller. 3D tracking via body radio reflections. In *Proceedings of the 11th USENIX Symposium on Networked Systems Design and Implementation*, pages 317–329, Seattle, WA, April 2014. USENIX Association.

[34] Fadel Adib, Chen-Yu Hsu, Hongzi Mao, Dina Katabi, and Frédo Durand. Capturing the human figure through a wall. *ACM Transactions on Graphics*, 34(6):219:1–219:13, October 2015.

[35] Fadel Adib, Hongzi Mao, Zachary Kabelac, Dina Katabi, and Robert C. Miller. Smart homes that monitor breathing and heart rate. In *Proceedings of the 33rd Annual ACM Conference on Human Factors in Computing Systems*, pages 837–846, New York, NY, USA, 2015. ACM.

[36] Chen-Yu Hsu, Yuchen Liu, Zachary Kabelac, Rumen Hristov, Dina Katabi, and Christine Liu. Extracting gait velocity and stride length from surrounding radio signals. In *Proceedings of the 2017 CHI Conference on Human Factors in Computing Systems*, CHI '17, pages 2116–2126, New York, NY, USA, 2017. ACM.

[37] Mingmin Zhao, Shichao Yue, Dina Katabi, Tommi S. Jaakkola, and Matt T. Bianchi. Learning sleep stages from radio signals: A conditional adversarial architecture. In Doina Precup and Yee Whye Teh, editors, *Proceedings of the 34th International Conference on Machine Learning*, volume 70 of *Proceedings of Machine Learning Research*, pages 4100–4109, International Convention Centre, Sydney, Australia, 06–11 Aug 2017. PMLR.

[38] Geoffroy Lerosey, J De Rosny, A Tourin, A Derode, G Montaldo, and M Fink. Time reversal of electromagnetic waves. *Physical review letters*, 92(19):193904, 2004.

[39] Qinyi Xu, Chunxiao Jiang, Yi Han, Beibei Wang, and K. J. Ray Liu. Waveforming: An overview with beamforming. *IEEE Communications Surveys & Tutorials*, 20(1):132–149, Firstquarter 2018.

[40] Yan Chen, Beibei Wang, Yi Han, Hung-Quoc Lai, Zoltan Safar, and K. J. Ray Liu. Why time reversal for future 5G wireless? *IEEE Signal Processing Magazine*, 33(2):17–26, March 2016.

[41] Yi Han, Yan Chen, Beibei Wang, and K. J. Ray Liu. Time-reversal massive multipath effect: A single-antenna massive MIMO solution. *IEEE Transactions on Communications*, 64(8):3382–3394, Aug 2016.

[42] Jeffrey G. Andrews, Stefano Buzzi, Wan Choi, Stephen V. Hanly, Angel Lozano, Anthony C. K. Soong, and Jianzhong Charlie Zhang. What will 5G be? *IEEE Journal on Selected Areas in Communications*, 32(6):1065–1082, June 2014.

[43] B. Bogert. Demonstration of delay distortion correction by time-reversal techniques. *IRE Transactions on Communications Systems*, 5(3):2–7, December 1957.

[44] Mathias Fink, Claire Prada, Francois Wu, and Didier Cassereau. Self focusing in inhomogeneous media with time reversal acoustic mirrors. *IEEE Ultrasonics Symposium Proceedings*, pages 681–686, 1989.

[45] Mathias Fink. Time reversal of ultrasonic fields. I. basic principles. *IEEE Transactions on Ultrasonics, Ferroelectrics, and Frequency Control*, 39(5):555–566, 1992.

[46] Francois Wu, Jean-Louis Thomas, and Mathias Fink. Time reversal of ultrasonic fields. II. experimental results. *IEEE Transactions on Ultrasonics, Ferroelectrics, and Frequency Control*, 39(5):567–578, 1992.

[47] Christian Dorme, Mathias Fink, and Claire Prada. Focusing in transmit-receive mode through inhomogeneous media: The matched filter approach. In *IEEE 1992 Ultrasonics Symposium Proceedings*, pages 629–634 vol.1, Oct 1992.

[48] A. Derode, P. Roux, and M. Fink. Acoustic time-reversal through high-order multiple scattering. In *Proceedings of the 1995 IEEE Ultrasonics Symposium. Proceedings. An International Symposium*, volume 2, pages 1091–1094 vol.2, Nov 1995.

[49] WA Kuperman, William S Hodgkiss, Hee Chun Song, T. Akal, C. Ferla, and Darrell R Jackson. Phase conjugation in the ocean: Experimental demonstration of an acoustic time-reversal mirror. *The Journal of the Acoustical Society of America*, 103(1):25–40, 1998.

[50] Hee Chun Song, WA Kuperman, WS Hodgkiss, T Akal, and C Ferla. Iterative time reversal in the ocean. *The Journal of the Acoustical Society of America*, 105(6):3176–3184, 1999.

[51] Daniel Rouseff, Darrell R Jackson, Warren LJ Fox, Christopher D Jones, James A Ritcey, and David R Dowling. Underwater acoustic communication by passive-phase conjugation: Theory and experimental results. *IEEE Journal of Oceanic Engineering*, 26(4):821–831, 2001.

[52] Geoffrey F. Edelmann, T. Akal, William S. Hodgkiss, Seongil Kim, William A. Kuperman, and Hee Chun Song. An initial demonstration of underwater acoustic communication using time reversal. *IEEE Journal of Oceanic Engineering*, 27(3):602–609, Jul 2002.

[53] Benjamin E Henty and Daniel D Stancil. Multipath-enabled super-resolution for RF and microwave communication using phase-conjugate arrays. *Physical Review Letters*, 93(24):243904, 2004.

[54] Geoffroy Lerosey, J De Rosny, A Tourin, A Derode, G Montaldo, and M Fink. Time reversal of electromagnetic waves and telecommunication. *Radio Science*, 40(6):1–10, 2005.

[55] G Lerosey, J De Rosny, A Tourin, A Derode, and M Fink. Time reversal of wideband microwaves. *Applied Physics Letters*, 88(15):154101, 2006.

[56] Robert C. Qiu, Chenming Zhou, Nan Guo, and John Q. Zhang. Time reversal with miso for ultra-wideband communications: experimental results. In *Proceedings of the 2006 IEEE Radio and Wireless Symposium*, pages 499–502, Jan 2006.

[57] Julien de Rosny, Geoffroy Lerosey, and Mathias Fink. Theory of electromagnetic time-reversal mirrors. *IEEE Transactions on Antennas and Propagation*, 58(10):3139–3149, 2010.

[58] I. H. Naqvi, G. E. Zein, G. Lerosey, J. D. Rosny, P. Besnier, A. Tourin, and M. Fink. Experimental validation of time reversal ultra wide-band communication system for high data rates. *IET Microwaves, Antennas Propagation*, 4(5):643–650, May 2010.

[59] Majid Emami, Mai Vu, Jan Hansen, Arogyaswami J Paulraj, and George Papanicolaou. Matched filtering with rate back-off for low complexity communications in very large delay spread channels. In *Proceedings of the 38th Asilomar Conference on Signals, Systems and Computers*, pages 218–222. IEEE, 2004.

[60] Hung Tuan Nguyen, Istvn Zsolt Kovcs, and Patrick Claus Friedrich Eggers. A time reversal transmission approach for multiuser UWB communications. *IEEE Transactions on Antennas and Propagation*, 54(11):3216–3224, Nov 2006.

[61] Raul L. de Lacerda Neto, Aawatif Menouni Hayar, and Merouane Debbah. Channel division multiple access based on high UWB channel temporal resolution. In *Proceedings of the IEEE Vehicular Technology Conference*, pages 1–5, Sept 2006.

[62] Nan Guo, Brian M. Sadler, and Robert C. Qiu. Reduced-complexity UWB time-reversal techniques and experimental results. *IEEE Transactions on Wireless Communications*, 6(12):4221–4226, December 2007.

[63] A. Khaleghi, G. EI Zein, and I. H. Naqvi. Demonstration of time-reversal in indoor ultra-wideband communication: Time domain measurement. In *Proceedings of the 2007 4th International Symposium on Wireless Communication Systems*, pages 465–468, Oct 2007.

[64] Hung Tuan Nguyen, Jørgen Bach Andersen, and G.F. Pedersen. The potential use of time reversal techniques in multiple element antenna systems. *IEEE Communications Letters*, 9(1):40–42, Jan 2005.

[65] Yuanwei Jin, Yi Jiang, and Jos M. F. Moura. Multiple antenna time reversal transmission in ultra-wideband communications. In *Proceedings of the 2007 IEEE Global Telecommunications Conference*, pages 3029–3033, Nov 2007.

[66] Chenming Zhou, Nan Guo, Brian M. Sadler, and Robert C. Qiu. Performance study on time reversed impulse MIMO for UWB communications based on measured spatial UWB channels. In *Proceedings of the 2007 IEEE Military Communications Conference*, pages 1–6, Oct 2007.

[67] Antonios Pitarokoilis, Saif Khan Mohammed, and Erik G. Larsson. Uplink performance of time-reversal MRC in massive MIMO systems subject to phase noise. *IEEE Transactions on Wireless Communications*, 14(2):711–723, Feb 2015.

[68] Beibei Wang, Yongle Wu, Feng Han, Yu-Han Yang, and K. J. R. Liu. Green wireless communications: A time-reversal paradigm. *IEEE Journal on Selected Areas in Communications*, 29(8):1698–1710, 2011.

[69] M. A. Bouzigues, I. Siaud, M. Helard, and A. M. Ulmer-Moll. Turn back the clock: Time reversal for green radio communications. *IEEE Vehicular Technology Magazine*, 8(1):49–56, March 2013.

[70] Feng Han, Yu-Han Yang, Beibei Wang, Yongle Wu, and K. J. Ray Liu. Time-reversal division multiple access over multi-path channels. *IEEE Transactions on Communications*, 60(7):1953–1965, July 2012.

[71] Yu-Han Yang, Beibei Wang, W. Sabrina Lin, and K. J. Ray Liu. Near-optimal waveform design for sum rate optimization in time-reversal multiuser downlink systems. *IEEE Transactions on Wireless Communications*, 12(1):346–357, January 2013.

[72] Feng Han and K. J. Ray Liu. A multiuser trdma uplink system with 2d parallel interference cancellation. *IEEE Transactions on Communications*, 62(3):1011–1022, March 2014.

[73] Eunchul Yoon, Sun-Yong Kim, and Unil Yun. A time-reversal-based transmission using predistortion for intersymbol interference alignment. *IEEE Transactions on Communications*, 63(2):455–465, Feb 2015.

[74] Yu-Han Yang and K. J. Ray Liu. Waveform design with interference pre-cancellation beyond time-reversal systems. *IEEE Transactions on Wireless Communications*, 15(5):3643–3654, May 2016.

[75] Qinyi Xu, Yan Chen, and K. J. Ray Liu. Combating strong-weak spatial-temporal resonances in time-reversal uplinks. *IEEE Transactions on Wireless Communications*, 15(1):568–580, Jan 2016.

[76] Yan Chen, Feng Han, Yu-Han Yang, Hang Ma, Yi Han, Chunxiao Jiang, Hung Quoc Lai, David Claffey, Zoltan Safar, and K. J. Ray Liu. Time-reversal wireless paradigm for green internet of things: An overview. *IEEE Internet of Things Journal*, 1(1):81–98, Feb 2014.

[77] Zhung-Han Wu, Yi Han, Yan Chen, and K. J. Ray Liu. A time-reversal paradigm for indoor positioning system. *IEEE Transactions on Vehicular Technology*, 64(4):1331–1339, April 2015.

[78] Chen Chen, Yi Han, Yan Chen, and K. J. Ray Liu. Indoor global positioning system with centimeter accuracy using wi-fi. *IEEE Signal Processing Magazine*, 33(6):128–134, Nov 2016.

[79] Chen Chen, Yan Chen, Yi Han, Hung-Quoc Lai, and K. J. Ray Liu. Achieving centimeter-accuracy indoor localization on wifi platforms: A frequency hopping approach. *IEEE Internet of Things Journal*, 4(1):111–121, Feb 2017.

[80] Chen Chen, Yan Chen, Yi Han, Hung-Quoc Lai, Feng Zhang, and K. J. Ray Liu. Achieving centimeter-accuracy indoor localization on wifi platforms: A multi-antenna approach. *IEEE Internet of Things Journal*, 4(1):122–134, Feb 2017.

[81] Feng Zhang, Chen Chen, Beibei Wang, and K. J. Ray Liu. Wispeed: A statistical electromagnetic approach for device-free indoor speed estimation. *IEEE Internet of Things Journal*, pages 1–1, 2018.

[82] Qinyi Xu, Yan Chen, Beibei Wang, and K. J. Ray Liu. TRIEDS: Wireless events detection through the wall. *IEEE Internet of Things Journal*, 4(3):723–735, June 2017.

[83] Qinyi Xu, Zoltan Safar, Yi Han, Beibei Wang, and K. J. Ray Liu. Statistical learning over time-reversal space for indoor monitoring system. *IEEE Internet of Things Journal*, 5(2):970–983, April 2018.

[84] Qinyi Xu, Feng Zhang, Beibei Wang, Min Wu, and K. J. Ray Liu. Real-time indoor event monitoring using csi time series. In *Proceedings of the IEEE International Conference on Acoustics, Speech, and Signal Processing*, page 1, April 2018.

[85] Qinyi Xu, Yan Chen, Beibei Wang, and K. J. Ray Liu. Radio biometrics: Human recognition through a wall. *IEEE Transactions on Information Forensics and Security*, 12(5):1141–1155, May 2017.

[86] Chen Chen, Yi Han, Yan Chen, Hung-Quoc Lai, Feng Zhang, Beibei Wang, and K. J. Ray Liu. Tr-breath: Time-reversal breathing rate estimation and detection. *IEEE Transactions on Biomedical Engineering*, 65(3):489–501, March 2018.

[87] Ruichi Yu, Hongcheng Wang, and Larry S. Davis. Remotenet: Efficient relevant motion event detection for large-scale home surveillance videos. *IEEE Winter Conference on Applications of Computer Vision (WACV)*, 2018.

[88] Ruichi Yu, Hongcheng Wang, Ang Li, Jingxiao Zheng, Vlad I. Morariu, and Larry S. Davis. Representing videos based on scene layouts for recognizing agent-in-place actions. *arXiv preprint arXiv:1711.05282*, 2018.

[89] Hiroaki Sakoe and Seibi Chiba. Dynamic programming algorithm optimization for spoken word recognition. *IEEE transactions on acoustics, speech, and signal processing*, 26(1):43–49, 1978.

[90] Meinard Müller. *Information retrieval for music and motion*. Springer Berlin Heidelberg, 2007.

[91] Anil Jain, Arun A Ross, and Karthik Nandakumar. *Introduction to biometrics*. Springer Science & Business Media, 2011.

[92] Anil K Jain, Karthik Nandakumar, and Arun Ross. 50 years of biometric research: Accomplishments, challenges, and opportunities. *Pattern Recognition Letters*, 2016.

[93] Davrondzhon Gafurov. A survey of biometric gait recognition: Approaches, security and challenges. 2007.

[94] Dave Tahmoush and Jerry Silvious. Radar micro-doppler for long range front-view gait recognition. In *Proceedings of the 2009 IEEE 3rd International Conference on Biometrics: Theory, Applications, and Systems*, pages 1–6, Sept 2009.

[95] R. G. Raj, V. C. Chen, and R. Lipps. Analysis of radar human gait signatures. *IET Signal Processing*, 4(3):234–244, June 2010.

[96] Gregory Melia. Electromagnetic absorption by the human body from 1-15 GHz. 2013.

[97] Petr Beckmann and Andre Spizzichino. The scattering of electromagnetic waves from rough surfaces. *Norwood, MA, Artech House, Inc., 1987, 511 p.*, 1987.

[98] Sami Gabriel, RW Lau, and Camelia Gabriel. The dielectric properties of biological tissues: II. measurements in the frequency range 10 hz to 20 GHz. *Physics in medicine and biology*, 41(11):2251, 1996.

[99] Sami Gabriel, RW Lau, and Camelia Gabriel. The dielectric properties of biological tissues: III. parametric models for the dielectric spectrum of tissues. *Physics in medicine and biology*, 41(11):2271, 1996.

[100] Samuel Levy, Granger Sutton, Pauline C Ng, Lars Feuk, Aaron L Halpern, Brian P Walenz, Nelson Axelrod, Jiaqi Huang, Ewen F Kirkness, Gennady Denisov, et al. The diploid genome sequence of an individual human. *PLoS Biol*, 5(10):e254, 2007.